Title
Anisotropy in the deep Earth

Authors
Romanowicz, Barbara
Wenk, Hans-Rudolf

Publication Date
2017-08-01

DOI
10.1016/j.pepi.2017.05.005

Peer reviewed

Physics of the Earth and Planetary Interiors 269 (2017) 58–90

Contents lists available at ScienceDirect

Physics of the Earth and Planetary Interiors

journal homepage: www.elsevier.com/locate/pepi

Invited Review

Anisotropy in the deep Earth

Barbara Romanowicz [a,b,*], Hans-Rudolf Wenk [a]

[a] Department of Earth and Planetary Science, University of California at Berkeley, United States
[b] Collège de France and Institut de Physique du Globe, Paris, France

ARTICLE INFO

Article history:
Received 11 September 2016
Received in revised form 30 March 2017
Accepted 3 May 2017
Available online 6 May 2017

ABSTRACT

Seismic anisotropy has been found in many regions of the Earth's interior. Its presence in the Earth's crust has been known since the 19th century, and is due in part to the alignment of anisotropic crystals in rocks, and in part to patterns in the distribution of fractures and pores. In the upper mantle, seismic anisotropy was discovered 50 years ago, and can be attributed for the most part, to the alignment of intrinsically anisotropic olivine crystals during large scale deformation associated with convection. There is some indication for anisotropy in the transition zone, particularly in the vicinity of subducted slabs. Here we focus on the deep Earth – the lower mantle and core, where anisotropy is not yet mapped in detail, nor is there consensus on its origin. Most of the lower mantle appears largely isotropic, except in the last 200–300 km, in the D″ region, where evidence for seismic anisotropy has been accumulating since the late 1980s, mostly from shear wave splitting measurements. Recently, a picture has been emerging, where strong anisotropy is associated with high shear velocities at the edges of the large low shear velocity provinces (LLSVPs) in the central Pacific and under Africa. These observations are consistent with being due to the presence of highly anisotropic $MgSiO_3$ post-perovskite crystals, aligned during the deformation of slabs impinging on the core-mantle boundary, and upwelling flow within the LLSVPs.

We also discuss mineral physics aspects such as ultrahigh pressure deformation experiments, first principles calculations to obtain information about elastic properties, and derivation of dislocation activity based on bonding characteristics. Polycrystal plasticity simulations can predict anisotropy but models are still highly idealized and neglect the complex microstructure of polyphase aggregates with strong and weak components. A promising direction for future progress in understanding the origin of seismic anisotropy in the deep mantle and its relation to global mantle circulation, is to link macroscopic information from seismology and microscopic information mineral physics through geodynamics modeling.

Anisotropy in the inner core was proposed 30 years ago to explain faster P wave propagation along the direction of the Earth's axis of rotation as well as anomalous splitting of core sensitive free oscillations. There is still uncertainty about the origin of this anisotropy. In particular, it is difficult to explain its strength, based on known elastic properties of iron, as it would require almost perfect alignment of iron crystals. Indeed, the strongly anomalous P travel times observed on paths from the South Sandwich Islands to Alaska may or may not be due to inner core anisotropy, and will need to be explained before consensus can be reached on the strength of anisotropy in the inner core and its origin.

Contents

---

* Corresponding author at: Department of Earth and Planetary Science, University of California at Berkeley, United States.
E-mail address: barbara@seismo.berkeley.edu (B. Romanowicz).

http://dx.doi.org/10.1016/j.pepi.2017.05.005

1. Background and motivation

The presence of seismic anisotropy in the crust and in the upper mantle is well documented and there is relatively good consensus on its origins, owing to direct observations in the field and laboratory experiments on mineral crystal structure and deformation properties, in a range of pressures and temperatures that is now readily accessible. The situation is much less clear for the deep mantle and core, due on the one hand, to the poor sampling by seismic waves, contamination by upper mantle effects, and, on the other hand, the difficulty for mineral physics deformation experiments to reach the relevant physical conditions. However, there has been significant progress in both fields, in the last decade, and a new and promising approach has emerged, aiming at combining seismic observations of anisotropy in the deep Earth with knowledge from geodynamics modelling and constraints from mineral physics, towards understanding deformation patterns related to global mantle circulation.

Here we review the present state of knowledge on deep mantle and inner core anisotropy in seismology and mineral physics, describe current efforts at linking the two through mantle circulation modeling, and discuss future directions and challenges. First, we start with some historical background.

Anisotropic propagation of sound waves was already described by Green (1838), who introduced Green's functions. Rudzki (1897, 1911) recognized the importance of anisotropic wave propagation in crustal rocks and developed the framework for seismic exploration in the Earth's crust. He highlighted the relationship between the orientation of crystals and fractures in rocks. On the mineral physics side it was D'Halloy (1833) who introduced the expression "texture" to describe directional properties of the rock fabric that was further quantified by Naumann (1850). Voigt (1887) first introduced a quantitative link between elastic properties of single crystals and their orientation with the elastic properties of a textured aggregate. In the following century, these concepts were refined and were applied in materials science as well as geophysics. In exploration geophysics, e.g. of oil deposits, anisotropy became a central issue (e.g. Crampin, 1984; Thomsen, 1986).

It took considerably longer to recognize anisotropy in the deep Earth. At an I.U.G.G. meeting in Berkeley, Raitt (1963) reported azimuthal anisotropy below the Moho in the Mendocino escarpment. Similar anisotropy was observed by Morris et al. (1969) in Hawaii (Fig. 1a). This came at a time when Wegener's (1915) theory of continental drift was revived by Vine and Matthews (1963), documenting magnetic reversals along ridges of upwelling basalts. The structural geologist Hess (1964) immediately interpreted these observations as due to large-scale mantle convection that produced alignment of olivine crystals. The alignment was attributed to crystal plasticity. Cann (1968) further advanced the mantle convection concept (Fig. 1b).

With the advent of global seismic tomography, it became possible to map the patterns of radial and azimuthal anisotropy in the uppermost mantle using fundamental mode surface wave dispersion data. This pattern of azimuthal anisotropy turned out to be quite regular, with an indication of the direction of spreading near mid-ocean ridges (e.g. Fig. 1c, Tanimoto and Anderson, 1985; Montagner and Tanimoto, 1990, 1991), while differences in the velocity of vertically polarized Rayleigh waves and transversely polarized Love waves could point to the location of rising or sinking currents (e.g. Nataf et al., 1984; Montagner, 2002).

While it was generally accepted that alignment of olivine crystals during mantle convection plays a critical role in the development of seismic anisotropy, the mechanism proposed by Hess (1964) was very simple-minded. Olivine crystals do not occur as platelets or needles that float in a viscous liquid and align relative to flow plane and flow direction. Interest in the mantle started experimental research on deformation mechanisms of olivine and associated crystal preferred orientation (CPO), mainly with piston-cylinder deformation apparatus (e.g. Raleigh, 1968 and later Kohlstedt and Goetze, 1974; Jung and Karato, 2001; Jung et al., 2006). It revealed that depending on conditions, different dislocation glide mechanisms are active, with dominant (010)[100] slip at low stress and water content (A-type), dominant (010)[001] slip at high stress (B-type) and (100)[001] slip at high water content, as derived from observations of dislocations by transmission electron microscopy and fabric types in aggregates (e.g. Karato et al., 2008). During dislocation glide, crystals in a polycrystalline aggregate rotate and align. But the deformation pattern in the convecting upper mantle is more complex than a deformation experiment, most commonly performed in axial compression and sometimes in simple shear, and at much higher strain rates than in the Earth.

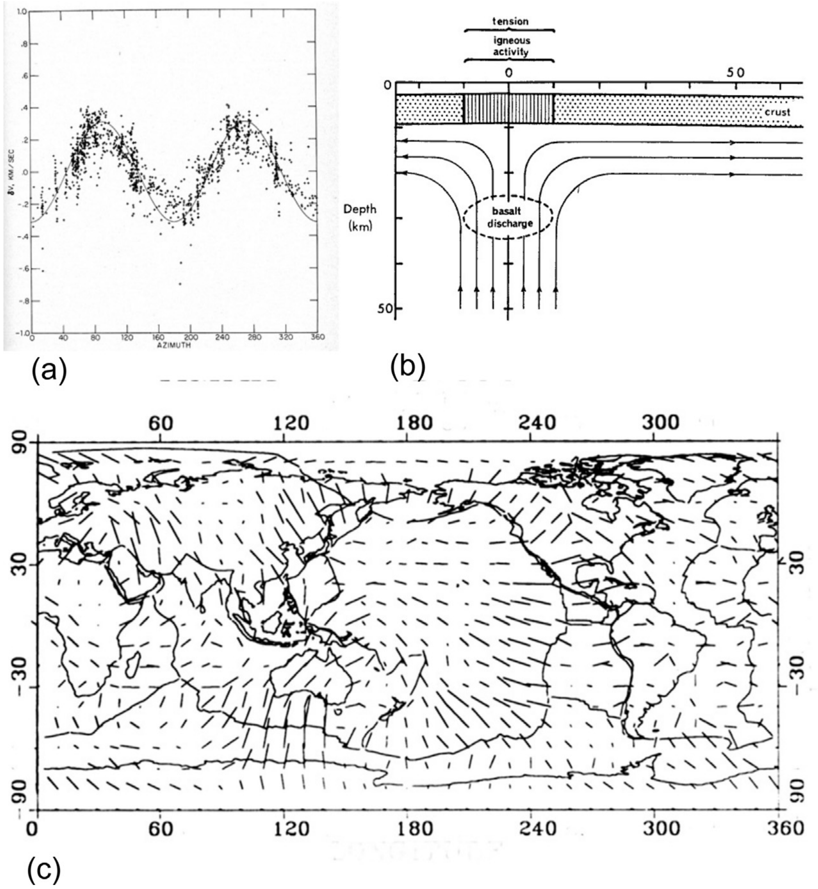

Fig. 1. (a) Azimuthal variation of surface wave velocities in Hawaii (Morris et al. 1969). (b) Proposed model for mantle upwelling at an oceanic ridge (Cann, 1968). (c) Azimuthal anisotropy in Rayleigh waves at a period of 98s (Montagner and Tanimoto, 1990). The lines correspond to fast wave propagation directions, and are proportional to the strength of anisotropy.

Geodynamic models are necessary to suggest realistic deformation paths. Early models assumed flow in an isotropic medium driven by temperature and density gradients (e.g. Hager and O'Connell, 1981; Tackley, 1993; Bunge et al., 1996). Also, subduction of crustal slabs was explored, including rigid slabs (e.g. McKenzie, 1969) as well as more ductile and weak slabs (e.g. Gurnis and Hager, 1988). The development of seismic anisotropy was considered only later by including polycrystal plasticity to explain the development of preferred orientation during plastic deformation (e.g. Blackman et al., 1996; Dawson and Wenk, 2000; Kaminski and Ribe, 2001). We will discuss convection models in more detail below.

Seismic observations revealed that the pattern of anisotropy in the upper mantle is much more complex that the picture in Fig. 1c. This has been reviewed recently (e.g. Long and Becker, 2010; Long, 2013). Here we will focus on anisotropy in the lower mantle and inner core, first from what we know from seismology, and from our current knowledge about mineral physics, particularly elasticity of minerals at deep Earth conditions and deformation mechanisms. Then we will explain how geodynamics modeling is brought into the picture. Great progress has been made in all three fields over the last 20 years. The deep Earth appeared like a simple image, but the more we learn about it, the more complexities arise. In a concluding section, we will highlight some important issues that need to be addressed in the future. There has been a lot of interest in this topic, with many publications in prestigious journals such as Science and Nature, but still a lot of work remains to be done to better describe and understand processes that cause seismic anisotropy at deep Earth conditions.

The purpose of this review is to establish our current state of knowledge and to identify some outstanding questions. It also should serve as an introduction to the field of deep Earth anisotropy for those who are not experts in the field, for example for student projects.

2. Seismic anisotropy in the deep mantle

2.1. Overview

There is as yet no compelling evidence for the presence of significant anisotropy in the bulk of the lower mantle, at least away from subduction zones (e.g. Meade et al., 1995; Montagner and Kennett, 1996; Niu and Perez, 2004; Panning and Romanowicz, 2006; Moulik and Ekström, 2014), although a recent study based on normal mode center frequency observations suggests the presence of anisotropy, as expressed in the radial anisotropy parameter η, already 1000 km above the core-mantle boundary (de Wit and Trampert, 2015). In any case, it is now well established that significant seismic anisotropy is present in the D″ region at the base of the mantle. Here, we review the corresponding observational evidence, which is based on local studies of shear body waves sensitive to the deep mantle, complemented by global tomographic studies of radial anisotropy throughout the mantle.

The first observations of shear wave splitting attributed to anisotropy in the D″ region date back to the late 1980s. Vinnik et al. (1989) observed elliptically polarized S_{diff} waves, for paths sampling the lowermost mantle in the central Pacific, along a direction for which no splitting was present in SKS. Because the absence of the latter indicated that the data were not contaminated by upper mantle anisotropy, they suggested that the splitting originated in the deep mantle and could be due to the presence of anisotropy. Earlier, Mitchell and Helmberger (1973) and Lay and Helmberger (1983) had observed time shifts between the arrival of ScS_H and ScS_V, but attributed them to the presence of a high velocity region at the base of the mantle. Many studies followed in the 1990s, documenting splitting times of up to 10 s in shear waves, such as ScS and S_{diff} (Fig 2), that propagate quasi-horizontally in D″, and interpreted them as indicating the presence of several percent of VTI (Vertical Transverse Isotropy) in the deep mantle (see Lay et al., 1998 and Kendall and Silver, 1998 for early reviews).

As different areas of the world were progressively sampled, the picture that emerged was that globally, the vertically polarized wave (SV) is generally delayed with respect to the horizontally polarized one (SH) in the circum-pacific ring where isotropic shear wave velocities are higher than average in D″. On the other hand, intermittent splitting and sometimes delayed SH with respect to SV was observed on paths sampling the large low shear velocity provinces (LLSVPs) in the central Pacific and under Africa (Fig. 3). Additional reports of splitting in ScS and S_{diff} have been published in the last two decades, most of them attributed to anisotropy in D″. A review of observations of shear wave splitting originating in D″ can be found in Wookey and Kendall (2007) and Nowacki et al. (2011) as well as Lay (2015). Here we focus primarily on the most recent contributions, while an updated list of observations is given in Table 1 and Fig. 3.

Several important challenges affect studies of shear wave splitting in D″. One is the necessity to account for (or avoid) contamination of seismic waveforms by strong upper mantle anisotropy sampled by the body waves considered (Fig. 2). Another challenge is the poor azimuthal sampling of D″ at any given location, due to the limited global distribution of earthquake sources and receivers. This makes it difficult to distinguish between different possible causes of anisotropy, whether due to periodic layering or crystal alignment, and whether the nature of the anisotropy is transverse isotropy with a vertical (VTI) or tilted (TTI) axis of symmetry, or perhaps involves more complex symmetries. Also, in the case of S_{diff}, an apparent delay of SV_{diff} may be due to waveform distorsion in a laterally heterogeneous, but isotropic, structure, due to the fact that the amplitude of SV_{diff} decays rapidly with distance in regions of fast isotropic velocity (e.g. Vinnik et al., 1995; Komatitsch et al., 2010). More generally, apparent splitting in S waves sampling the D″ region may sometimes be due to other causes than anisotropy, such as propagation in a complex heterogeneous medium near the boundary between the solid mantle and the liquid core, which requires more sophisticated modeling than infinite frequency ray theory (Monteiller and Chevrot, 2010; Borgeaud et al., 2016; Nowacki and Wookey, 2016). Careful waveform analysis is therefore necessary before attributing splitting observations to anisotropy. Some of the splitting results listed in Table 1 may need to be re-evaluated in that context. However, consistency in the splitting results obtained using different types of waves across a number of regions of the world, and in some cases detailed waveform modeling, indicates that in general, invoking anisotropy as a cause for the observed splitting, is a robust result. At the present time, interpretation in terms of layering or CPO requires invoking possible constraints from other fields than seismology, and remains uncertain.

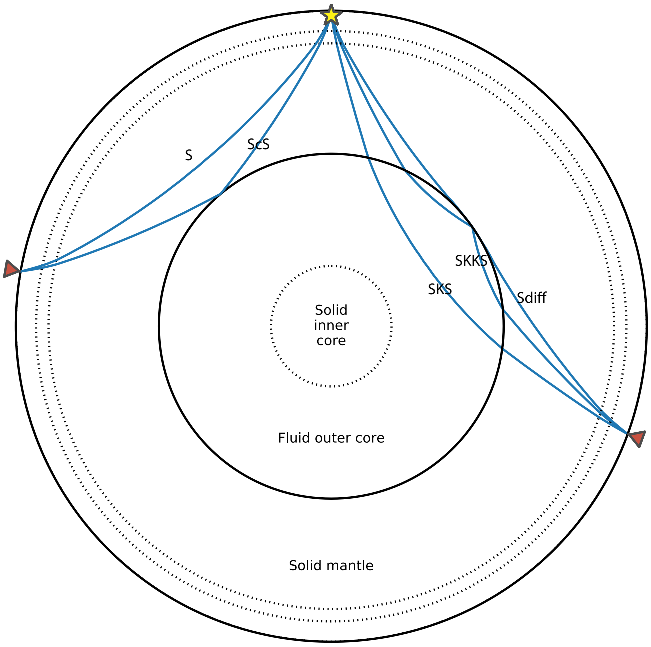

Fig. 2. Raypaths through the Earth of the main seismic body wave phases used for studying anisotropy in the deep mantle. Asterisk is earthquake location, triangles are receiver stations.

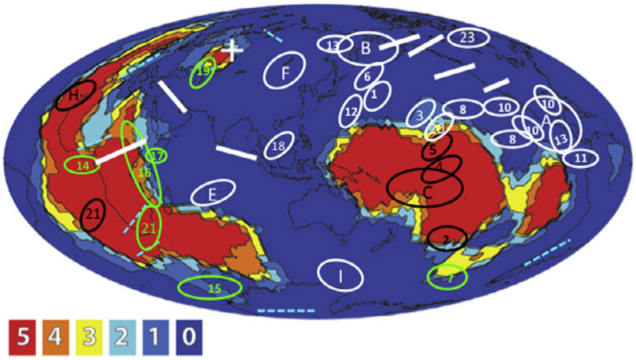

Fig. 3. Background: "Voting map" based on 5 shear wave velocity tomographic models modified (from Lekic et al., 2012). Locations in D″ where 5 models agree that Vs is lower than average or higher than average are shown in red and dark blue, respectively. White ellipses indicate locations where shear wave splitting observations with Vsh > Vsv have been attributed to anisotropy in D″. These include regions where azimuthal anisotropy has been reported. Green ellipses indicate regions where strong lateral variations of anisotropy in D″ have been reported, at the edges of the African LLSVP (14, 17, 21), the Perm anomaly (19) and in the south Pacific (7,19). Blue ellipses with broken lines indicate regions where Vsv > Vsh has been reported and/or null splitting. See Table 1 for references to numbers and letters. White bars and blue broken lines (no splitting) are from Niu and Perez (2004).

2.2. Accounting for upper mantle anisotropy

In order to account for upper-mantle anisotropy, an approach taken in early studies of S_{diff} splitting was to only consider deep earthquakes and paths for which SKS and SKKS do not present any evidence of splitting (e.g. Vinnik et al., 1989, 1995). Selecting observations for deep earthquakes assures that contamination by anisotropic effects in the upper mantle on the source side can largely be avoided. On the station side, the paths of S_{diff} and SKS/SKKS are very close in the upper mantle (Fig 2), while they diverge in the deep mantle. Also, only S_{diff} spends significant time within D″. The absence of splitting in SKS/SKKS indicates that either there is no anisotropy in the upper mantle region sampled on the receiver side, or the direction of the great circle path is along the null splitting direction. Any splitting observed in S_{diff} can thus be attributed to the deep mantle.

However, such geometries are exceptional. Therefore it is important to find ways to correct for the widespread and strong

Table 1
Summary of local studies of anisotropy in D″

	Authors	Region	Type of seismic waves
$V_{SH} > V_{SV}$			
A	Wookey and Kendall (2007)	Caribbean	
	and Refs. therein:		
	Kendall and Silver (1996)	Caribbean	S,Sdiff
	Ding and Helmberger (1997)	Caribbean	ScS
	Rokosky et al. (2004)	Caribbean	ScS
B	Wookey and Kendall (2007)	Alaska	
	and Refs. therein:		
	Lay and Young (1991)	Alaska	S,ScS
	Matzel et al. (1996)	Alaska	S,ScS,Sdiff
	Garnero and Lay (1997)	Alaska	S,ScS,Sdiff
	Wysession et al. (1998)	Alaska	Sdiff
	Fouch et al. (2001)	Alaska	S,Sdiff
E	Ritsema (2000)	Indian Ocean	S
F	Thomas and Kendall (2002)	Siberia	S,ScS,Sdiff
I	Usui et al. (2008)	Antarctic Ocean	S
1	Kendall and Silver (1998)	NW Pacific	S,ScS,Sdiff
3	Vinnik et al. (1995, 1998b)	north central Pacific	Sdiff
6	Wookey et al. (2005b)	N. Pacific	ScS
8	Long (2009)	East Pacific	SKS-SKKS
9	Niu and Perez (2004)	N. America, Asia	SKS/SKKS
11	Vanacore and Niu (2011)	Caribbean	SKS-SKKS
12	He and Long (2011)	NW Pacific	PcS,ScS, SKS, SKKS
13	Wookey and Kendall (2008)	Caribbean	ScS
18	Thomas et al. (2007)	W Pacific	ScS
20	Fouch et al. (2001)	North central Pacific	S,Sdiff
SV < SH			
4	Pulliam and Sen (1998)	Central Pacific	S
C	Ritsema et al. (1998)	Central Pacific	S,Sdiff
22	Kawai and Geller (2010)	Central Pacific	S,ScS,SKS
Tilted/azimuthal/laterally varying			
5	Russell et al. (1998, 1999)	North Central Pacific	ScS
7	Ford et al. (2006)	South Pacific	S,Sdiff
A	Garnero et al. (2004a)	Caribbean	S,ScS,Sdiff
A	Maupin et al. (2005)	Caribbean	S,ScS,Sdiff
A	Rokosky et al. (2004, 2006)	Caribbean	ScS
G	Wookey et al. (2005a)	North West Pacific	ScS
23	Restivo and Helffrich (2006)	North America	SKS, SKKS
21	Wang and Wen (2007)	East/South Africa	SKS,SKKS
10	Nowacki et al. (2010)	Caribbean/west US	ScS
14	Lynner and Long (2012)	Central Africa	SKS-SKKS
15	Cottaar and Romanowicz (2013)	South edge of African LLSVP	Sdiff
16	Lynner and Long (2014)	East/South Africa	SKS-SKKS
19	Long and Lynner (2015)	Near Perm Anomaly	SKS-SKKS
17	Ford et al. (2015)	East Africa	SKS-SKKS
Isotropic or weak anisotropy			
2	Kendall and Silver (1996)	South Pacific	S,ScS,Sdiff
H	Garnero et al. (2004b)	Atlantic	S,Sdiff
9	Niu and Perez (2004)	South Africa, Antarctica, Southeast Pacific	SKS,SKKS
21	Wang and Wen (2007)	Eastern Atlantic	SKS,SKKS

upper mantle anisotropy sampled along the path of deep mantle seismic waves. For example, Vinnik et al. (1998a) proposed a reference event method to correct S_{diff} waveforms for unknown upper mantle anisotropy using SKS and SKKS waveforms. In the past two decades, characterization of upper mantle anisotropy from SKS splitting data has progressed significantly (see review by Long and Silver, 2009), making it possible to apply relatively robust corrections in ″known″ upper mantle models, both on the source and receiver sides, and thus augment the number of D″ locations that can be sampled.

Another approach to minimize effects of upper mantle anisotropy has been the use of differential measurements on pairs of phases. One such suitable pair is S and ScS, which have similar paths in the upper mantle on the source and station side, but, at appropriate distances, only ScS samples D″ (Fig. 2), while S samples a portion of the lower mantle which is assumed to be isotropic (e.g. Wookey et al., 2005a; Nowacki et al., 2010). Similarly, while SKS and SKKS splitting is most strongly acquired during propagation in the upper mantle, the paths of SKS and SKKS waves diverge significantly in the lowermost mantle, so that differential splitting of these two phases can sometimes be attributed to anisotropy in the deep mantle (e.g. Hall et al., 2004; Niu and Perez, 2004; Restivo and Helffrich, 2006; Wang and Wen, 2007). Such an approach has been applied to several regions of the world (e.g. Long, 2009; He and Long, 2011; Vanacore and Niu, 2011; Lynner and Long, 2012, 2014; Long and Lynner, 2015; Ford et al., 2015). Results consistently show strong and complex anisotropy on the borders of the LLSVP's, and interestingly, also in the vicinity of the Perm Anomaly (Long and Lynner, 2015), a low velocity anomaly seen at the base of the mantle in all tomographic models in the vicinity of the town of Perm (Russia), and of smaller lateral extent (~ 900 km) but corresponds to a similar reduction in shear velocity as found in the LLSVPs (e.g. Lekic et al., 2012; Fig. 3).

2.3. Results from array studies

Earlier observations and forward modeling studies of D″ anisotropy mostly relied on data from isolated stations, which made it difficult to constrain the geometry of anisotropy, for lack of sampling of the target regions by waves propagating in different directions (e.g. Maupin, 1994). Thus, most studies only reported the differences in SH and SV propagation times, leading to models of apparent VTI. Yet, evidence for azimuthal anisotropy has been suggested, either from waveform complexity (e.g. Garnero et al., 2004a; Maupin et al., 2005) or, when the geometry permitted, from measurements of splitting on paths sampling the target region in at least two directions (e.g. Wookey and Kendall, 2008). With the advent of denser broadband arrays, more detailed studies have emerged in recent years, aiming at the very least, to distinguish VTI from radial anisotropy with tilted axis of symmetry (TTI), with implications for the interpretation of observations in terms of intrinsic or extrinsic anisotropy (e.g. Long et al., 2006).

Regions of the world where this has been possible so far are central America, exploiting ScS, S data from the dense USArray (Nowacki et al., 2010), and the northwest Pacific (He and Long, 2011), using ScS data from F-net in Japan. Studies of S_{diff} at the southern border of the African LLSVP, based on data from the Kaapval array, show lateral variations in anisotropy (To et al., 2005; Cottaar and Romanowicz, 2013), with strong anisotropy in the fast velocity region outside the LLSVP, increasing towards its border and apparently disappearing inside it. Although caution must be taken when interpreting apparent splitting in S_{diff}, due to isotropic heterogeneity potentially affecting SV_{diff} in a significant way (Komatitsch et al., 2010), the strong elliptical shape of the particle motion outside of the African LLSVP (Fig. 4 and To et al., 2005), where isotropic velocities are relatively fast, contrasting with the linear particle motion for paths travelling inside the LLSVP cannot be accounted for by isotropic heterogeneity. This was demonstrated in the follow-up study of Cottaar and Romanowicz (2013), in which the waveforms of Fig. 4 and others were modelled using the spectral element method, a numerical method for 3D seismic wavefield computations, which can take effects of 3D isotropic heterogeneity into account accurately. Differential splitting in S and ScS has also been exploited in the north Pacific (Wookey et al., 2005a) and in east Africa (Ford et al., 2015), where, remarkably, several azimuths can be sampled.

The recent studies have confirmed earlier results, with, in general, Vsh> Vsv in the ring of faster than average velocities surrounding the two LLSVPs, and absence of significant splitting, or Vsh<Vsv found primarily within the LLSVPs (Fig. 3, Table 1).

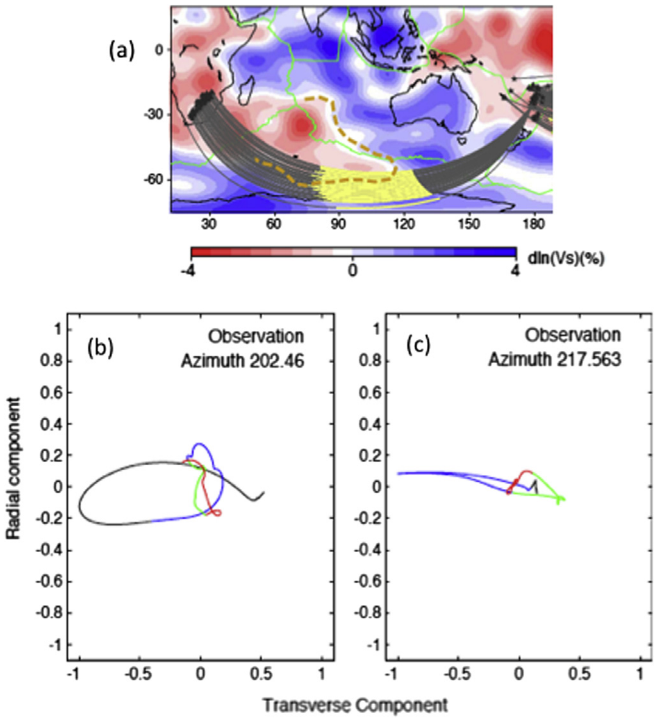

Fig. 4. Example of change of character of particle motion for paths sampling the border of the African LLSVP. (a) Map showing the paths sampled plotted on top of a background shear wave tomographic model (SAW24B16, Mégnin and Romanowicz, 2000). The portion of path sampling the D″ region is highlighted in yellow. (b) and (c) shows particle motions of Sdiff at distances of ∼ 120° and at two azimuths: In (b) the path in D″ is outside of the LLSVP and in (c), the path in D″ is inside the LLSVP (from To et al., 2005). The color indicates the time with respect to predicted Sdiff arrival from PREM. Black: −35 to −5 s, Blue: −5 to 20 s, Green 20 to 45 s, Red 45 to 70 s. The elliptical particle motion in (B) contrasts with the linear particle motion in (c). This cannot simply be explained by lateral heterogeneity in isotropic velocity, as one would expect larger amplitudes in SV for waves propagating inside the low velocity LLSVP. This interpretation was later confirmed by 3D numerical waveform modelling (Cottaar and Romanowicz, 2013). (For interpretation of the references to color in this figure legend, the reader is referred to the web version of this article.)

The recent results indicate variability of anisotropy at relatively short scales, with evidence for azimuthal anisotropy with different orientations of fast velocity axes, at least in regions of faster than average isotropic shear velocity. Interestingly, the studies of Cottaar and Romanowicz (2013), Lynner and Long (2014) and Ford et al. (2015), consistently show changes in anisotropy across the border of the African LLSVP, with stronger anisotropy outside of it, practically disappearing inside it (e.g. Fig. 5). Interestingly, the same trend, although less sharply defined because of the challenging geometry, is likely present at the northern edge of the Pacific LLSVP (Fig. 6). Indeed, all studies of the latter region consider paths from Fiji-Tonga sources to stations in north America. Different results are found for different distance ranges, with Vsv>Vsh for the shorter distances, sampling inside the LLSVP (as well as above D″), and Vsh>Vsv at longer distances (Sdiff) which sample a significant portion of the fast Vs region outside of the LLSVP. Vinnik et al. (1995, 1998b) used S_{diff} data and found $V_{SH}>V_{SV}$; the portion of the corresponding paths inside the LLSVP was small and Vinnik et al. (1998b) showed that splitting only occurred for distances larger than 102°, when paths sampled more of the fast region outside of the LLSVP. Likewise, Fouch et al. (2001) and Ritsema et al. (1998) used S, Sdiff and found Vsh>Vsv for larger distance paths, while Vsv>Vsh for shorter distance paths that sample within the LLSVP and above D″, as did Kawai and Geller (2010). Pulliam and Sen (1998) and Russell et al. (1998) used S and ScS, respectively, at shorter distances, sampling inside the LLSVP, and found Vsv>Vsh.

All these results point in the same direction: evidence for significant anisotropy with generally Vsh>Vsv within the ring of fast velocities surrounding the Pacific and African LLSVP, possibly increasing and tilting at their borders, but vanishing or changing sign (Vsv>Vsh) inside the LLSVP's.

2.4. Results from global anisotropic tomography

Gaining improved understanding of the distribution and nature of seismic anisotropy at the base of the mantle requires better global sampling with accurate corrections for upper mantle anisotropy. One possible approach is to construct global whole mantle tomographic models of anisotropy. Such an approach is attractive, because a variety of seismic waveforms can be included, in particular fundamental and overtone surface waves, which provide constraints on the strong anisotropy in the uppermost mantle (e.g. Debayle and Ricard, 2013). Combining surface wave data with various body waveforms that illuminate the entire mantle should ultimately allow improved resolution and characterization of deep mantle anisotropy. So far, this has proven very challenging for the deep mantle.

Indeed, most successful has been the tomographic characterization of shear wave azimuthal anisotropy in the uppermost 200 km of the mantle at the global scale using Rayleigh wave dispersion data (e.g. Tanimoto and Anderson, 1984; Montagner and Tanimoto, 1990, 1991, Fig. 1). More recent models developed by different groups show broadly consistent trends (e.g. Trampert and Woodhouse, 2003; Ekström, 2011; Debayle and Ricard, 2013; Yuan and Beghein, 2013). On the other hand, the robustness of global scale transition zone azimuthal anisotropy models that utilize surface wave overtone information (e.g. Trampert and van Heijst, 2002; Yuan and Beghein, 2013) is still debated. This is because the anisotropic signal in overtone surface waves is weak, the azimuthal sampling far from ideal, and the number of parameters needed to invert for azimuthal anisotropy at the global scale, even when considering only the dominant terms in 2-ψ (where ψ is the azimuth) is very large, likely resulting in trade-offs with isotropic structure. It is not possible at present to extend this type of study to the deep mantle, as the sensitivity of available long period overtone data becomes too weak and azimuthal coverage for body waves provided by the current geometry of sources and stations is not sufficient.

Thus, tomographic imaging of anisotropy in the whole mantle can, at present, only hope to resolve the simplest form of anisotropy that does not have as strong requirements on azimuthal coverage, which is VTI (or apparent VTI). Such studies are based on relatively long period waveforms, mostly sensitive to shear velocity, combining fundamental mode surface waves, surface wave overtones and shear body waves, and aim at solving for the distribution of only two anisotropic parameters: Vsh and Vsv, or, alternatively, isotropic velocity Vs_{iso} and the anisotropic parameter $\xi = (Vsh/Vsv)^2$ (Panning and Romanowicz, 2004, 2006; Panning et al., 2010; Kustowski et al., 2008; French and Romanowicz, 2014; Moulik and Ekström, 2014; Auer et al., 2014; Chang et al., 2014, 2015). The other three anisotropic parameters that are necessary to fully describe a VTI medium are scaled to Vs_{iso} and ξ, using scaling relations that are appropriate for the upper mantle (e.g. Montagner and Anderson, 1989), but may be questionable for the lower mantle. However, this may not be a significant issue given the dominant sensitivity of the waveforms considered to shear velocities. While the resulting models show qualitative agreement at long wavelengths, details vary from model to model significantly enough not to be trustworthy for quantitative interpretations.

These models do agree on the following observations: on average, radial anisotropy is strongest in the uppermost mantle, and most of the lower mantle exhibits little radial anisotropy (Fig. 7).

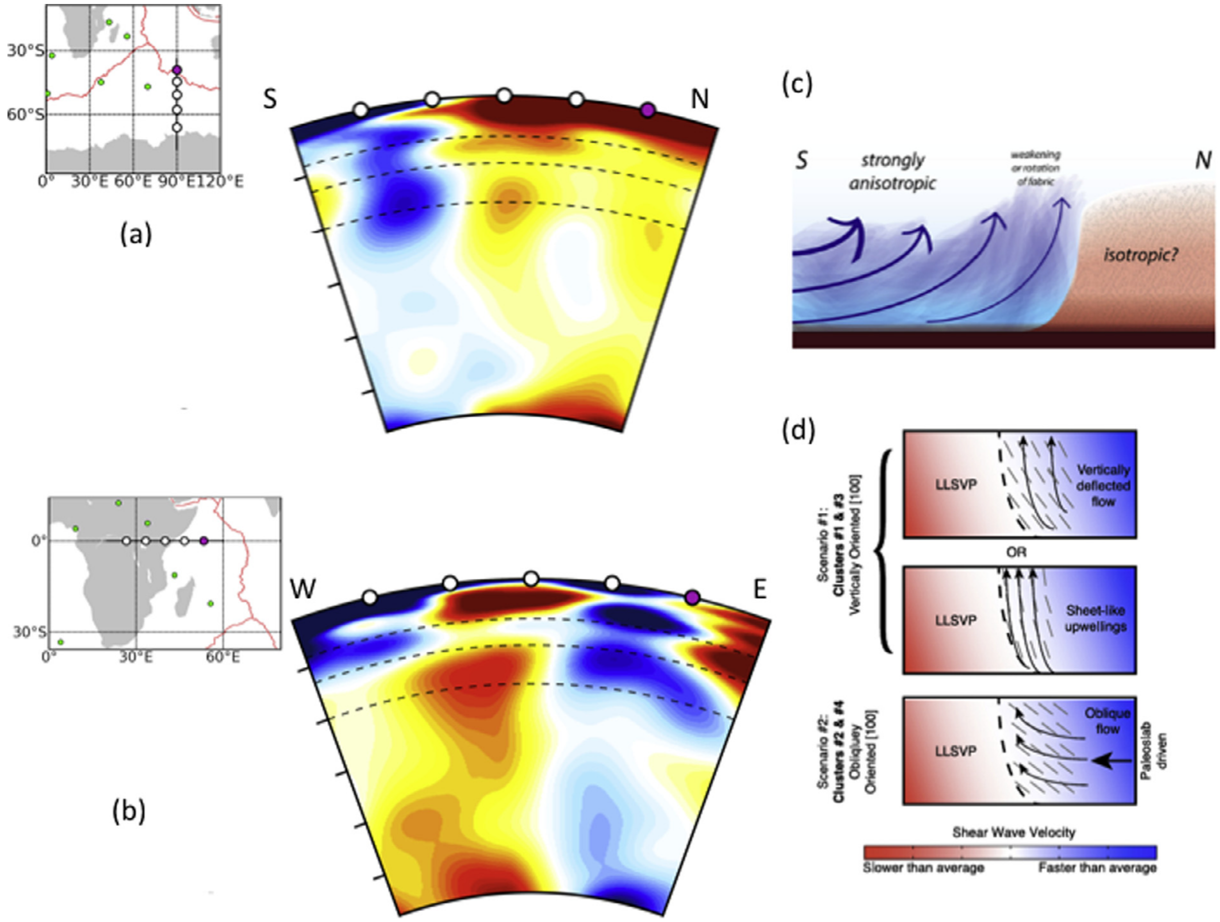

Fig. 5. a and b: Whole mantle depth cross sections through the isotropic Vs part of model SEMUCB_WM1 (French and Romanowicz, 2014) at the southern (a) and eastern (b) edge of the African LLSVP, where rapid variations in the direction and strength of anisotropy have been reported, decreasing from outside (blue) to inside (pink) the LLSVP. in c) the map view is from Lynner and Long (2014) with background shear velocity model GyPSuM of Simmons et al. (2012). The cross-section location is indicated on the map by a straight line. c and d: corresponding cartoons proposed by the authors, respectively (c) Cottaar and Romanowicz (2013); (d) Ford and Long (2015).

In most models, there is an indication of an increase in anisotropy in D″, with Vsh> Vsv (ξ slightly larger than 1), although there is variability among models, due to a combination of parametrization, types of seismic waves considered, and theoretical assumptions.

Common 3D features of these models in D″ are a predominance of Vsh > Vsv outside of the LLSVPs, with patches of Vsh < Vsv confined within the LLSVPs, in agreement with local studies (Fig. 8). However, the current models do not show consistency in the amplitude of the lateral variations in ξ, nor the wavelengths of these variations. This is partly due to the parametrization chosen. For example, Panning and Romanowicz (2004, 2006) and Auer et al. (2014) allowed relatively short wavelength lateral variations in ξ, while Moulik and Ekström (2014) and French and Romanowicz (2014) chose to assign shorter wavelength lateral variations to isotropic Vs, while constraining the anisotropic part of the model to be smooth. Theoretical assumptions on wave propagation are also important: ray theory is not valid for modelling of S_{diff}, nor is it valid to use the surface wave approximation for modelling this phase, as shown by Li and Romanowicz (1995). So far, only the Berkeley models are constructed taking into account finite frequency effects rather than ray theory for body waves (Panning and Romanowicz, 2004, 2006; French and Romanowicz, 2014).

One fundamental issue is that S_{diff} and ScS_n data (with n>1) are necessary to obtain good coverage of D″ at the global scale. As discussed previously, SV_{diff} decays rapidly with distance in models such as the reference model PREM (Dziewonski and Anderson, 1981) where the velocity in D″ is relatively fast. The global datasets are thus necessarily biased, although to various degrees depending on the particular dataset, by the predominance of SH_{diff}, introducing trade-offs between isotropic and anisotropic structure (e.g. Kustowski et al., 2008; Chang et al., 2015), and making it only possible to resolve the very longest wavelengths of VTI in D″, with poor constraints on their amplitude.

In summary, robustly mapping even the simplest component of seismic anisotropy, apparent VTI, at the base of the mantle, at high resolution using a tomographic approach is still a challenging open question, let alone constraining azimuthal anisotropy at the global scale. Still, available global models agree with local studies about the prevalence of Vsh>Vsv in regions of faster than average velocity in D″.

As for P wave anisotropy in the deep mantle, only few studies have tried to constrain it so far. Several studies have attempted to retrieve the global average variation with depth of the radially anisotropic parameter $\eta = (Vph/Vpv)^2$ using normal mode data (Montagner and Kennett, 1996; Beghein et al., 2006), finding some indication that the anisotropy in η may be anticorrelated with that of ξ in the D″ region, with, however, strong trade-offs with density (to which normal mode data are also sensitive). Note that the anticorrelation of isotropic P and S velocities, at long wavelengths, in the deep mantle is, in contrast, better established (e.g. Su and Dziewonski, 1997; Kennett and Widyantoro, 1998; Masters et al., 2000; Ishii and Tromp, 1999; Romanowicz and Bréger, 2000). The possibility of P wave anisotropy in the deep mantle using P wave data (mantle and core phases) has been investigated by Boschi and Dziewonski (2000), concluding that anisotropy may be small with significant trade-offs with core-mantle boundary topography

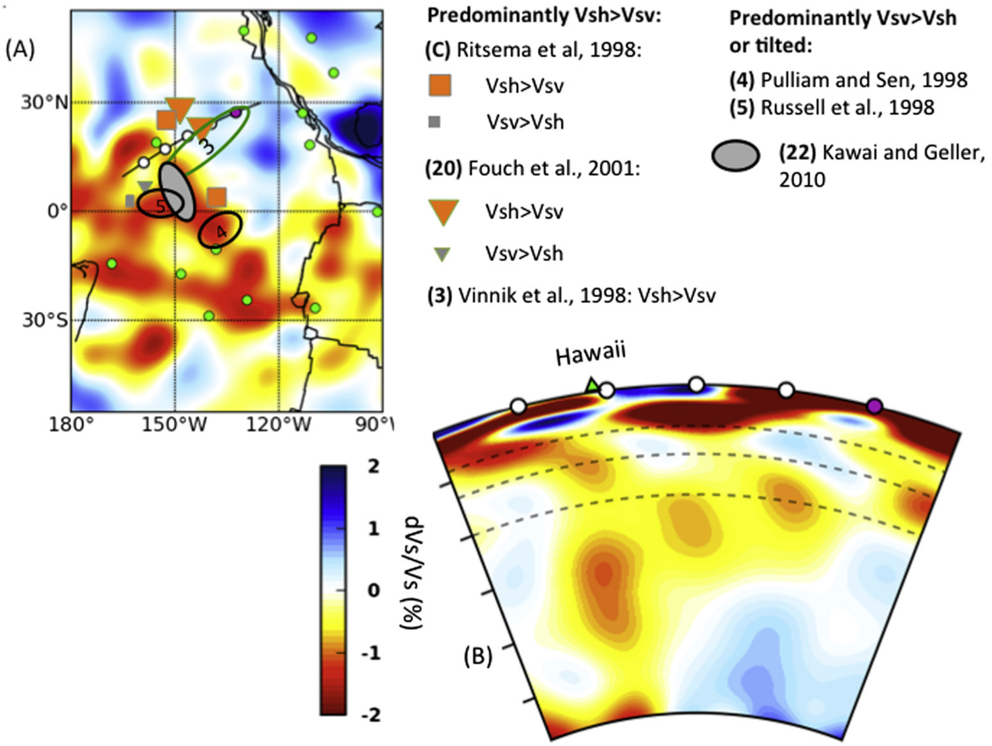

Fig. 6. Zoom on the northern edge of the Pacific LLSVP. The background tomographic model is the isotropic Vs part of model SEMUCB_WM1 (French and Romanowicz, 2014). (A) Map view, with locations of studies of D″ shear wave splitting suggesting a change of character of anisotropy across the boundary of the LLSVP. Green dots indicate the location of major hotspots. Black line with white and purple dots is the great circle path corresponding to the depth cross section shown in (B), displaying the Hawaiian plume and transition from low to fast velocities in D″. Kawai and Geller (2010), Pulliam and Sen (1998) and Russell et al. (1998) find $V_{SV} > V_{SH}$ while Ritsema et al. (1998), Fouch et al. (2001) and Vinnik et al. (1998) find that Vsh > Vsv, increasingly so for paths sampling the fast region outside of the LLSVP. Note that the color saturation of the tomographic model is different in (A) and (B).

and outer core structure. The possible anticorrelation of P and S radial anisotropy in the D″ must therefore be considered with caution, at the present time, when used as a constraint in modeling.

Given these difficulties, a currently explored possible avenue is to try and combine constraints not only from seismology but also from mineral physics and geodynamics. Each of these approaches, taken individually, involves many assumptions and uncertainties, but by combining them, the hope is that the space of acceptable models for anisotropy and its causes can be further reduced. The idea is to start with the strain field inferred from a mantle circulation model, compute the corresponding texture development and predicted seismic anisotropy using available information on crystal plasticity and elasticity for different lower mantle minerals, and compare these predictions with seismic observations. This should provide constraints on the mineral physics assumptions as well as the deep mantle dynamics, or at least allow us to rule out some classes of models. Note that in this approach, the fundamental assumption is that anisotropy is due to CPO development resulting from large-scale mantle flow.

Before describing these efforts in more detail, we will review current knowledge and capabilities in mineral physics and describe how seismology and mineral physics can be linked through geodynamics modeling.

3. Mineral physics perspective on the deep mantle

3.1. Dominant mineral phases in the lower mantle

Ringwood (1962) speculated about the composition of the lower mantle, suggesting that olivine Mg_2SiO_4 would first break down to spinel Mg_2SiO_4, and then to $MgSiO_3$ with a "corundum-like" structure and periclase (MgO). Liu (1974) synthesized this structure at high temperature and pressure and identified it as $MgSiO_3$ perovskite (which has recently been named bridgmanite, Tschauner et al., 2014). At high pressure, bridgmanite transforms to post-perovskite, pPv (e.g. Murakami et al., 2004; Oganov and Ono, 2004; Tateno et al., 2009, Fig. 9a) and this may be the most important phase near the core-mantle boundary, particularly along a cold geotherm within subducting slabs (Fig. 9b). Thus it appears that cubic periclase (Fig 10a), orthorhombic bridgmanite (Fig 10b) and orthorhombic post-perovskite (Fig. 10c) are the dominant minerals in the lower mantle. Periclase has the same highly symmetric structure as halite (NaCl) with close-packed MgO^{VI} octahedral coordination polyhedra. Bridgmanite (spacegroup Pbnm) is a distorted cubic perovskite structure with SiO^{VI} coordination octahedra linked over corners and Mg^{2+} in large interstices. Post-perovskite (spacegroup Cmcm) has layers of SiO^{VI} octahedra alternating with layers of Mg. The layers are parallel to (010). It is isostructural with $CaIrO_3$ (e.g. Hunt et al., 2009). While the pseudocubic perovskite structure is elastically fairly isotropic, the layered post-perovskite structure is highly anisotropic. As we will see, post-perovskite is of critical importance for anisotropy in the lower mantle. In the following discussion we will use mostly the abbreviation pPv.

Most lower mantle minerals (>660 km) cannot be studied at surface conditions. Even if lower mantle material has reached the surface by upwelling, minerals have undergone phase transitions. Thus information about phase diagrams is based on *in situ* observations in high pressure experiments and *ab initio* calculations.

Irifune and Tsuchiya (2015) have reviewed the mineralogical composition of the lower mantle. Different bulk compositions of the lower mantle have been proposed. Ringwood (1962, 1975) suggested a peridotitic-"pyrolitic" composition (Fig. 11a). Subducting

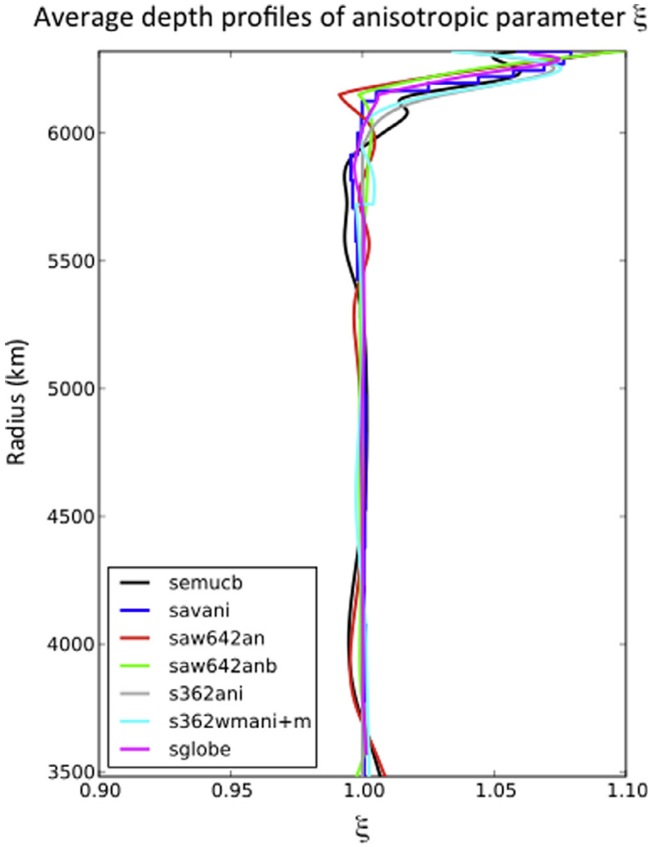

Fig. 7. Comparison of depth profiles throughout the mantle of global average radial anisotropy parameter $\xi = (V_{sh}/V_{sv})^2$, in 6 recent global shear velocity models. $\xi = 1$ corresponds to isotropy. Model S362ANI (Kustowski et al., 2008) is isotropic in the lower mantle. While there are differences between models, all of them agree that radial anisotropy is strongest in the first 200 km of the mantle and very weak in most of the lower mantle. In D″, on average V_{sh} is equal of slightly faster than V_{sv}.

slabs may correspond to more siliceous, aluminous and Ca-rich mid-ocean ridge basalts (MORB, e.g. Irifune and Ringwood, 1993, Fig. 11b). In both cases $MgSiO_3$-perovskite (bridgmanite) dominates in large volumes of the lower mantle but for MORB compositions, high pressure silica and alumina phases are also significant, and there may be no ferropericlase. Calcium perovskite ($CaSiO_3$) is cubic (spacegroup Pm3 m) at lower mantle conditions (e.g. Wang et al., 1996; Kawai and Tscuchiya, 2015) and is an important component at depths beyond 750 km. It distorts to a tetragonal structure at low temperature and high pressure (e.g. Shim et al., 2002).

As more details about the lower mantle are revealed, compositional heterogeneities become apparent (e.g. Badro et al., 2003; Li, Y. et al., 2014). Higher concentrations of Si, Al and Fe add considerable complexity. The diverse composition is in part the result of subduction of slabs composed of crust and upper mantle. Silica (SiO_2) may exist as stishovite with a rutile structure and 6-fold coordination, or at higher pressure as a cubic phase with $CaCl_2$. structure and 8-fold coordination (e.g. Kingma et al., 1995) and at even higher pressure as an orthorhombic (Pbcn) α-PbO_2 structure (seifertite) (e.g. Dubrovinsky et al., 2004; Grocholski et al., 2013; Zhang et al., 2016). According to first principles calculations, at extreme pressure SiO_2 may transform to a pyrite structure (Kuwayama et al., 2005). Al_2O_3 in the form of trigonal corundum or orthorhombic Rh_2O_3(II) may be present, and Fe may exist as native iron (e.g. Frost et al., 2004; Shi et al., 2013).

Of considerable importance is the oxidation state as well as the spin state of iron that have received a lot of attention (e.g. McCammon, 1997; Badro et al. 2003; Li et al. 2004; Tsuchiya et al., 2006; Fei et al., 2007; Lin et al., 2008; Catalli et al., 2010; Saha et al., 2011, 2012; Vilella et al., 2015). With increasing pressure, there is a transition from a high spin to a low spin configuration. It may be responsible for the anomalous viscosity structure in the central part of the lower mantle (900–1200 km, e.g. Rudolph et al., 2015), although the spin transition is generally thought to occur deeper (~1500 km).

In addition, hydrogen may play a significant role (e.g. Ohtami and Sakai, 2008). A hydrous aluminosilicate is stable at lower mantle conditions (e.g. Tsuchiya and Tsuchiya, 2008, 2011; Pamato et al., 2014) and dehydration may cause melting at the top of the lower mantle (Schmandt et al., 2014).

As far as elastic properties and anisotropy are concerned, one should keep in mind that the major phases over large volumes of the lower mantle are bridgmanite, ferropericlase, pPv and $CaSiO_3$ perovskite. These contribute largely to the bulk elastic properties, but there may be local deviations.

3.2. Some comments on plasticity models and representation of anisotropy

What are the sources of seismic anisotropy in the Earth? Very important is the alignment of anisotropic crystals called crystal preferred orientation (CPO) or texture (based on D'Halloy, 1833) and universally used in materials science. The crystal anisotropy is linked to the crystal structure. A second aspect is crystal shape that produces a shape-preferred orientation (SPO). CPO and SPO are sometimes linked (in mica, for example, the crystal plane (001) is parallel to the platelet). Often it is not (e.g. in quartz or in periclase). Also significant is the orientation of flat fractures and fractures filled with kerogen. This is a very important contribution to anisotropy in shales (e.g. Hornby et al., 1994; Sayers, 1994; Vasin et al., 2013) but insignificant in the lower mantle. In the lower mantle there is the possibility of partial melt, particularly near the core-mantle boundary (e.g. Williams and Garnero, 1996; Lay et al., 2004; Shi et al., 2013) but this would only give rise to anisotropy if melt occurred in parallel thin layers (e.g. Backus, 1962). We will focus here on the development of CPO.

Before going into plasticity in the mantle, a few words about deformation mechanisms of polycrystalline aggregates are in order. Deformation experiments on minerals have a long history. Pfaff (1859) documented mechanical twinning in calcite when a stress is applied. In the early twentieth century deformation experiments at a wide range of temperature and strain conditions were conducted on metals to explore the deformation behavior (e.g. Schmid, 1924) and in this context linear defects called dislocations were discovered (Polanyi, 1934; Taylor, 1934). Without dislocations it would be very difficult to deform crystals and indeed they are present in most crystalline materials.

Dislocations form in the crystal lattice when a stress is applied. Edge dislocations propagate on a glide plane (*hkl*) and in a slip direction [uvw], defined by rational indices relative to crystallographic axes. Propagation of dislocations causes crystals to rotate relative to the applied stress, which is conceptually illustrated for an experimentally compressed single crystal in Fig. 12. By movement of dislocations on glide planes the rectangular crystal attains a new shape (parallelogram). Since pistons must stay in contact this results in an effective rotation of β. In a polycrystalline aggregate neighboring grains play the function of pistons.

Based on deformation experiments on metals, deformation mechanism maps were established (e.g. Ashby, 1972; Langdon and Mohamed, 1978; Frost and Ashby, 1982). They define conditions such as temperature, pressure, stress magnitudes, strain rate and grain size under which mechanisms such as dislocation glide, dislocation climb, grain boundary migration and grain boundary sliding are active (Fig. 13). Identifying mechanisms is important

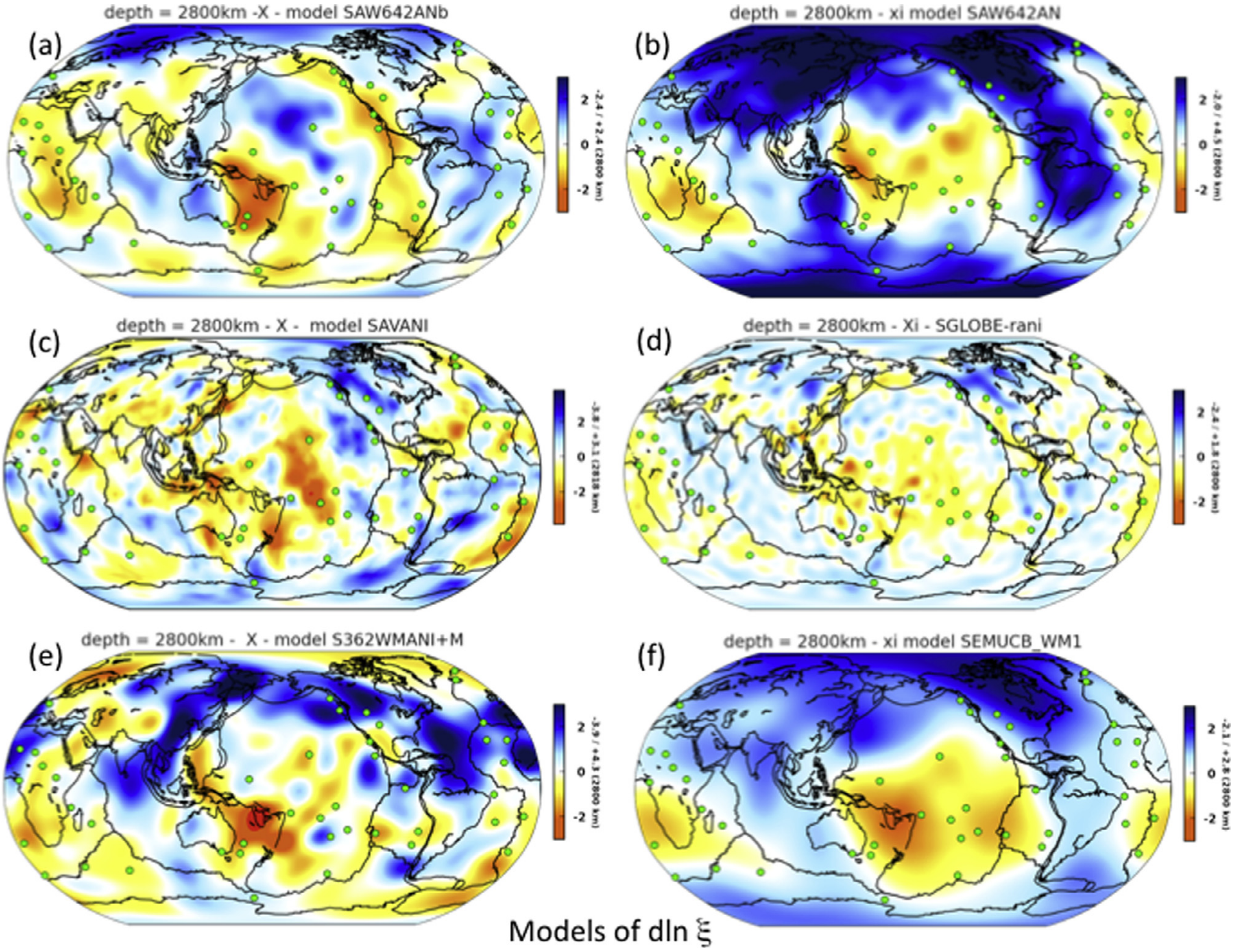

Fig. 8. Comparison of 6 recent models of lateral variations in the radial anisotropy parameter $\xi = (V_{sh}/V_{sv})^2$, plotted in terms of dlnξ referred to isotropy. While the models disagree in detail, common features are $V_{sh} > V_{sv}$ (blue) in the circum Pacific ring (roughly in agreement with local studies), and pronounced $V_{sv} > V_{sh}$ (orange) in the Fiji-Tonga/Indonesia region and under southernmost Africa (except SAVANI). Models plotted are: (a) SAW642ANb (Panning et al., 2010); (b) SAW642AN (Panning and Romanowicz, 2006); (c) SAVANI (Auer et al., 2014); (d) SGLOBE-rani (Chang et al., 2015); (e) S362WANI + M (Moulik and Ekström, 2014); (f) SEMUCB_WM1 (French and Romanowicz, 2014).

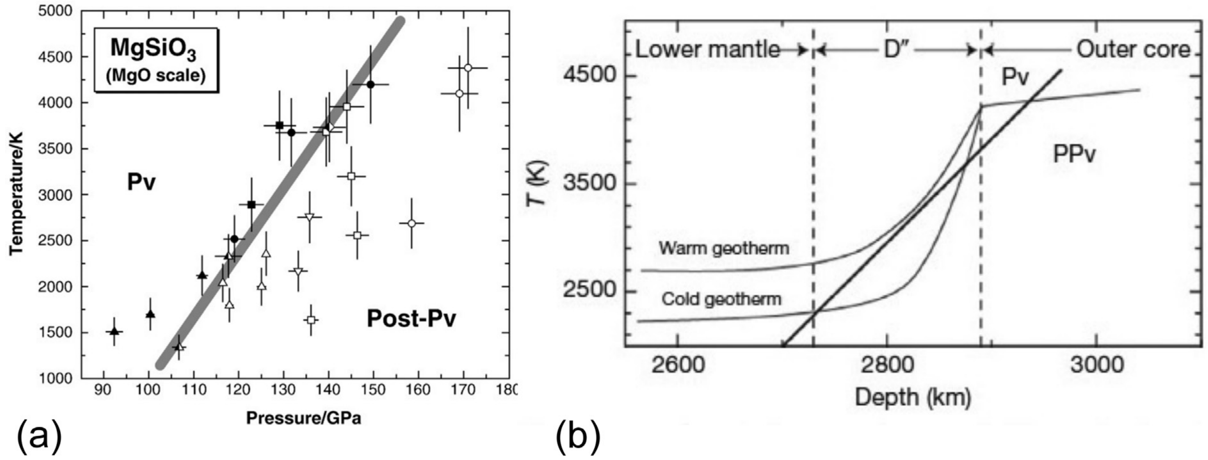

Fig. 9. (a) Experimentally determined PT phase diagram for perovskite/bridgmanite (Pv)-post-perovskite (Murakami et al. 2004). (b) T-Depth phase diagram, plotting the pv-ppv phase boundary and cold and warm geotherms (after Hernlund et al., 2005).

because some produce crystal rotations and thus crystallographic preferred orientation (notably dislocation glide and – to some extent – dynamic recrystallization) while others generate random orientations (such as grain boundary sliding in fine-grained materials and dislocation climb). We will return to these issues in Section 4.8.

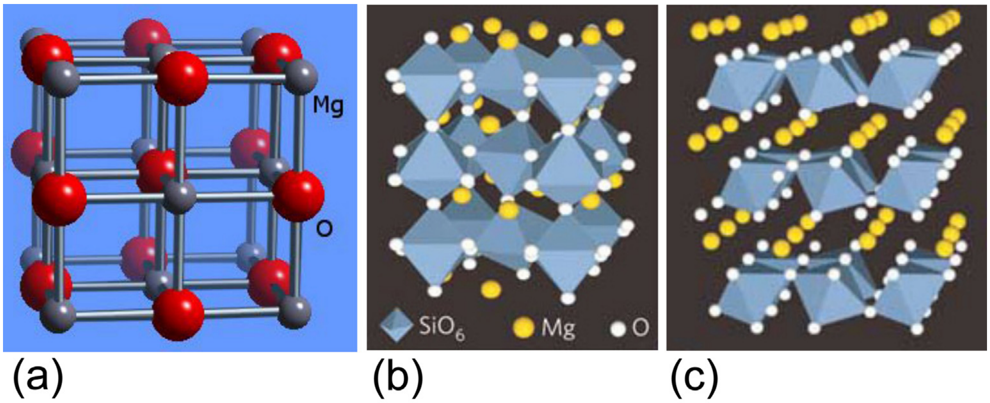

Fig. 10. Crystal structures of (a) periclase, (b) bridgmanite and (c) post-perovskite, the latter two with octahedrally coordinated silicon.

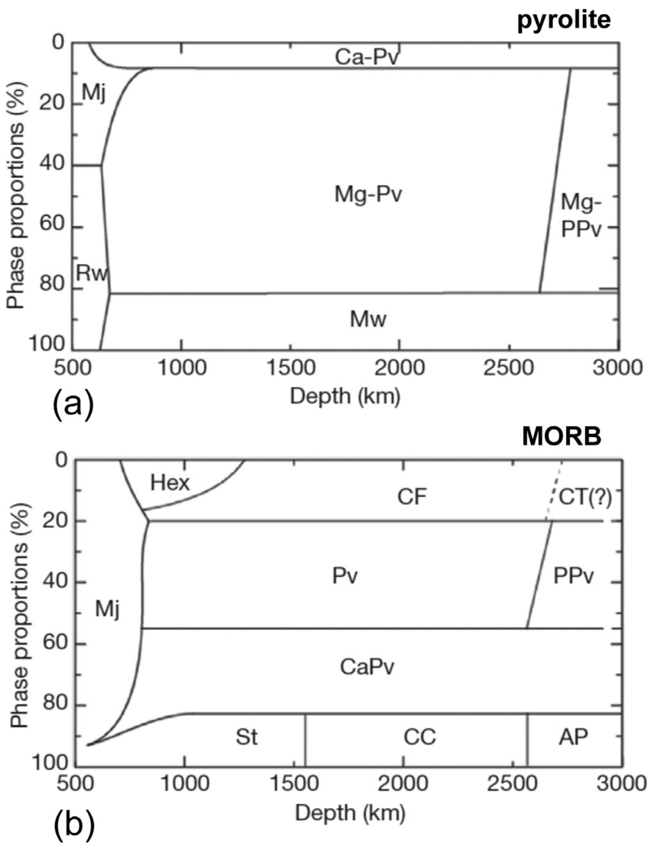

Fig. 11. Lower mantle composition for different models: (a) pyrolite, (b) MORB (from Irifune and Tsuchiya, 2015). Pv perovskite/bridgmanite, Ppv post-perovskite, Mw magnesiowuestite/ferropericlase, Mj majorite, Rw ringwoodite, SiO_2: St stishovite, CC $CaCl_2$ phase, AP α-PbO_2 phase; Al_2O: Hex, CF calcium-ferrite phase, CT calcium-titanate phase.

In a polycrystalline aggregate, stresses are transmitted across grain boundaries, causing heterogeneities, even within grains. This is most realistically approached with finite element methods (e.g. Mika and Dawson, 1999), but these are still extremely demanding and rarely applied. Simpler models have been used in materials science for a long time. The Taylor (1938) theory, developed by the same Taylor who discovered dislocations (1934), assumes homogeneous strain. All grains undergo the same shape change irrespective of orientation. This leaves grain boundaries intact (Fig. 14, left side). The Taylor model is very applicable to cubic metals with many symmetrically related slip systems. Slip on {1 1 1}⟨1 1 0⟩ in fcc metals or cubic periclase has 12 equivalent systems. Another model (Sachs, 1928) assumes stress equilibrium and more favorably oriented grains deform more than others. In the model this causes overlaps and gaps at grain boundaries. In principle, this would be more adequate for low symmetry minerals (such as orthorhombic) but of course overlaps and gaps do not exist. A compromise between homogeneous strain and stress equilibrium is a self-consistent model that treats grains as ellipsoidal inclusions deforming in an anisotropic viscous medium (Fig. 14, center; Molinari et al., 1987). It is most widely applied in the Los Alamos code VPSC (Lebensohn and Tomé, 1993), and it can be used both to understand preferred orientation in high pressure experiments and to predict anisotropy in geodynamic models. In the viscoplastic self-consistent model grains deform without knowledge of their neighborhood. In a finite element model (Fig. 14, right) grains are constrained by the orientation of neighbors. In this sketch it is assumed that each grain has a single orientation. In more sophisticated FEM models there are strain and orientation gradients developing within grains (e.g. Mika and Dawson, 1999).

When crystals are deformed in a polycrystalline medium they undergo systematic rotations (Fig. 12) and the material attains an anisotropic pattern. We need to describe the orientation of a crystal relative to the macroscopic sample. This is efficiently done by relating two orthogonal coordinate systems (sample x, y, z; crystal [1 0 0], [0 1 0], [0 0 1]) by three rotations. Most frequently the so-called Euler angles are used. Φ is the distance from z to [0 0 1], ϕ_1 is the azimuth of [0 0 1] from y (around z); ϕ_2 is the azimuth of [1 0 0] around [0 0 1] (Fig. 15). The 3-dimensional crystal orientation distribution (COD) is conventionally described by a continuous orientation distribution function (ODF). The ODF is required to calculate anisotropic elastic properties of an aggregate from crystal orientations.

For graphical representations of orientation patterns generally 2-dimensional spherical projections of the ODF are used. Depending on the application one can either use the macroscopic sample x, y, z as reference and plot crystal directions (pole figures) or use the crystal as reference and plot sample directions (inverse pole figures). Inverse pole figures are useful if only a single sample direction is of interest, e.g. the compression direction in a compression experiment. The symmetry of pole figures reflects the symmetry of the deformation path. In compression experiments pole figures are axially symmetric. The density of poles on the sphere is contoured and then expressed as continuous pole densities, usually normalized relative to a random distribution and defined as multiples of a random distribution (m.r.d.). 2–5 m.r.d. are moderate CODs, 20–50 m.r.d. very strong CODs. The strongest crystal alignments in rocks that have been observed are muscovite in slates, exceeding 100 m.r.d. Fig. 16a is a {1 1 1} pole figure of rolled copper with roll-

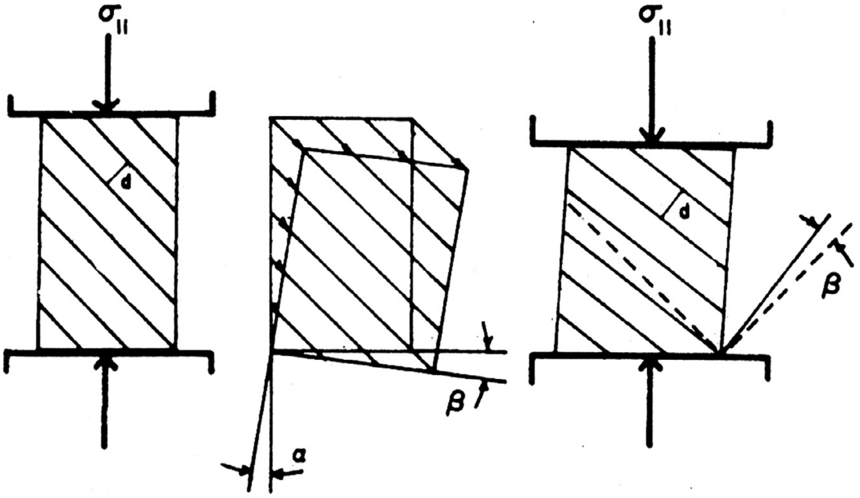

Fig. 12. Under stress imposed by pistons a crystal deforms to a new shape by slip of dislocations on a glide plane. Since pistons remain in contact with the crystal surface, there is an effective rotation β. In a polycrystal neighboring grains act as effective pistons to transmit the stress.

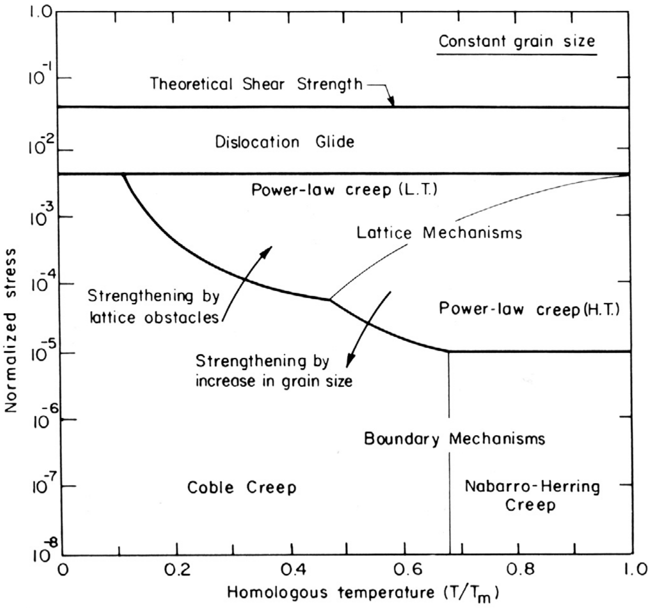

Fig. 13. Stress-temperature deformation mechanism map (Langdon and Mohamed, 1978).

ing R, transverse T and normal N sample directions indicated. Fig. 16b is the corresponding inverse pole figure of the normal direction. Inverse pole figures display the crystal symmetry. Both representations will be used in the following discussion.

3.3. Deformation experiments and rheology

The experiments on plasticity of metals were not applicable to most minerals, because, even at elevated temperatures, their deformation behavior at ambient pressure is generally brittle. One had to wait until high pressure deformation experiments were developed by Griggs (1936) and applied on a wide scale, including olivine (e.g. Raleigh, 1968). Since then sophisticated deformation apparati have been constructed in many laboratories, making it possible to deform rocks at a wide range of pressures and temperatures. They were applied to many minerals and rocks in the crust and upper mantle. Studies on olivine (e.g. Jung and Karato, 2001; Hansen et al., 2012; Jackson and Faul, 2010) documented the complex influence of temperature, pressure, composition (such as water and iron content). The most sophisticated apparatus was developed at the Australian National University (Paterson and Olgaard, 2000). It allows for deformation experiments on relatively large samples (~1 cm) in compression, tension and torsion. Pressures are limited to ~0.3 GPa and the limitation in pressure prevents these instruments to be used for experiments relevant to the lower mantle (20–150 GPa) and inner core (320–360 GPa).

Higher pressure deformation experiments have been reviewed by Weidner and Li (2015). The multi-anvil apparatus called DIA with three pairs of octahedral pistons (Onodera, 1987) has been modified to apply stress by preferentially advancing one piston pair (D-DIA for deformation DIA). The sample can be heated internally. Changes in phase structure, preferred orientation and microstructure can be recorded *in situ* if the D-DIA apparatus is combined with a monochromatic synchrotron X-ray beam for diffraction and imaging (e.g. Wang et al., 2003, 2011). The conventional D-DIA apparatus has been used to 20 GPa and samples are cylinders ~1 mm in diameter (e.g. Kawazoe et al., 2010). A more advanced D-DIA (Kawai-type) reaching >110 GPa with sintered diamond anvils and smaller samples has been introduced at SPring8 in Japan (Yamazaki et al., 2014).

Shear deformation at high pressure can be performed with a rotational Drickamer apparatus (RDA) (e.g. Yamasaki and Karato, 2001). Shear deformation of a bridgmanite-ferropericlase aggregate at 25 GPa and 2100 K has been achieved to large strains (Girard et al., 2016). In such torsion experiments the strain varies greatly as a function of sample radius. The experiment documented that most of the plastic deformation is accommodated by the weaker ferropericlase.

Currently the most accessible method to deform samples at ultrahigh pressures (>500 GPa) is with diamond anvil cells (DAC) where diamonds are used as pistons, compressing a small sample (~30–80 μm in diameter and ~50 μm thick) (e.g. Merkel et al., 2002, Fig. 17). The diamonds are used not only to induce pressure but also to cause compressive deformation (Fig. 17 b, c) and the evolution of preferred orientation can be observed *in situ* if horizontal X-rays transmit the sample in radial diffraction geometry (r-DAC). Strong textures have been observed in ferropericlase (e.g. Merkel et al., 2002; Lin et al., 2009), perovskite/bridgmanite (e.g. Merkel et al., 2003; Wenk et al., 2006; Miyagi and Wenk, 2016; Tsujino et al., 2016) and pPv, the phase likely to be present at the core-mantle boundary (e.g. Merkel et al., 2006, 2007;

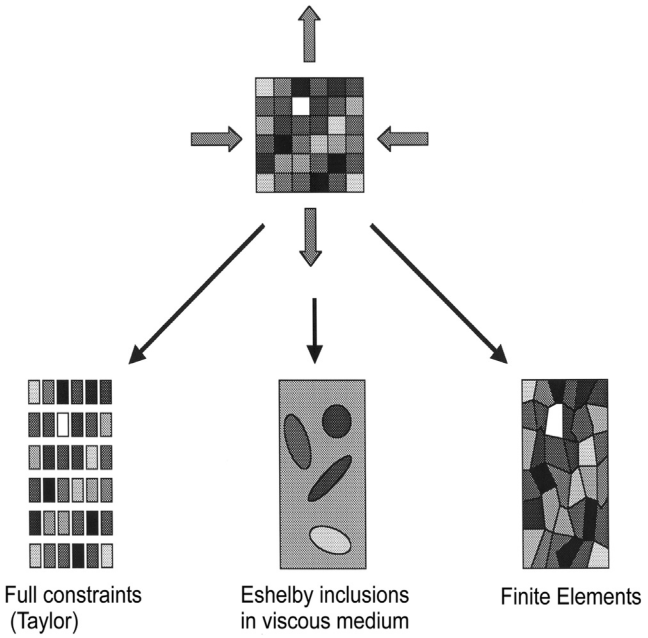

Fig. 14. 2D Sketches of polycrystal plasticity models. Gray shades express orientation. (Left) For the full constraints Taylor model all grains undergo the same deformation, regardless of orientation. (Center) The viscoplastic model VPSC treats grains as inclusions in an anisotropic viscous medium. (Right) In finite element models grains deform differently, depending on the orientation of neighbors.

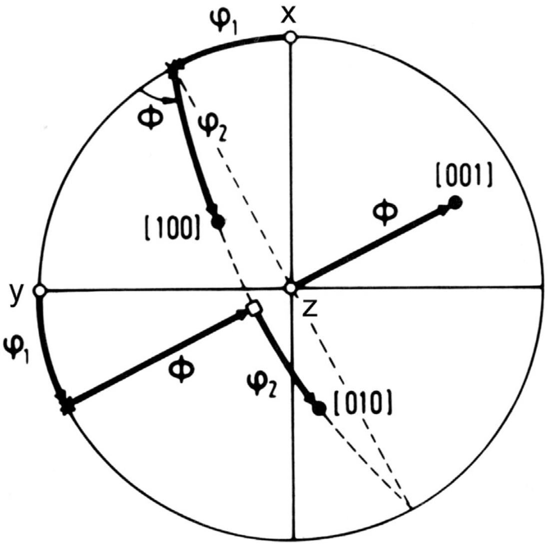

Fig. 15. Definition of crystal orientation relative to sample coordinates with three rotations (Euler angles) ϕ_1, Φ, ϕ_2. Projection based on sample coordinate system x, y, z (pole figure). Crystal coordinate system is defined by axes [100], [010] and [001].

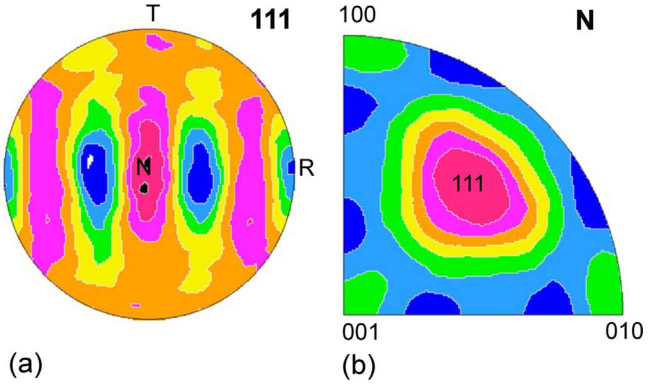

Fig. 16. Comparison of (a) 111 pole figure relative to sample coordinates and (b) N inverse pole figure relative to crystal coordinates for rolled copper. Equal area projection, red colors are high and blue colors are low pole densities. N normal direction, R rolling direction and T transverse direction. Note the equivalent information: In the 111 pole figure a maximum in the N direction, and in the ND inverse pole figure a maximum in 111.

Miyagi et al., 2010, 2011; Wu et al., 2017). Shear deformation can be induced in rotational DACs (e.g. Levitas et al., 2006). This method has been mainly used to induce phase transformations and has not yet been applied to study texture evolution at high pressure.

In addition to pressure and stress, temperature can be induced in DAC experiments by resistive (e.g. Liermann et al. 2009) and laser heating (e.g. Prakapenka et al., 2008; Dubrovinsky et al., 2009), or a combination of the two (Miyagi et al., 2013). Tateno et al. (2015) reached temperatures of 6000 K at >400 GPa on experiments on Fe and Fe-Si, corresponding to conditions of the Earth's inner core. Obviously there are limitations to DAC experiments: samples are extremely small, strain is always compressive and strain rates are difficult to control.

It was surprising to see that silicates and oxides that are brittle at ambient conditions, including olivine, become ductile at pressures of ~10GPa, even at room temperature, and deform by dislocation glide (e.g. Wenk et al., 2004). The diffraction image of $MgSiO_3$ post-perovskite at 150 GPa (Fig. 18a) is "unrolled" and the compression direction is indicated by arrows (large 2θ, small d, Q=1/d) (Fig. 18b). The elastic lattice distortion (wave-like pattern with azimuth) is related to applied stress and elastic properties. The intensity variations with azimuth are indicative of preferred orientation. For example there is a strong maximum for 004 (fourth order diffraction on the lattice plane 001) in the compression direction. This image illustrates why radial diffraction geometry has to be used to display CPO as function of angle to the compression direction. In axial geometry (X-rays parallel to the diamond axis) Debye-rings have uniform intensity since all diffracting lattice planes have the same angle to the compression direction.

A qualitative interpretation of a diffraction image is illustrated in Fig. 19 for an experiment with $MgGeO_3$ post-perovskite (Miyagi et al., 2011) and used to construct an inverse pole figure of the compression direction (arrow). $MgGeO_3$ is an analog of $MgSiO_3$ but transforms to pPv at lower pressure. There is a maximum for 002 and a minimum for 020 in the compression direction which can be plotted in the inverse pole figure (Fig. 19, right side). The quantitative deconvolution of diffraction images is not trivial and most often an iterative Rietveld method is applied (e.g. Lutterotti et al., 2014; Wenk et al., 2014). The high pressure synchrotron X-ray diffraction deformation images provide quantitative information about phases, crystal structures, density, stress, elastic properties and preferred orientation.

Fig. 20a-c shows experimental inverse pole figures of $MgSiO_3$ pPv, documenting increasing texture development with pressure-stress–strain, with a maximum at (001). From the orientation pattern, active slip systems can be derived by comparing experimental inverse pole figures with results from polycrystal plasticity calculations that assume certain combinations of slip systems (Fig. 20d). Based on the good agreement it can be concluded that pPv deformed in the experiment by dominant (001)[100] slip (Miyagi et al., 2010).

With similar experiments it was suggested that $MgSiO_3$ bridgmanite deforms dominantly by slip on (001) planes in [100], [010], and ⟨1 1 0⟩ directions (e.g. Miyagi and Wenk, 2016) but sim-

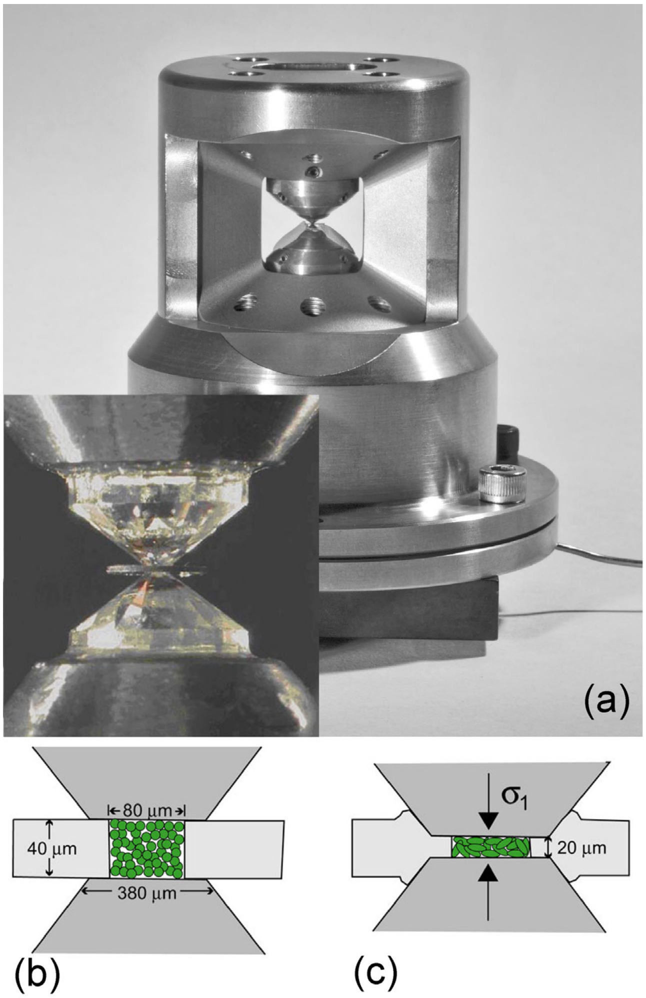

Fig. 17. Diamond anvil cell for radial diffraction experiments. The X-ray beam is horizontal. (a) illustrates the cell and the insert is an enlargement with diamonds and gasket to contain the sample. (b, c) illustrate that diamonds not only apply pressure but also compressive stress that deforms the sample and produces CPO.

ple shear experiments in a D-DIA apparatus indicate $(100)[001]$ slip (Tsujino et al., 2016). Ferropericlase likely deforms by $\{110\}\langle 1\,{-}1\,0\rangle$ slip (e.g. Stretton et al., 2001; Merkel et al., 2002; Lin et al., 2009) at high pressure conditions. For Ca-perovskite dominant $\{110\}\langle 1\,{-}1\,0\rangle$ slip was proposed (Miyagi et al., 2006, 2009).

So far most DAC high-pressure deformation experiments extracted COD information from intensity variations along Debye rings (e.g. Fig. 18). A new method called multigrain is still under development. It obtains orientation information from individual grain diffractions (e.g. Barton and Bernier, 2012; Rosa et al., 2015; Langrand et al., 2017) and is especially applicable to coarser aggregates. Nisr et al. (2012) used information about dislocations from distortion of single crystal diffraction patterns of the post-perovskite analog $MgGeO_3$ and suggested dominant slip on $\{110\}$ and (001) planes.

It should be mentioned that information from such high pressure experiments is by no means unambiguous. Obviously deformation conditions in experiments and simulations differ considerably from those in the deep Earth, just to mention temperature, grain size, strain rate, interaction of dislocations and interaction between grains. Furthermore, not all CPO patterns that are observed are due to deformation but could be inherited from orientation patterns of precursor phases such as for pPv from perovskite (Dobson et al., 2013) or enstatite (Merkel et al., 2006, 2007; Miyagi et al., 2011). Also, slip systems may not be the same for pPv phases of different compositions such as $MgGeO_3$, $CaIrO_3$, $NaMgF_3$, or Mn_2O_3.

A different approach has become very important: computation of Peierl's stresses and lattice friction for dislocation systems based on bonding characteristics. It was originally developed for metals (e.g. Kubin et al., 1992; Devincre and Kubin, 1997) and has more recently been applied to minerals in the mantle where it allows to predict slip system activities for a wide range of temperature–pressure–strain rate conditions (e.g. Carrez et al., 2007; Mainprice et al., 2008; Cordier et al., 2012). Amodeo et al. (2012, 2014, 2016) propose a switch from $\{110\}\langle 0\,{-}1\,0\rangle$ slip to $\{100\}\langle 0\,1\,1\rangle$ slip in periclase with pressure. Kraych et al. (2016) suggest $(010)[100]$ slip in bridgmanite at high pressure. According to these calculations, the strength of bridgmanite increases greatly with pressure and at 60 GPa bridgmanite appears 20 times stronger than periclase. The critical resolved shear stress decreases about 20% from strain rates of $10^{-5}\,s^{-1}$ (which corresponds to

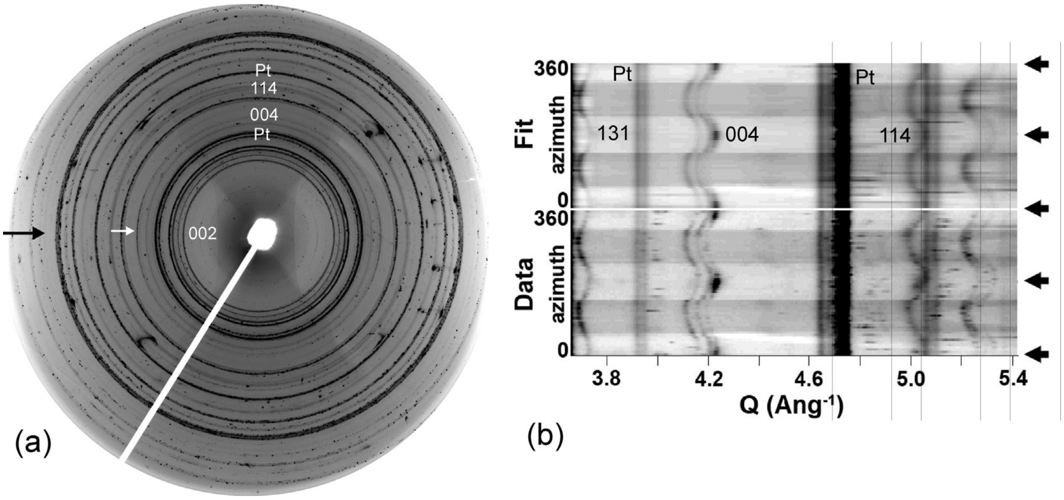

Fig. 18. (a) Diffraction image of $MgSiO_3$ post-perovskite at 150 GPa (b) Unrolled diffraction image as function of Q (Q = 1/d). Intensity variations with azimuth illustrate CPO, changes in Q are due to elastic distortion of the crystal lattice under compression. Bottom experimental data, above fit of the data with the Rietveld method to extract quantitative information such as inverse pole figures.

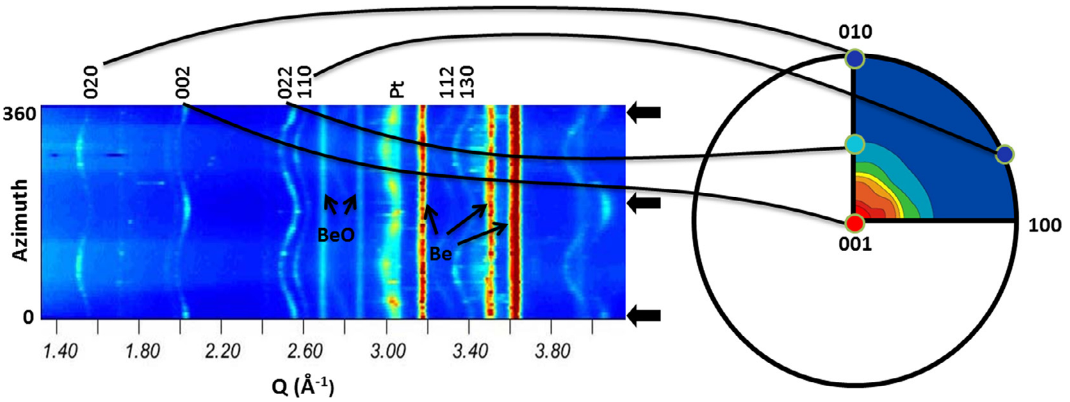

Fig. 19. Explanation of the relationship between DAC diffraction image and inverse pole figure. Left: Unrolled diffraction image of $MgGeO_3$ post-perovskite. Some diffraction lines are labeled. The sinusoidal variations are due to imposed stress. High stress (high Q, low d) is indicated by arrows. On the right side is a conceptual construction of the inverse pole figure of the compression axis based on relative diffraction intensities (Miyagi et al. 2011).

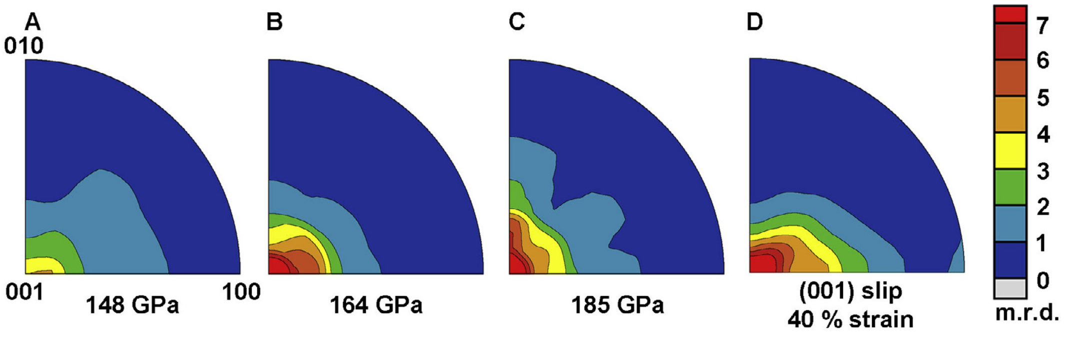

Fig. 20. Inverse pole figures for $MgSiO_3$ post-perovskite. (A–C) experiments (D) Plasticity model with dominant (001) slip, equal area projection (Miyagi et al. 2010).

experimental values) to 10^{-14} s^{-1}, corresponding to likely values at deep mantle conditions (Fig. 21a). The opposite is the case for pPv which appears much weaker than periclase at high pressure, high temperature and slow strain rates (Fig. 21b, Goryaeva et al., 2015, 2016). Also, the predicted weakest calculated slip system for post-perovskite at deep mantle conditions is (010)[100], corresponding to the layered crystal structure (Fig. 21c) but different from that observed in DAC experiments (Miyagi et al., 2010; Wu et al. 2017).

It should be mentioned that a single slip system is not sufficient to deform a polycrystal. In the case of the Taylor model, at least 5 systems have to be active to produce an arbitrary strain (Mises, 1928). This is relaxed for the self-consistent model but also here several slip systems are active. The choice of activity depends on the crystal orientation relative to the applied stress (Schmid factor). TEM investigations confirm this, though some slip systems usually dominate and the literature refers to the “dominant” slip system. Some dominant slip systems for deep Earth minerals are summarized in Table 2.

3.4. Elastic properties

Elastic properties of crystals at conditions pertaining to the lower mantle are critical to link microstructural properties of the rock with seismic observations. The most straightforward experimental method that has been applied to many lower mantle minerals is Brillouin scattering (see review by Speziale et al., 2014) and energy-dispersive X-ray diffraction (e.g. for calcium silicate perovskite, Shieh et al., 2004). A different approach is with first principles calculations at high pressure and temperature (for some applications to bridgmanite, $CaSiO_3$ perovskite and pPv see e.g. Zhang et al., 2013; Wentzcovitch et al., 2005; Kawai and Tsuchiya, 2015). First principles results look fairly consistent for minerals at lower mantle conditions, but as we will see in Section 6.2, predictions for iron at inner core conditions are still ambiguous. Furthermore, the actual composition of the minerals, particularly the iron content can be significant (e.g. Koci et al. 2007). Values of stiffness coefficients and P-wave anisotropy (An % = $200(P_{max} - P_{min})/(P_{max} + P_{min})$ for some low mantle minerals at lowermost mantle conditions are listed in Table 3. Fig. 22 gives corresponding S velocities of single crystals with black lines corresponding to the orientation of the fast S-wave polarization. As can be seen in Table 1 periclase and pPv have the highest P-wave anisotropy and Ca-perovskite is least anisotropic. The S-wave anisotropy is considerably higher for pPv and periclase than for bridgmanite and particularly $CaSiO_3$ perovskite.

To obtain elastic properties of aggregates, one has to average over all orientations and corresponding elastic tensors, taking phase fractions into account. Simple averages are upper bound (Voigt, 1887) and lower bound (Reuss, 1929). Generally an intermediate arithmetic mean (Hill, 1952) or a geometric mean (Matthies and Humbert, 1995) are preferred. All these models do not take grain shape into account, which is not very significant for crystalline phases but becomes important for systems with platy minerals such as graphite or sheet-silicate containing rocks and aggregates with flat oriented pores. For such cases, a self-consistent (Matthies, 2012; Vasin et al., 2013) or differential effective medium approach (e.g. Hornby et al. 1994) should be considered. It is probably not important for the lower mantle.

Note that S-waves passing through anisotropic media have arbitrary polarization directions in the plane perpendicular to the direction of propagation, as is best displayed for the fast direction of single crystals in Fig. 22 but applies also to aggregations of ori-

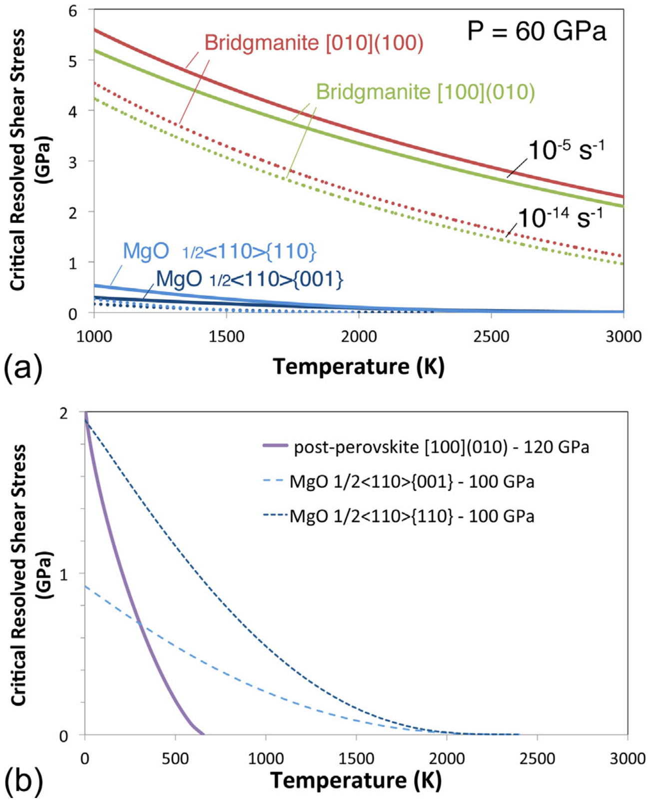

Fig. 21. Critical resolved shear stress CRSS for dislocation glide activities as function of temperature of (a) bridgmanite at 60 GPa (from Kraych et al. 2016) and MgO (from Amodeo et al. 2016) at strain rates 10^{-5} s^{-1} and 10^{-14} s^{-1}. (b) post-perovskite at 120 GPa at strain rate 10^{-16} s^{-1} (from Goryaeva et al., 2016) compared with MgO (from Amodeo et al. 2012). Courtesy of P. Cordier.

ented crystals. Seismologists generally consider the projection of that polarization direction onto horizontal and vertical axes. This is convenient, because differences in arrival times and waveforms in this representation can be expressed in terms of apparent vertical transverse isotropy (VTI), which, because of limited azimuthal sampling, is often the only anisotropic constraint that can be obtained.

4. Linking seismology and mineral physics through predictions of anisotropy in geodynamic models

4.1. Isotropic geodynamic models for upper mantle convection

Ever since the concept of plate tectonics became accepted in the 1960s, convective movements in the Earth's mantle have been proposed such as upwelling along oceanic ridges (e.g. Hess, 1964; Cann, 1968, Fig 1b). The first quantitative models based on hydrodynamics emerged in the eighties (e.g. Hager and O'Connell, 1981). Geodynamic models have been mainly applied to the upper mantle and we will not discuss them here in detail (see e.g. review by Long and Becker, 2010).

Many convection models have been developed to understand the evolution of the deep Earth. Calculations generally assume a viscous fluid and use non-dimensional equations for the conservation of mass, momentum, and energy, applying the Boussineq approximation. Critical parameters are Rayleigh number, viscosity, boundary temperatures. In order to evaluate the strain evolution during the convection process, tracers are introduced that record the velocity gradient tensor at each time step along the path of the tracer. If the deformation mechanisms are known (e.g. dislocation glide) polycrystal plasticity calculations can be used to calculate the evolution of crystal preferred orientation based on the strain recorded by tracers.

Most geodynamic models assume a viscous isotropic medium, with a smoothly varying viscosity structure, and the microstructural processes leading to preferred orientation are introduced post-mortem. Considering an anisotropic medium that constantly changes its properties greatly increases the complexity of geodynamic calculations. However, there are models in metallurgy, such as extrusion of an aggregate, that illustrate the importance of an anisotropic material behavior (e.g. Beyerlein et al., 2003).

4.2. Review of upper mantle anisotropic models

We will start the discussion of anisotropic convection by returning to a simple 2D model (Dawson and Wenk, 2000) that was originally issued as an educational video by AGU (1999) and can now be downloaded in digital form (http://eps.berkeley.edu/~wenk/TexturePage/Mantle-Video.htm). At high Rayleigh number (low viscosity) heat transfer occurs by convection rather than conduction, corresponding to conditions in the Earth's mantle. Convection is driven by temperature gradients. As aggregates move along streamlines, the orientation of grains is constantly updated and the local texture affects the next deformation step, which introduces considerable heterogeneities. It was surprising to find locally heterogeneous CPO patterns in the 2D convection cell representing the upper mantle, shown as [100] pole figures of olivine after 100 m.y. (Fig. 23). Some regions have strong and others very weak patterns, that can be attributed to heterogeneous deformation due to CPO development and result in "anisotropic" viscosity.

Some complexities of different plasticity models for a simple case of upwelling have been investigated by Blackman et al. (1996, 2002) and Castelnau et al. (2009). If a lower bound behavior is assumed (Sachs, 1928), there is very strong CPO development. For self-consistent models (Lebensohn and Tomé, 1993) rotations are reduced. If dislocation glide is combined with dynamic recrystallization, both grain growth and grain growth combined with nucleation, resulting orientation patterns can be very different. Recrystallization is likely in the deep Earth, with high temperature and large strains, where grain boundary migration is likely to occur. We will return to the issue of recrystallization in Section 4.8.

Table 2
Proposed dominant slip systems in deep Earth minerals.

Ferropericlase	Lower P {110}1 −10	Merkel et al. (2002) and Lin et al. (2009)
	High PT also {100}011	Amodeo et al. (2016)
Bridgmanite	Low P (001)[100], [010], 110	Miyagi and Wenk, 2016
	High P (100)[001]	Tsujino et al. (2016)
	(010)[100]	Kraych et al. (2016)
pPv	(001)[100]	Miyagi et al. (2010) and Wu et al. (2017)
	(010)[100]	Goryaeva et al. (2016)
Ca-perovskite	{110}1 −10	Miyagi et al. (2009) and Ferré et al. (2009)
ε-iron	(0001)11 −20, subordinate {10 −10}	Merkel et al. (2004) and Miyagi et al. (2008)

Table 3
Density (g/cm^3), elastic stiffness (GPa) and P-wave anisotropy (An%) of periclase, bridgmanite, post-perovskite and Ca-perovskite at conditions of the lowermost mantle (3000 K, 125 GPa).

	Periclase	Bridgmanite	pPv	Ca-perovskite
	Karki et al. (2000)	Wentzcovitch et al. (2004)	Stackhouse et al. (2005)	Kawai and Tscuchiya (2015)
ρ	5.07	5.25	5.35	5.6
C_{11}	1154.0	860.0	1220.0	970
C_{12}	265.5	535.5	474.0	505
C_{13}	265.5	437.0	359.0	505
C_{22}	1154.0	1067.5	899.0	970
C_{23}	265.5	467.5	493.0	505
C_{33}	1154.0	1053.0	1176.0	970
C_{44}	198.0	294.0	273.0	305
C_{55}	198.0	249.5	245.0	305
C_{66}	198.0	284.5	376.0	305
An%	16.7	11.0	15.2	4.7

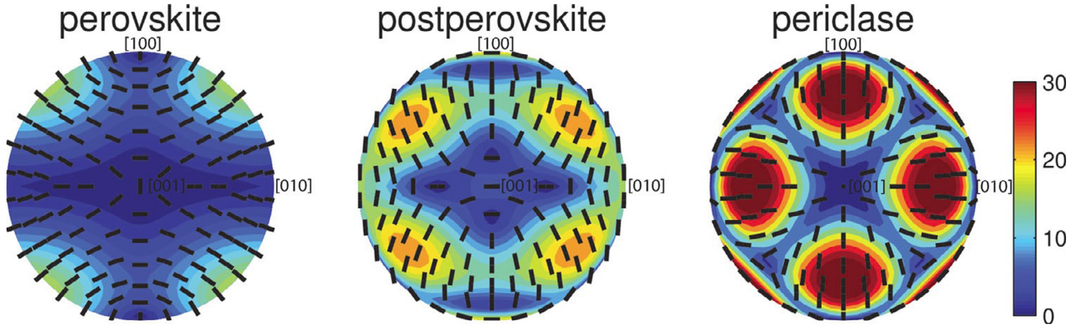

Fig. 22. Spherical representation of shear-wave splitting (in m/s) of main minerals at lowermost mantle conditions and corresponding to elastic properties in Table 1. Values are in m/s; black lines illustrate polarization of the fast S-wave.

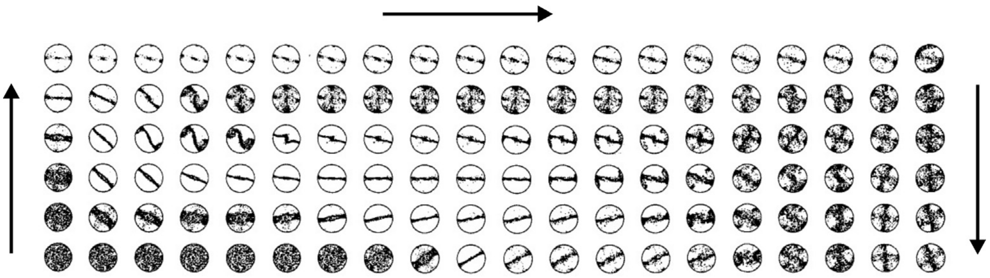

Fig. 23. (0 0 1) pole figures of olivine for a finite element model of homogeneous upper mantle convection that takes anisotropy development into account. Upwelling on left, subduction on the right (Dawson and Wenk, 2000).

4.3. Anisotropic models for the lowermost mantle

As explained earlier, seismic imaging of the D″ zone has revealed an anisotropic velocity structure, particularly expressed in fast S-wave velocities for polarization parallel to the core-mantle boundary, in regions that are thought to correspond to slab graveyards (Fig. 8). This seismic anisotropy depends on the elastic properties of the rocks. Elastic properties are due to the mineral phases that are present, the orientation of crystals and the elastic properties of single crystals at D″ conditions. If we know the deformation mechanisms of crystals at conditions of the lower mantle (from high pressure/temperature deformation experiments or bonding calculations), we can predict the alignment of crystals in an aggregate that has undergone a strain path recorded by tracers in a geodynamic model.

An isotropic viscous medium approach was used by McNamara et al. (2002) and then extended to include texture development by Wenk et al. (2006) and Wenk et al. (2011) in 2D, and Cottaar et al. (2014) in 3D, to predict patterns of seismic anisotropy in and around slabs as they impinge on the core-mantle boundary.

In another approach, the flow field is derived from an instantaneous flow calculation based on the consideration of an existing 3D mantle global tomographic model, a 1D mantle viscosity model, as well as constraints from geodynamic observables such as the gravity field and surface plate motions (e.g. Simmons et al., 2009). This was used by Walker et al. (2011) and Nowacki et al. (2013) to predict global anisotropy patterns. The advantage of this model is that it applies to the whole Earth, but it may be biased by the tomographic seismic structure, and assumptions on the conversion of seismic velocities to density to establish the flow field.

In both approaches, particle paths are tracked by tracers, allowing the computation of the strain field. Texture development is then modelled in polycrystalline aggregates, starting from a large sample of randomly oriented grains, and applying polycrystal plasticity theory (Section 3.2), followed by computation of the elastic tensor of the aggregate, by averaging over crystal orientations and corresponding single crystal elastic properties.

4.4. Isotropic viscosity medium approach for lower mantle anisotropy

This type of model investigates the characteristics of a subductiong cold slab descending through the lower mantle to the core-mantle boundary. The model is isochemical and isotropic viscosity is assumed. The calculations solve non-dimensional equations for the conservation of mass, momentum and energy, using the Boussinesq approximation (McNamara et al., 2003). The strain evolution is evaluated by inserting tracers into the isotropic convective medium. This strain is then used to calculate development of preferred orientation using the viscoplastic self-consistent method (Lebensohn and Tomé, 1993), which was introduced in Section 3.2 for evaluating slip systems in high pressure deformation experiments.

We will explain the general procedure for a 2D model of a subducting slab into the D'' zone (Wenk et al., 2011). Fig. 24 (top) is a snapshot of a section of the upper mantle with downwelling cold slabs (blue) und upwelling hot plumes (red). Below (Fig. 24 bottom) is an enlarged section of D'', extending 300 km above the core-mantle boundary. It indicates the path of some streamlines. We are following the lowest tracer 189. Post-perovskite and ferropericlase are likely the main components in the cooler parts of the enigmatic D'' zone and texture calculations were done with such a 2-phase system. In addition significant amounts of cubic $CaSiO_3$ perovskite may be present but this was not considered in this model because of relatively low anisotropy.

Plasticity calculations were performed by assuming different combinations of dominant slip systems for pPv, since there is some ambiguity (Section 3.2 and Table 2), (100), (010), (001) (e.g. Merkel et al., 2004, 2007; Miyagi et al., 2010, 2011; Wu et al. 2017; Goryaeva et al., 2015, 2016). They are shown in Fig. 25 for dominant (001)[100] slip for pPv and dominant $\{110\}\langle -1\,1\,0\rangle$ slip for periclase (MgO) (e.g. Merkel et al. 2002; Miyajima et al. 2009) at three step increments. There is moderate CPO at 1200 steps but it becomes very strong at 3600 steps. For periclase, there is a significant rotation of the pattern due to simple shear, similar to what was observed in halite with the same crystal structure (Wenk et al., 2009). The simple shear rotation is less pronounced for orthorhombic pPv than for cubic periclase.

Below the pole figures are corresponding maps of P-velocities, again expressing significant rotations for periclase. Post-perovskite shows very low P-velocities parallel to the core-mantle boundary. For two-phase materials the combination may add or reduce overall anisotropy. It should be mentioned that plasticity models assume deformation by dislocation slip. At deep mantle conditions other mechanisms are likely active that do not contribute crystal rotations, such as dislocation climb, grain boundary sliding and to some extent dynamic recrystallization. We will return to some of these issues in Section 4.5. For this calculation, it was assumed that only half of the strain is accommodated by dislocation glide.

Following this procedure for many streamlines, we can map anisotropic velocity patterns over the whole region of the geodynamic model. Fig. 26 shows five simulations, one for ferropericlase and perovskite, and three for post-perovskite assuming different dominant slip systems. Only the pattern for dominant (001) dislocation glide of post-perovskite compares well with seismic observations of fast SH waves in regions of faster than average isotropic Vs (e.g. Fig. 3). The *anti*-correlation of anisotropy in S and P is consistent with a seismic study of the average profile with depth of VTI parameters constrained by normal mode data (Beghein et al., 2006). Perovskite was also considered, but did not match the seismic observations. One additional argument in favor of (001) slip, is the strong splitting and prediction of a tilted fast axis. This is also more compatible, in both direction and strength, with the observations of splitting in S_{diff} at the edge of the African LLSVP (Cottaar and Romanowicz, 2013).

This is an interesting example linking microscopic and macroscopic observations. Deformation mechanisms at the crystal scale (dislocations), derived from laboratory experiments, predict deformation mechanisms and are then applied to Earth processes over large volumes and long time-scales. Comparing the geodynamic results with seismic observations in this case seems to confirm the assumptions about microscopic processes, i.e. the type of dislocations that are active. However, the interpretation relies heavily on the very tentative seismic observation of *anti*-correlation of S and P anisotropy in the deep mantle.

4.5. Flow calculation based on a global tomographic model

This type of flow model is based on the joint inversion of global S-wave travel times, the global gravity field, dynamic surface topography, tectonic plate motions and the excess ellipticity of the core-mantle boundary (Walker et al., 2011). A theory of viscous flow in a compressible, self-gravitating spherical mantle is used to calculate the mantle convective flow predicted on the basis of the tomographically-inferred 3D density anomalies (Mitrovica and Forte, 2004). Fig. 27 shows a map of the horizontal flow vectors (arrows) and radial components of flow velocity (color, blue negative, red positive) illustrating upwelling in the Pacific and in South Africa, for one model. From the 3D mantle flow field polycrystal plasticity calculations, similar to the model discussed in Section 4.3, are used to calculate orientation patterns and corresponding anisotropic elastic properties.

In tomographic models of radial anisotropy in P (Boschi and Dziewonski, 2000) and instantaneous flow calculations, global maps of VTI inferred from different pPv models are compared with

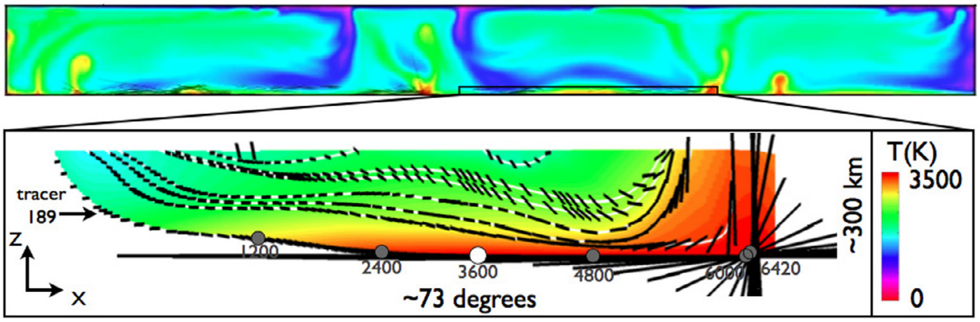

Fig. 24. 2D convection model illustrating subduction of a cold slab (blue) into the lowermost mantle. The insert illustrates some tracers and temperatures in the D'' zone (reproduced from Wenk et al. 2011).

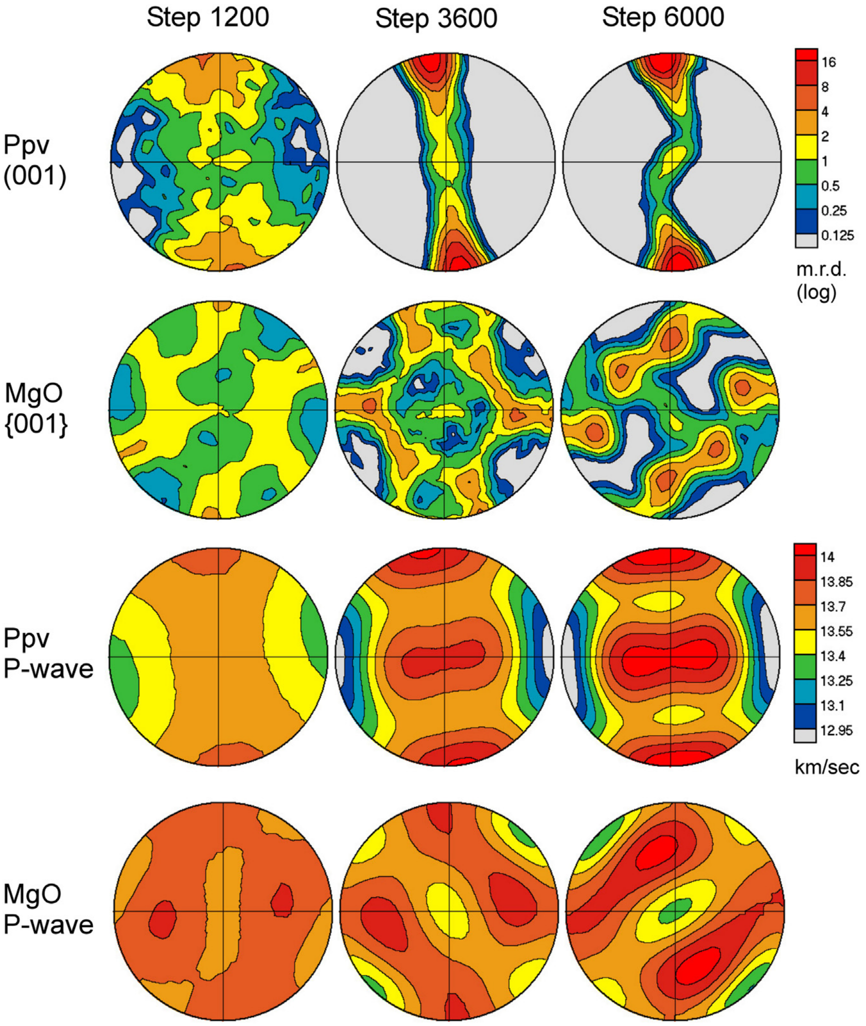

Fig. 25. (001) Pole figures and P-wave velocities for three positions along tracer 189 marked on Fig. Equal area projection. Core-mantle boundary is horizontal.

global seismic VTI models of D″ (Walker et al., 2011). They suggest a preference for slip of dislocations on (010) or (100) and {110} rather than on (001). However, this preference is based on the calculation of correlations that are dominated by regions within the LLSVPs, where, in fact, pPv might not be present, since the LLSVPs are very likely hotter than average regions, and the pPv-bridgmanite transition may occur at pressures corresponding to the core (Fig. 9b). The correlation is dominated by the centers of the Pacific and African LLSVP, where actually one might not expect pPv to be present (Fig. 9b). Clearly, further constraints on P anisotropy in the deep mantle are necessary to better discriminate among possible pPv slip systems.

Whereas Walker et al. (2011) restricted their analysis to the VTI portion of their predicted anisotropic structure, in a follow-up study, Nowacki et al. (2013) extended this approach to allow a most general form of anisotropy, albeit focused on three regions of paleo-subduction, where differential S-ScS shear wave splitting measurements indicate the presence of azimuthal anisotropy in

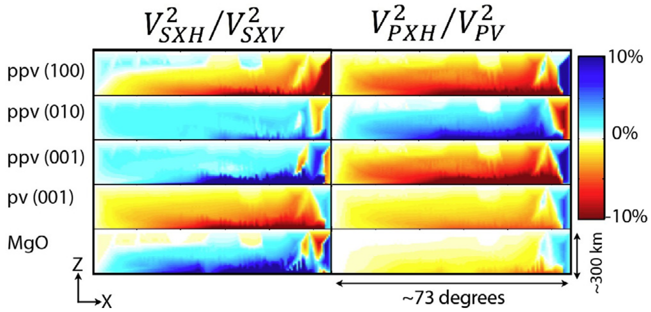

Fig. 26. D″ zone with plots of squared ratios of horizontally and vertically polarized S waves (left side) and horizontal and vertical P-waves for different phases (ppv: post-perovskite, pv perovskite and MgO) and different dominant slip systems (Wenk et al. 2011).

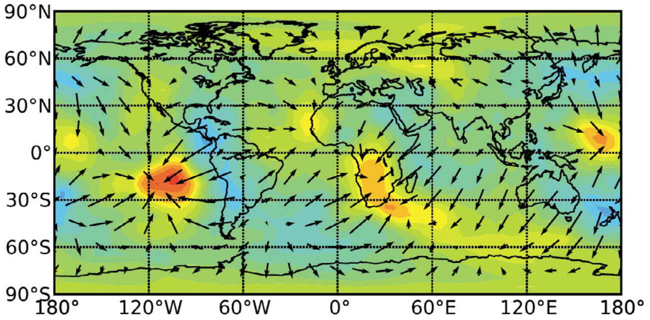

Fig. 27. Tomographic inversion model for mantle flow. Map showing the radial (color, red positive, blue negative) and horizontal flow (arrows) 150 km above the CMB (from Walker et al. 2011).

D″. Testing, as previously, the predictions of anisotropy from the same flow models as in Walker et al. (2011), they confirmed that the (010) slip system of pPv provided the best fit to the seismic data. Still, only the fast axis directions were tested, disregarding the amplitude of splitting, arguing that the latter may be unrealistically strong in plasticity calculations, while imposing any scaling would be arbitrary.

We note that Ford and Long (2015) have independently tested the seismic anisotropy predictions of the Walker et al. (2011) flow models on a set of measurements of shear wave splitting at the eastern edge of the African LLSVP. They concluded that none of the flow models and pPv slip system combinations provided satisfactory predictions of their dataset, although when they relax constraints on the fast axis orientations, the (010) slip model is favored.

4.6. Compositional heterogeneities

Neither the 2D and 3D convection models nor the instantaneous flow model constrained by tomography, include the presence of thermo-chemical piles, as have been hypothesized to explain LLSVPs. The presence of such piles could significantly modify the flow patterns, and focus deformation at the border of the piles, which seems to be observed in some local shear wave splitting studies (e.g. Fig. 4). Also, it appears that the lowermost mantle may be compositionally considerably heterogeneous (e.g. White, 2015). Subduction of lithospheric slabs is a major contribution to heterogeneity, including in the D″ zone (van den Berg et al., 2010, c.f. Fig. 11a and b). Additional phases are likely present, among them cubic $CaSiO_3$ perovskite, silica and perhaps metallic iron (e.g. Shi et al., 2013) (see Fig. 11). Upwelling plumes display chemical heterogeneity and characteristic isotope signatures were documented at hotspots such as Hawaii (Weis et al., 2011; Nobre Silva et al., 2013; Li, Y. et al., 2014), but this does not explain the prevalent seismic anisotropy in the D″ zone, expressed in S-wave splitting patterns with SH>SV (e.g. Table 1, Fig. 3), and for this, crystal alignment during subduction is the most obvious explanation at present (e.g. Cottaar et al., 2014).

4.7. Viscosity changes

There are some complications that have not been taken into account in any of these models. Changes in viscosity do occur, e.g. during phase transformations, with strong increases in the transition zone between the upper and lower mantle (410–660 km). The viscosity is assumed to be low in the upper mantle (radial viscosity of reference model $\sim 0.1 \cdot 10^{21}$ Pa s, Becker, 2006), increases in the transition zone ($\sim 1 \cdot 10^{21}$ Pa s) and then again as minerals transform to denser lower mantle phases ($\sim 50 \cdot 10^{21}$ Pa s). There is considerable complexity as some slabs descend into the lower mantle (e.g. Conrad and Lithgow-Bertelloni, 2004).

Recently seismic heterogeneities were attributed to higher viscosities in the mid-mantle region (∼1000 km), leading to a stagnation of subducting slabs (Rudolph et al., 2015) and this could be due to composition (e.g. Bolfan-Casanova et al., 2003 suggested that the solubility of water decreases), iron fractionation and iron spin transitions (e.g. Lin et al., 2012; Vilella et al., 2015), or changes in mechanical properties with pressure of ferropericlase (e.g. Marquardt and Miyagi, 2015) and post-perovskite (Catalli et al., 2009). First principle calculations of Kraych et al. (2016) suggest a strong strength increase for bridgmanite with pressure (Fig. 21a) and a dramatic decrease for post-perovskite (Goryaeva et al., 2016, Fig. 21b). The geodynamic models described here do not take changes in viscosity into account nor do they consider anisotropic viscosity (e.g. Christensen, 1987).

4.8. Active deformation mechanisms

The models described in this section attribute anisotropy to plastic deformation of crystals by dislocation glide that induces rotations and resulting preferred orientation. In Section 3.2 we discussed deformation mechanisms, and clearly at lower mantle conditions other mechanisms are likely active. The deformation mechanism map (Fig. 13) suggests a creep regime with a combination of dislocation glide and diffusional dislocation climb (e.g. Ammann et al., 2010). Also, grain boundary mechanisms may be active at low stress (e.g. Chen and Argon, 1979), with grain boundary sliding, grain-size reduction but there are no experimental data for lower mantle conditions (e.g. Sun et al., 2016 describe disclinations in olivine). Recent bonding calculations suggest that dislocation climb may dominate in olivine (Boioli et al., 2015) and particularly in bridgmanite (Boioli et al., 2017). Since only glide generates CPO, this may explain why most of the lower mantle appears isotropic. To account for these other mechanisms, in some geodynamic convection models only half of the strain was attributed to glide but this limit is arbitrary.

Many deformation mechanism maps have been introduced for geological systems, with emphasis on the upper mantle and the influences of temperature, pressure, stress and strain rate (e.g. Hansen et al., 2011, 2012; Kohlstedt and Goetze, 1974; Linckens et al., 2011). Extrapolating results to the lower mantle is more speculative, but with new models such as Boioli et al. (2017), Goryaeva et al. (2016) and Kraych et al. (2016), this domain may come within reach.

Another mechanism that is likely active in the deep mantle is dynamic recrystallization. It has been approached with thermodynamic theory of grain growth under stress (e.g. Kamb, 1961; Paterson, 1973; Green, 1980; Shimizu, 1999, 2008; Rozel et al., 2011). While recrystallization can result in grain growth, it more often produces grain size reduction, which has an effect on the rheology (e.g. De Bresser et al., 2001). But evidence from materials science suggests that in deformed aggregates recrystallization is often controlled by crystal defects. Grains with high dislocation densities are less stable and nucleation may occur. On the other hand, a grain with low dislocation density may grow and replace a highly strained grain by grain boundary migration (e.g. Haessner, 1978). These concepts can be introduced in plasticity models and were able to explain orientation patterns observed in experimentally deformed quartzite, halite and ice (Wenk et al., 1997) and olivine (Wenk and Tomé, 1999; Kaminski and Ribe, 2001), but there are too many unknown parameters to predict recrystallization mechanisms in lower mantle rocks. Often dynamic recrystallization randomizes orientation patterns.

4.9. Complications in polyphase systems

Perhaps the most important complication for anisotropic geodynamics is that the lower mantle is a system with two major phases of different strength. The interaction of these phases is not taken into account in most polycrystal plasticity models. Such systems are common, yet there is not much work, neither in material science nor geological environments and recommendations formulated at an interdisciplinary polyphase polycrystal plasticity workshop still apply (Bréchet et al., 1994).

Most rocks in the Earth's crust and mantle are polymineralic, yet most experimental and theoretical investigations were done on monomineralic systems and, for example in quartz-mica mixtures, CPO of quartz is greatly reduced compared with a pure quartz aggregate (Canova et al., 1992; Tullis and Wenk, 1994). Under metamorphic conditions complex reactions may occur at grain boundaries and change the fabric (e.g. Abart et al., 2004; Gaidies et al., 2017).

In most recrystallized gneisses, feldspar and quartz show barely any preferred orientation (e.g. Kern et al., 2008; Ullemeyer et al., 2006). This becomes particularly pronounced if rocks have undergone large secondary deformation, resulting in mylonites (e.g. Handy, 1994; Kern and Wenk, 1990; Herwegh et al., 2011; Linckens et al., 2011; Bercovici and Ricard, 2016). In mylonites of granitic composition the much stronger and dominant feldspar phase barely deforms and grains tumble in the much weaker and recrystallizing quartz phase (Fig. 28). A similar microstructure may be expected in highly deformed parts of the lower mantle with strong bridgmanite in a matrix of weak ferropericlase (Fig. 21a) and could explain the lack of significant anisotropy.

For the analog system neighborite-halite, Kaercher et al. (2016) have documented that for single phase systems strong CPO develops, but for mixtures CPO is greatly reduced, caused by locally heterogeneous deformation. This is also confirmed by DAC experiments for perovskite-ferropericlase mixtures (e.g. Miyagi and Wenk, 2016; Girard et al., 2016).

For the 2-phase problem with local heterogeneities, there is no straightforward polycrystal plasticity model. Canova et al. (1992) have developed an n-site viscoplastic formulation and applied it to muscovite quartz mixtures. There have been attempts with finite element approaches (e.g. Mika and Dawson, 1999) and Fourier transform methods (e.g. Lebensohn, 2001) but they are not applicable to large geophysical systems, at least for now, and particularly do not account for grain boundary sliding, which may be very significant.

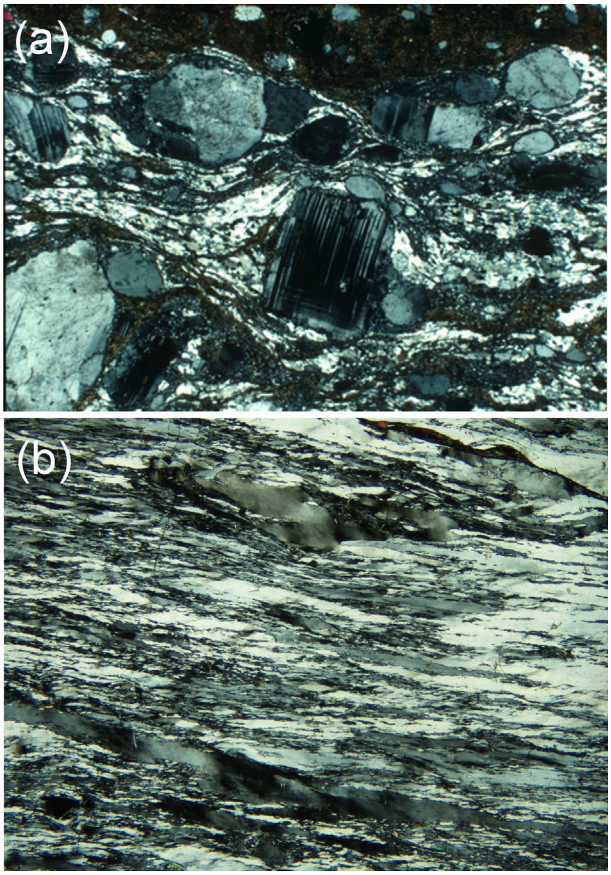

Fig. 28. (a) Thin section image of granite mylonite from the Santa Rosa mylonite zone in Southern California, with rigid strong plagioclase crystals floating in fine grained recrystallized quartz creating a viscous matrix. This represents probably a similar microstructure as bridgmanite and periclase in the lower mantle. (b) Image of deformed quartzite with feldspar inclusions from the Bergell Alps. This pervasive ductile deformation may be similar to sheared post-perovskite in the lowermost mantle. Width of images is 10 mm, crossed polarizers.

For the D″ zone, this is likely different because post-perovskite is of similar strength or weaker than ferropericlase (Fig. 21b) and thus deforms with a significant contribution of dislocation glide. The microstructure of highly strained D″ material may be more analogous to deformed quartzite with some feldspar inclusions and extremely strong preferred orientation (Fig. 28b).

5. Seismic anisotropy in the inner core

We conclude this review with a brief discussion about seismic anisotropy in the solid inner core. While the presence of a dense, possibly fluid core had been suggested long ago based on the high average density of the Earth as well as measurements of tides, its presence was confirmed by seismology in the early 20th century (Oldham, 1906; Gutenberg, 1913). An iron-nickel composition was assigned, in analogy to iron meteorites. In 1936, Inge Lehmann discovered the presence of an inner core of different elastic properties within the fluid outer core (Lehmann, 1936). Several decades later, the solidity of the inner core was demonstrated by Dziewonski and Gilbert (1971) based on the measurements of eigenfrequencies of inner core-sensitive free oscillations. Birch (1952) showed that the density of an iron-nickel alloy is too high compared to seismological estimates, and proposed the presence of ~10% of lighter elements. Since then, the structure and composition of the core was refined based on seismic, gravitational and magnetic evidence (e.g. Hirose et al., 2013).

The presence of cylindrical anisotropy in the inner core, with the fast axis aligned with the Earth's rotation axis, was first proposed thirty years ago to explain two types of independent seismic observations: (1) travel time anomalies of P waves that traverse the inner core (denoted PKIKP or PKP(DF)) on polar paths (i.e. in a direction quasi parallel to the Earth's rotation axis) arriving up to 5 s earlier than those travelling on equatorial paths (Morelli et al., 1986), and (2) anomalous splitting of inner core sensitive free oscillations (Woodhouse et al., 1986). Neither of these observations could be explained by long-wavelength heterogeneous structure in the earth's mantle. It was suggested that this anisotropy could likely be due to the alignment of intrinsically anisotropic iron crystals, and in the following decade several models for the physical cause of such alignment were proposed (Jeanloz and Wenk, 1988; Romanowicz et al., 1996; Bergman, 1997; Karato, 1999; Wenk et al., 2000b; Buffett and Wenk, 2001; Yoshida et al., 1996; see review by Sumita and Bergman, 2015).

In the decades since its discovery, many seismic studies have confirmed these early observations from ever increasing datasets, leading to a current landscape of the distribution of inner core anisotropy that is surprisingly complex for such a small volume of the Earth (e.g. Tkalčić, 2015). The top ~100 km of the 1220 km-thick inner core have been found to be isotropic, while deeper, there is evidence for a hemispherical pattern of anisotropy (Tanaka and Hamaguchi, 1997; Creager, 1999; Niu and Wen, 2002; Garcia, 2002; Waszek et al., 2011; Irving and Deuss, 2011; Lythgoe et al., 2014), with weaker anisotropy in the eastern hemisphere than in the western hemisphere. There is also evidence for depth dependence, with increased strength of anisotropy towards the center (Creager, 1992; Vinnik et al., 1994), and more recently, the suggestion of a different orientation of anisotropy in the central part of the inner core (Ishii and Dziewonski, 2002; Beghein and Trampert, 2003), dubbed "Inner Most Inner Core" (IMIC, Ishii and Dziewonski, 2002). The IMIC, as reexamined in more recent studies, would have a radius of about 550 km (e.g. Cormier and Stroujkova, 2005; Cao and Romanowicz, 2007; Lythgoe et al., 2014; Wang et al., 2015; Romanowicz et al., 2016). The signature of a hemispherical anisotropic structure has also been found from the modeling of coupling of pairs of modes sensitive to such structure (Deuss et al., 2010). In addition, regional variations in the direction of the fast axis and strength of anisotropy have been documented (e.g. Bréger et al., 1999; Sun and Song, 2008a,b; Irving, 2016). To explain this complexity, Tkalčić (2010) suggested that the inner core may be made of a patchwork of anisotropic domains of different orientations. Attenuation of PKIKP waves also presents anisotropic variations, with higher attenuation correlated with early arrivals along quasi-polar paths (Souriau and Romanowicz, 1996, 1997; Oreshin and Vinnik, 2004). We refer the reader to more complete reviews of seismological studies of inner core anisotropy (Deuss, 2014; Souriau, 2015; Tkalčić, 2015). Here, we briefly describe some of the seismological challenges that are still preventing us from a full understanding of these intriguing observations.

One of the main challenges in fully resolving the pattern of inner core anisotropy is the poor directional sampling available due to the limited distribution of sources and receivers in polar regions (e.g. Tkalčić, 2015). Thus, paths sampling the inner core at a given location from different directions, which is necessary to confirm the presence of anisotropy, are frequently lacking, making it difficult to image inner core anisotropy in three dimensions without imposing strong a priori-constraints (e.g. Sun and Song, 2008a; Lythgoe et al., 2014). The strongest anisotropy in PKIKP data is found primarily along paths from events in South Sandwich Islands (SSI) to Alaska, which dominate the set of observations in the strongly anisotropic western hemisphere that contribute to the ξ angle range between 10-30°, where ξ is the angle of the raypath in the inner core with the Earth's axis of rotation. At shorter distances (<~155°), the PKP(DF) phase can be referred to PKP(BC), which is a core phase that does not traverse the inner core (Fig. 29). This makes it possible to eliminate contributions from uncertainties in the source parameters, as well as a significant part of the effects of 3D mantle structure, given that PKP(BC) and PKP(DF) have very similar paths throughout the mantle, diverging only in the vicinity of the inner core.

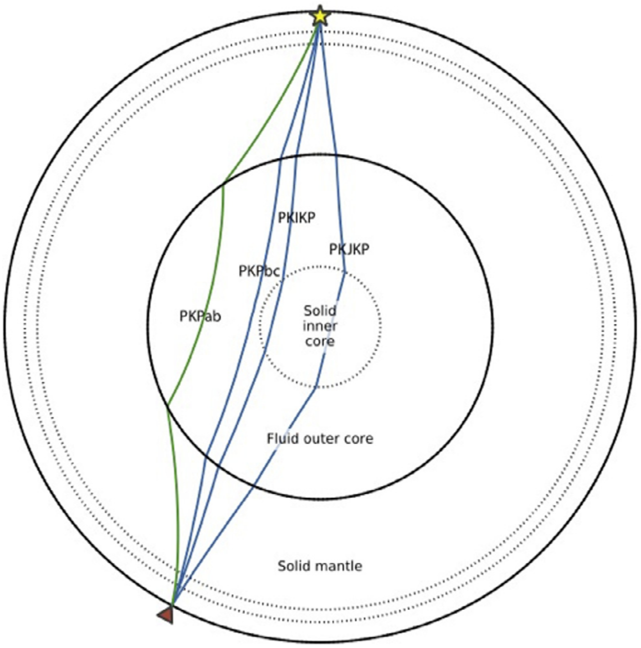

Fig. 29. Raypaths of main body wave phases used in the study of inner-core structure and anisotropy, at an epicentral distance of 155°. At this distance, all three core phases, PKIKP (also called PKP(DF)), PKP(BC) and PKP(AB) are observed. The phase PKJKP (a shear wave in the inner core) is very difficult to observe, and is plotted here only for reference.

In fact, the SSI dataset shows a wide range of travel time anomalies, ranging from 0 to >−5 s, when referred to the PKP(BC) phase, suggesting a strong local anomaly (e.g. Tkalčić et al., 2002). When plotted as a function of the angle ξ, the global PKP(BC)-PKP(DF) travel time dataset (which covers epicentral distances between 150° and 160°) forms an L-shaped curve which is not well explained by best fitting simple models of inner core anisotropy with fast axis aligned with the Earth's rotation axis (Fig. 30), for which one would expect a parabolic shape according to the equation:

$$\delta t = a + b\cos^2\xi + c\cos^4\xi$$

where a, b, c, are related to integrals of elastic anisotropic parameters along the path in the inner core.

At larger distances, the reference outer core phase is PKP(AB), which spends significant time in the highly heterogeneous D″ region at the base of the mantle. Therefore, absolute travel time anomalies of PKP(DF) are preferred, although in that case, contributions from mantle 3D structure and uncertainties in source parameters can bias the data (e.g. Bréger et al., 2000). Most studies will therefore only consider events from the high quality relocated EHB catalog (Engdahl et al., 1998) which presently exists only through 2010. Still, analysis of these PKP(DF) data indicate that, in the western hemisphere, a similar trend is observed in the absolute PKP(DF) travel time residuals as in the PKP(DF)-PKP(AB) residuals as a function of angle ξ (Fig. 30b). Most recent estimates of the corresponding anisotropy are on the order of 3–4% in the IMIC, which is considerable and difficult to reconcile with current predictions from mineral physics (see Section 6), let alone the estimate of 3–8.8% of Lythgoe et al. (2014).

To explain this trend and other aspects of complexity in travel time measurements of core sensitive phases that cannot be explained by mantle structure, Romanowicz et al. (2003) proposed alternative models that would involve structure in the outer core, with either faster than average velocities in the inner core tangent cylinder, or in polar caps at the top of the outer core, that could represent an increased concentration of light elements. For example, Fig. 31 shows the pattern obtained when plotting absolute travel time anomalies for DF,BC and AB, plotted at the entry point of the corresponding raypath into the outer core, on the Alaska side, for south-Sandwich to Alaska paths, as well as paths from Alaska to Antarctica. When plotted in this manner, the travel-time anomalies form a coherent pattern suggesting a localized anomaly that may originate near the core-mantle boundary on the Alaska side, compatible with both a polar cap in the outer core or heterogeneity within at least part of the tangent cylinder. Most anomalously split inner core sensitive normal modes could be explained by either of these models, except for mode ${}_3S_2$ which exhibits particularly strong splitting (Romanowicz and Bréger, 2000). These results have been reexamined critically by Ishii and Dziewonski (2005).

Putting structure in the outer core remains controversial (e.g. Souriau et al., 2003), as significant density anomalies in the vigorously convecting outer core appear to be ruled out (e.g. Stevenson, 1987). However, recent work suggesting the possibility of stagnant layers at the top of the outer core from magneto-hydrodynamics considerations (e.g. Buffett, 2014), indicates that at least the polar cap hypothesis should perhaps remain on the table as alternative to a strongly anisotropic region in the inner core. On the other hand, Tkalčić (2010) found that differential travel time anomalies of similar amplitude are observed on PcP-P data in the vicinity of SSI. Because such data do not sample the inner core at all, Tkalčić (2010) proposed that a significant part of the SSI anomaly could

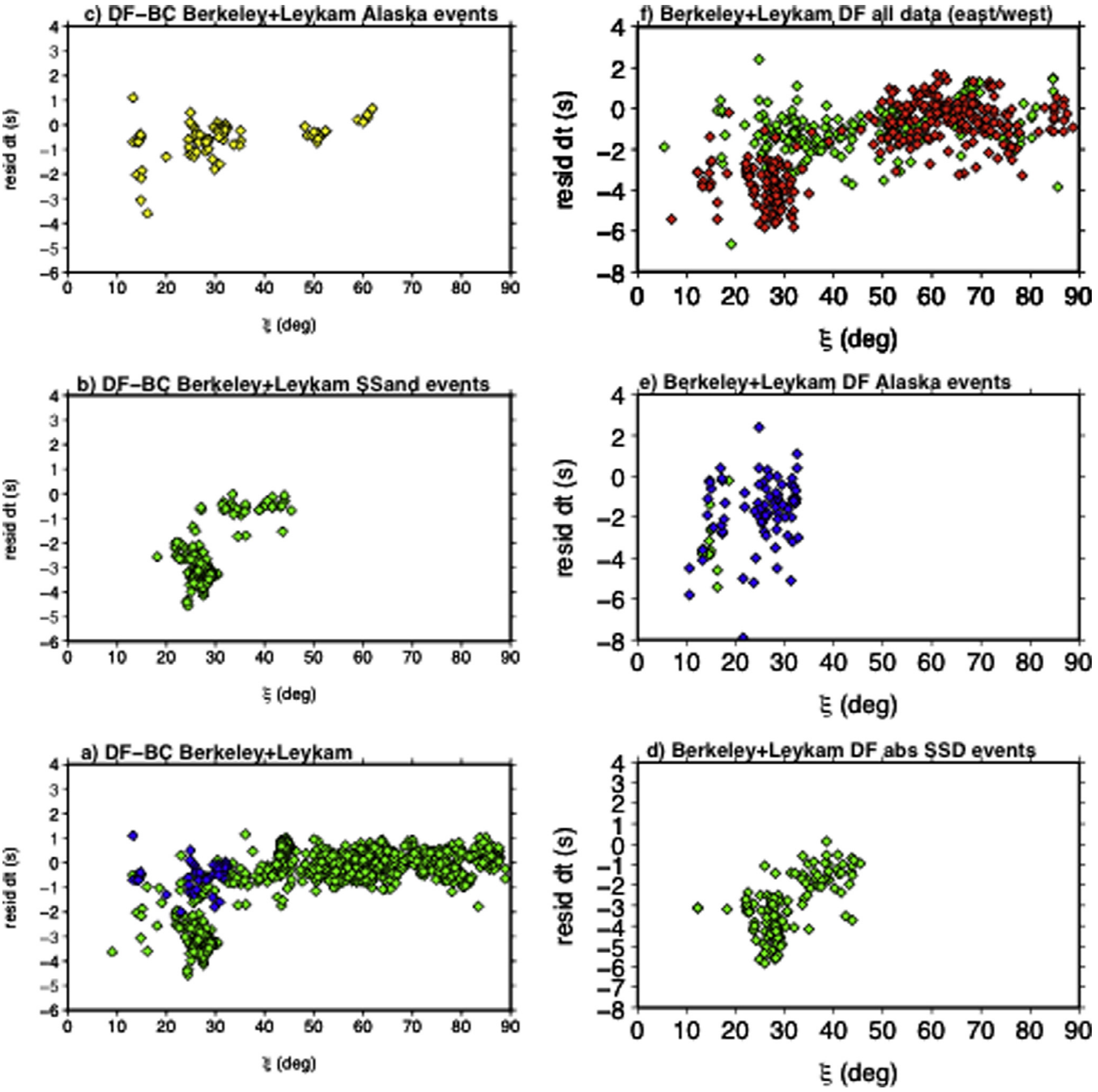

Fig. 30. Travel time anomalies of core phases as a function of angle ξ of the ray path in the inner core with respect to the Earth's rotation axis from the combined Berkeley data collection (Tkalčić et al., 2002) and from Leykam et al. (2010). Left: (DF–BC) – Right: absolute DF. a) and d) all data; b) and e): for events in the south-Sandwich Islands; c) and f) for events in Alaska.

be located in the deep mantle, although no such structure has been identified yet tomographically. Therefore, explaining the broad spread of PKP(DF) travel time anomalies on SSI paths to Alaska remains an open question, which needs to be answered before robust bounds on the strength of anisotropy in the inner core's western hemisphere can be provided to mineral physicists. Accumulation of data from the current deployment of USArray in Alaska may shed more light on this question.

This leads us to the second, and possibly related challenge that has come to light recently (Lincot et al., 2015, 2016; Romanowicz et al., 2016), which is how to reconcile the 3–8% seismic anisotropy inferred in the inner core's western hemisphere with current knowledge from mineral physics.

6. Mineral physics of the inner core

6.1. Phase relations

From the mineral physics point of view, a first order question has been the phase in which iron is present in the inner core. The high pressure ε phase of iron was first confirmed by X-ray diffraction by Mao et al. (1967) and a hexagonal close-packed (hcp) structure was identified. Since then, many high pressure experiments have been conducted. Most important are those pertinent to conditions of the inner core (Fig. 32). They include dynamic shock compression with relatively large error margins (e.g. Alfè et al., 2002; Anzellini et al., 2013; Brown, 2001; Ping

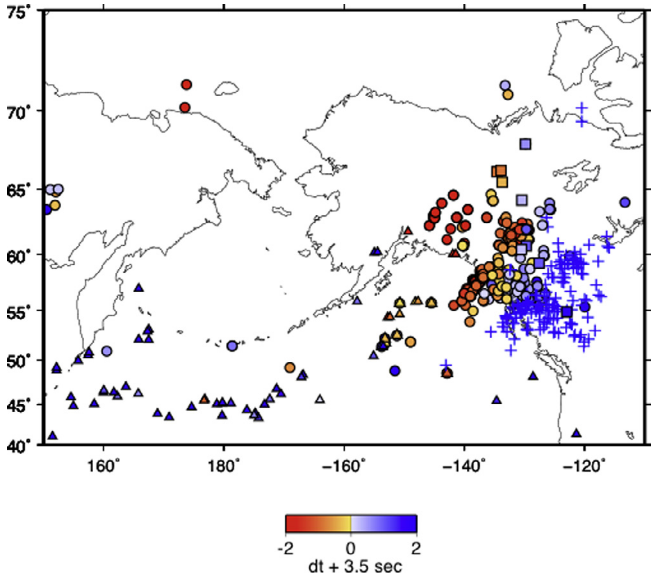

Fig. 31. Absolute travel time anomalies for DF (circles and triangles), BC (crosses) and AB (squares), for events at latitudes lower than −50°S or higher than 50°N plotted as a function of the location of the entry point of the ray path into the outer core. Triangles are for events at latitude >50°N observed at stations at latitudes <−50°S. Expanded from Romanowicz et al. (2003) to include data from Leykam et al. (2010), as also shown in Fig. 34b–f. This collection of travel time anomalies forms a coherent pattern with a sharp gradient delineating a localized boundary between very fast paths to the northwest and normal paths to the southeast, suggesting a “polar cap” pattern, that may or may not originate in the inner core. Note that the color code is centered at δt = −3.5 s.

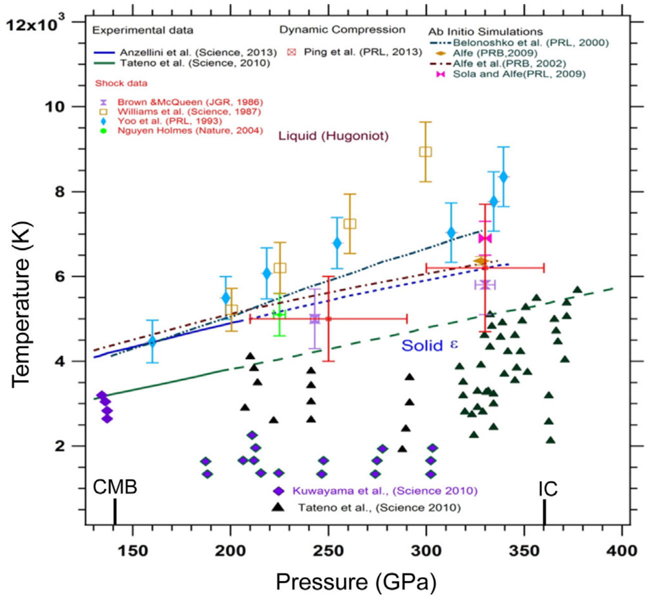

Fig. 32. Pressure–temperature phase diagram for iron at high pressure, illustrating diamond anvil and shock experiments as well as ab initio simulations. The lines correspond to melting curves (courtesy of B.K. Godwal).

et al., 2013) and DAC experiments at high pressure and temperature, up to 380 GPa and 6000 K (e.g. Tateno et al., 2010). Based on theoretical calculations, some authors have suggested that body-centered cubic (bcc) iron could be stable just below the melting point at core pressures (e.g. Vočadlo et al., 2003; Belonoshko et al., 2003, 2006; Dubrovinsky et al., 2007; Bouchet et al., 2013), but most recent studies indicate that bcc is unstable at these conditions (e.g. Godwal et al., 2015).

An important aspect is that the inner core may not be chemically and structurally homogeneous. It is likely that nickel, a component in iron meteorites, is also present in the core (Sakai et al., 2011; Tateno et al., 2012). Furthermore, to account for the lower density implied by seismic data suggests that lighter elements may be present and a good candidate is silicon. The Fe-Si system has been studied at intermediate pressure-temperatures (e.g. Sakai et al., 2011; Fischer et al., 2013, Fig. 33) and inner core conditions (Tateno et al., 2015). At high pressure and high temperature, FeSi crystallizes in the cubic B2 structure (CsCl structure) which is an ordered bcc structure. Fe_3Si forms a DO3 structure with doubling of the B2 unit cell and ordering. At lower pressures FeSi forms the B20 structure which is partially disordered bcc, with a lack of inversion symmetry (e.g. Jeong and Pickett, 2004). Elastic properties of FeSi have been investigated by Petrova et al. (2010). Badro et al. (2014) explored a range of possible elements in the core (O, S, Si, Ni) and concluded that oxygen is required in the outer core.

6.2. Causes of anisotropy in the inner core

Potential mechanisms for alignment of crystals in the inner core are dislocation-plasticity (e.g. Jeanloz and Wenk, 1988; Wenk et al., 2000a; Lincot et al., 2015, 2016), growth from a melt (e.g. Bergman, 1997; Deguen, 2012), magnetic Maxwell stresses (e.g. Karato, 1999; Buffett and Wenk, 2001).

Radial DAC experiments (e.g. Wenk et al., 2000a; Merkel et al., 2004, 2013; Miyagi et al., 2008) documented texture development in ε iron at high pressure and inferred (0001) and subordinate $\{11\bar{2}0\}$ slip, combined with mechanical twinning as potential mechanisms. However, these experiments were not at inner core conditions.

Elastic properties at core conditions rely on first principle calculations and various groups have been involved (e.g. Vočadlo et al., 2008, 2009; Mattesini et al., 2010). It is interesting to find that results are quite contradictory, as expressed in P-wave velocity profiles for hcp single crystals with the c-axis at $\xi = 0°$ (Fig. 34b). While Vočadlo et al. (2009) predict maximum velocities perpendicular to the c-axis, Mattesini et al. (2010) suggest maximum velocities parallel to the c-axis (the elastic tensor of hexagonal crystals is axially symmetric about the c-axis). Estimates of inner core seismic anisotropy are very high ($(V_{p\text{-fast}} - V_{p\text{-slow}})/V_{p\text{-iso}} = 3–8\%$; Fig. 34a), compared with the rather small P-wave anisotropy obtained from first principles calculations for single crystals (e.g. 4.9% for Vočadlo et al., 2009 at 308 GPa and 5000 K or 5.7% for Mattesini et al., 2010 at 346 GPa and 6000 K) and the best fit with seismic data would be a hexagonal single crystal aligned with the c-axis more or less parallel to the N-S axis. A huge single crystal seems unlikely, given that the largest documented crystals on Earth are about 20 m in size, and with pressure–temperature gradients, it is likely that huge crystals at high temperature would undergo transformations and recrystallization over geologic times.

A recent study (Lincot et al., 2016) constructed a multi-scale model, combining self-consistent polycrystal plasticity, inner-core formation models, and Monte Carlo simulations of elastic parameters to predict travel times of inner core PKP waves and confront them with observations. These authors found that they could explain as much as 3% seismic anisotropy with an hcp-iron structure with fast c axis, and with anomalous single crystal anisotropies near the melting point of up to 20% (Martorell et al., 2013), with dominant pyramidal ⟨c + a⟩ slip and crystal alignment provided by a low degree boundary condition for crystallization at the ICB. While this model might account for the faster PKP travel times on polar, compared to equatorial paths, it does not reproduce the L-shaped travel time anomaly curve as a function of angle ξ (Fig. 30).

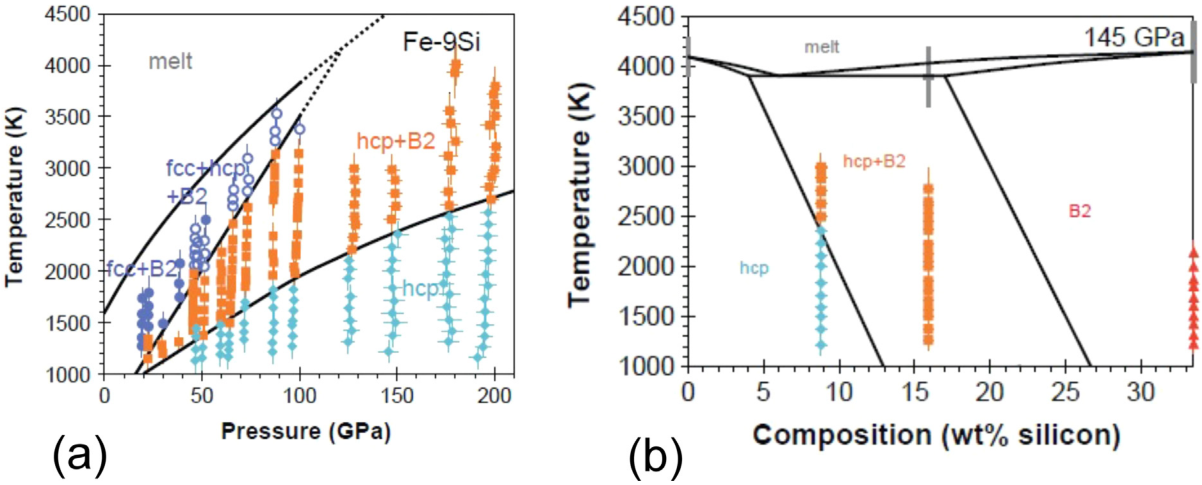

Fig. 33. Phase diagrams of the Fe-Si system (Fischer et al. 2013). (a) Pressure–temperature phase diagram illustrating stability fields of the various phases for Fe-9Si. (b) Temperature-composition diagram at 145 GPa illustrating the transition from hcp to B2.

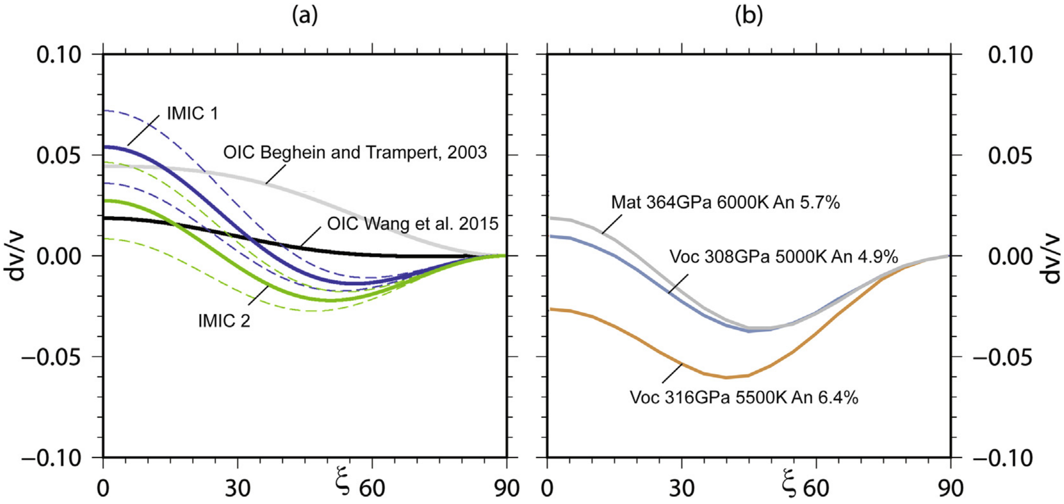

Fig. 34. (a) Comparison of relative velocity variations (in%) as a function of angle ξ of the ray path in the inner core with respect to the Earth's rotation axis for several seismological models. Black: OIC model of Wang et al. (2003); Grey: OIC model of Beghein and Trampert (2003). Blue: best fitting IMIC model using Wang et al.'s model for OIC anisotropy corrections. Green: best fitting IMIC model using Beghein and Trampert's (2003) OIC model for anisotropy corrections in the OIC. In the latter two cases the IMIC radius is held at 600 km. The IMIC model obtained is only slightly sensitive to the radius in the range 500–600 km. Dashed lines indicate the range of uncertainty on the IMIC model. (b) Calculated normalized P-wave velocities of hexagonal single crystals based on first principle elastic properties at various temperatures and pressures. An is strength of anisotropy. The polar angle ξ is zero parallel to the hexagonal c-axis. Mat: Mattesini et al., 2010, Voc: Vočadlo et al. (2009). Based on Romanowicz et al. (2016).

7. Conclusions and future directions

7.1. Anisotropy in the deep mantle

In the last ten years, global seismic tomography has provided increasingly refined images of seismic heterogeneity in the deep Earth. There is now agreement on the long wavelength structure, dominated by the presence of two low shear velocity provinces (LLSVPs) under Africa and the central Pacific, which may require compositional heterogeneity, at least at their base. There is also evidence for smaller scale structures suggestive of subducting slabs and upwelling plumes in the lower mantle. While the bulk of the lower mantle appears largely isotropic, the long wavelength pattern of VTI anisotropy detected in D″ from shear wave tomographic studies seems to track that of isotropic velocity, with SH faster than SV outside of the LLSVPs and SV faster than SH within them. However, the agreement among different models is limited to the very longest wavelengths ("degree 2″), and there are still debates about trade-offs between isotropic and anisotropic structure.

On the other hand, recent local studies of shear wave splitting are consistently showing the presence of strong seismic anisotropy (both radial and azimuthal) at the edges of the LLSVPs, primarily on the fast side. Because anisotropy in post-perovskite (pPv) is thought to be much stronger than in perovskite, and pPv is likely more widely present outside of the LLSVP (i.e. colder regions manifested by faster than average shear velocity) than inside the LLSVPs (which are likely warmer), these observations suggest that CPO of pPv may be the cause, indicating the presence of strong deformation due to constrained flow at the base of the mantle, with a change of direction towards the vertical at the border of the LLSVP, and more vertically oriented flow within it. While very attractive, because it can also explain opposite polarity behavior in reflections of P and S waves on the discontinuity at the top of D″

(Thomas et al., 2011; Cobden et al., 2015), the interpretation in terms of pPv must be considered with caution, given the uncertainties on whether pPv is actually present at deep mantle depths.

A priority for future seismic studies is to continue investigating the patterns of anisotropy on the borders of the LLSVPs as well as in the vicinity of upwelling plumes, where high concentrations of strain are expected. This would be greatly helped by installations of large aperture broadband arrays on the ocean floor, collecting high quality horizontal component data for at least 1 year, to cover gaps in the available sampling of D″ in these regions. We also lack robust constraints on deep mantle P anisotropy which would help differentiate between dominant (001) and (010) slip systems in post-perovskite.

Also mineral physics has added a lot of new information, most significantly the discovery of post-perovskite (Oganov and Ono, 2004) and derivation of deformation mechanisms, both by experiments and theoretical models. But as the anisotropic seismic structure of the Earth has become more complex over the last ten years, so has the interpretation with mineral physics concepts, opening a wide range of opportunities for new investigations. Perhaps most significant have been the recent advances in modeling crystal deformation based on bonding characteristics at a wide range of conditions that are relevant for the mantle but cannot be approached with experiments, like slow strain rates. It will be important to apply theory to experimental conditions and this might explain why DAC experiments at high pressure suggest (001) slip for $MgSiO_3$ post-perovskite (Miyagi et al., 2010; Wu et al., 2017), while bonding models predict (010) slip at deep mantle conditions (Goryaeva et al., 2016).

High pressure experiments will remain crucial. With advances in multi-anvil technology it will become possible to reach lower mantle conditions (Yamazaki et al., 2014), with larger samples and better defined deformation geometry than DAC, which is restricted to the ~50 μm range), with large gradients in pressure, deformation rates and temperature. In addition, D-DIA experiments can provide tomographic information about microstructural evolution, e.g. during phase transitions and recrystallization (Wang et al., 2011). Also DAC technology is adding new possibilities such as resistive heating for high temperature experiments, multigrain texture analysis for coarser aggregates (e.g. Barton and Bernier, 2012; Langrand et al., 2017), and the possibility of using DAC with Laue microdiffraction (Tamura, 2014) to perform orientation and microstructural mapping *in situ* at high pressure.

In the future, also a larger range of compositions needs to be explored experimentally, for example iron-magnesium content, multiphase systems (pPv, ferropericlase and $CaSiO_3$ perovskite) and the significance of perovskite/post-perovskite transformations.

Geodynamic models need refinements. New 3D models with tracers (e.g. Cottaar et al., 2014; Li, M. et al., 2014) still do not account for the very significant viscosity changes implied by mineral physics. And following texture evolution along streamlines provides results at different times for the advancing tracers, while relating anisotropy results to the Earth assumes that the streamline does not change, which is clearly not the case.

The issue of deformation mechanisms was addressed in Section 4.8. All models for lower mantle anisotropy assume dislocation glide of post-perovskite and ferropericlase as the cause of crystal alignment and use a self-consistent viscoplastic plasticity model. Some arbitrary strain fraction corrections are introduced to account for mechanisms such as climb, grain boundary migration, grain boundary sliding that do not contribute to texture. In the future, the significance of these mechanisms should be studied more systematically, both with experiments and models. There are strong indications that the activity of different mechanisms is the cause for lack of significant anisotropy in large parts of the lower mantle.

7.2. Inner core anisotropy

While the complexities of the lower mantle are developing into a realistic and solvable puzzle, inner core anisotropy is becoming more enigmatic. As we learn more about the large seismic anisotropy, it is not clear what the origin of this signal is and how much originates in the inner core. There is room for many possible interpretations, including a layered inner core with a bcc iron structure in the innermost inner core and an outer shell with an hcp structure (Wang et al., 2015). While such a structure is not impossible, it is quite unlikely (e.g. Romanowicz et al., 2016), and not presently resolvable from seismological observations. The high axial velocities, compared with equatorial velocities are difficult to explain, and particularly the striking L-shape of the PKP travel time residual as a function of angle of the raypath in the inner core with respect to the rotation axis. It is not impossible that heterogeneous structures in the outer liquid core, particularly columnar convection with a characteristic seismic pattern (e.g. Jones, 2011; Soderlund et al., 2012), influence the apparent seismic signature of the inner core. A priority for future seismic studies, in our view, is to achieve consensus on the origin of the observed L-shape mentioned above. The dense temporary broadband arrays recently installed in Alaska (as part of the Earthscope program) and in Antarctica should help in that endeavor.

On the mineral physics side, there is general agreement that hexagonal close-packed iron is the most likely component but the actual composition is still debated and an iron-silicon alloy may exist. There is uncertainty and disagreement about elastic properties of pure iron at inner core conditions derived with first principles calculations (e.g. Vočadlo et al., 2009 versus Mattesini et al., 2010) and no information about elastic properties of iron-silicon alloys. While there are many experiments documenting phase relations both of Fe and Fe-Si at high pressure and temperature (e.g. Tateno et al., 2010, 2015), there is still considerable uncertainty about the melting temperature.

These studies highlight the chemical and structural complexities of the core, with likely heterogeneities in the inner core, variable elastic properties and anisotropy. A multi-disciplinary approach including seismologists, geodynamicists, mineral physicists and material scientists is required to make progress. Such collaborations have been initiated and show great promise for the near future.

Acknowledgements

We are grateful to Mark Jellinek and Tim Horscroft for inviting us to prepare this review. It was an opportunity for us to explore the extensive literature on the subject and also to discover that a lot of work remains to be done. Particularly interesting was interaction with colleagues and students at the 2016 CIDER Workshop in Santa Barbara. HRW is appreciative of discussions with Rainer Abart, Sanne Cottaar, Patrick Cordier, Thorne Lay, Sebastien Merkel, Lowell Miyagi and Kaiqing Yuan. CIDER is funded through NSF (FESD grant EAR 1135452). We acknowledge support from NSF (EAR 1343908, 1417229, CSEDI-106751), DOE (DE-FG02-05ER15637), CDAC. We acknowledge constructive reviews by Mark Jellinek and Maureen Long.

References

Abart, R., Kunze, K., Milke, R., Sperb, R., Heinrich, W., et al., 2004. Silicon and oxygen self diffusion in enstatite polycrystals: the Milke (2001) rim growth experiments revisited. Contrib. Mineral. Petrol. 147, 633–646. http://dx.doi.org/10.1007/s00410-004-0596-9.

Alfè, D., Price, G.D., Gillan, M.J., 2002. Iron under Earth's core conditions: Liquid-state thermodynamics and high pressure melting curve from ab initio calculations. Phys. Rev. B 65 (16), 165118. http://dx.doi.org/10.1103/PhysRevB.65.165118.

Ammann, M., Brodholt, J., Wookey, J., Dobson, D., 2010. First-principles constraints on diffusion in lower-mantle minerals and a weak D'' layer. Nature 465, 462–465. http://dx.doi.org/10.1038/nature09052.

Amodeo, J., Carrez, P., Cordier, P., 2012. Modelling the effect of pressure on the critical shear stress of MgO single crystals. Philos. Mag. 92, 1523–1541. http://dx.doi.org/10.1080/14786435.2011.652689.

Amodeo, J., Devincre, B., Carrez, P., Cordier, P., 2014. Dislocation reactions, plastic anisotropy and forest strengthening in MgO at high temperature. Mech. Mater. 71, 62–73.

Amodeo, J., Dancette, S., Delannay, L., 2016. Atomistically-informed crystal plasticity in MgO polycrystals under pressure. Int. J. Plasticity 82, 177–191. http://dx.doi.org/10.1016/j.ijplas.2016.03.004.

Anzellini, S., Dewaele, A., Mezouar, M., Loubeyre, P., Morard, G., 2013. Melting of iron at Earth's inner core boundary based on fast X-ray diffraction. Science 340, 464–466. http://dx.doi.org/10.1126/science.1233514.

Ashby, M.F., 1972. A first report on deformation-mechanism maps. Acta Metall. 20, 887–897.

Auer, L., Boschi, L., Becker, T.W., Nissen-Meyer, T., Giardini, D., 2014. Savani: a variable resolution whole-mantle model of anisotropic shear-velocity variations based on multiple data sets. J. Geophys. Res. 119, 3006–3034. http://dx.doi.org/10.1002/2013JB010773.

Backus, G.E., 1962. Long-wave elastic anisotropy produced by horizontal layering. J. Geophys. Res. 67, 4427–4440.

Badro, J., Fiquet, G., Guyot, F., Rueff, J.-P., Struzhkin, V.V., Vanko, G., Monaco, G., 2003. Iron partitioning in Earth's mantle: toward a deep lower mantle discontinuity. Science 300, 789–791. http://dx.doi.org/10.1126/science.1081311.

Badro, J., Cote, A.S., Brodholt, J.P., 2014. A seismologically consistent compositional model of Earth's core. Proc. Nat. Acad. Sci. 111, 7542–7545.

Barton, N.R., Bernier, J.V., 2012. A method for intragranular orientation and lattice strain distribution determination. J. Appl. Cryst. 45, 1145–1155. http://dx.doi.org/10.1107/S0021889812040782.

Becker, T.W., 2006. On the effect of temperature and strain-rate dependent viscosity on global mantle flow, net rotation, and plate-driving forces. Geophys. J. Int. 167, 943–957.

Beghein, C., Trampert, J., 2003. Robust normal mode constraints on inner-core anisotropy from model space search. Science 299, 552–555. http://dx.doi.org/10.1126/science.1078159.

Beghein, C., Trampert, J., Heijst, H.V., 2006. Radial anisotropy in seismic reference models of the mantle. J. Geophys. Res. 111 (B2), B02303. http://dx.doi.org/10.1029/2005JB003728.

Belonoshko, A.B., Ahuja, R., Johansson, B., 2003. Stability of the body-centered-cubic phase of iron in the Earth's inner core. Nature 424, 1032–1034. http://dx.doi.org/10.1038/nature01954.

Belonoshko, A.B., Isaev, E.I., Skorodumova, N.V., Johansson, B., 2006. Stability of the body-centered-tetragonal phase of Fe at high pressure: ground-state energies, phonon spectra, and molecular dynamics simulations. Phys. Rev. B 74, 214102.

Bercovici, D., Ricard, Y., 2016. Grain-damage hysteresis and plate-tectonic states. Phys. Earth Planet. Int. 253, 31–47. http://dx.doi.org/10.1016/j.pepi.2016.01.005.

Bergman, M.I., 1997. Measurements of elastic anisotropy due to solidification texturing and the implications for the Earth's inner core. Nature 389, 60–63. http://dx.doi.org/10.1038/37962.

Beyerlein, I.J., Lebensohn, R.A., Tomé, C.N., 2003. Modeling texture and microstructural evolution in the equal channel angular extrusion process. Mater. Sci. Eng. A 345, 122–138.

Birch, F., 1952. Elasticity and constitution of the Earth's interior. J. Geophys. Res. 57, 227–286.

Blackman, D.K., Kendall, J.-M., Dawson, P.R., Wenk, H.-R., Boyce, D., Morgan, J.P., 1996. Teleseismic imaging of subaxial flow at mid-ocean ridges: travel-time effects of anisotropic mineral texture in the mantle. Geoph. J. Intern. 127, 415–426.

Blackman, D.K., Wenk, H.-R., Kendall, J.-M., 2002. Seismic anisotropy of the upper mantle: 1. Factors that affect mineral texture and effective elastic properties. Geochem. Geophys. Geosyst. 3 (9), 8601. http://dx.doi.org/10.1029/2001GC000248.

Boioli, F., Carrez, P., Cordier, P., Devincre, B., Marquille, M., 2015. Modeling the creep properties of olivine by 2.5-dimensional dislocation dynamics simulations. Phys. Rev. B 92 (1), 014115. http://dx.doi.org/10.1103/PhysRevB.92.014115.

Boioli, F., Carrez, P., Cordier, P., Devincre, B., Gouriet, K., Hirel, P., Kraych, A., Ritterbex, S., 2017. Pure climb creep mechanism drives flow in Earth's lower mantle. Sci. Adv. 3. http://dx.doi.org/10.1126/sciadv.1601958.

Bolfan-Casanova, N., Keppler, H., Rubie, D.C., 2003. Water partitioning at 660 km depth and evidence for very low water solubility in magnesium silicate perovskite. Geophys. Res. Lett. 30, 1905. http://dx.doi.org/10.1029/2003GL017182.

Borgeaud, A.F.E., Konishi, K., Kawai, K., Geller, R.J., 2016. Finite frequency effects on apparent S-wave splitting in the D'' layer: comparison between ray theory and full-wave synthetics. Geophys. J. Int. 207, 12. http://dx.doi.org/10.193/gji/ggw254.

Boschi, L., Dziewonski, A.M., 2000. Whole earth tomography from delay times of P, PcP and PKP phases: lateral heterogeneities in the outer core or radial anisotropy in the mantle? J. Geophys. Res. 105, 13675–13696.

Bouchet, J., Mazavet, S., Morard, G., Guyot, F., Musella, M., 2013. Ab initio equation of state of iron up to 1500 GPa. Phys. Rev. B 87 (9), 094102. http://dx.doi.org/10.1103/PhysRevB.87.094102.

Bréchet, Y.J.M., Dawson, P., Embury, J.D., Gsell, C., Suresh, S., Wenk, H.-R., 1994. Recommendations on modeling polyphase plasticity: conclusions of panel discussions. Mat. Sci. Eng. A175, 1–5.

Bréger, L., Romanowicz, B., Tkalcic, H., 1999. PKP(BC-DF) travel time residuals and short scale heterogeneity in the deep earth. Geophys. Res. Lett. 26 (20), 3169–3172. http://dx.doi.org/10.1029/1999GL008374.

Bréger, L., Tkalcic, H., Romanowicz, B., 2000. The effect of D'' on PKP(AB-DF) travel time residuals and possible implications for inner core structure. Earth Planet. Sci. Lett. 175, 133–143. http://dx.doi.org/10.1016/S0012-821X(99)00286-1.

Brown, J.M., 2001. The equation of state of iron to 450 GPa: Another high pressure solid phase? Geophys. Res. Lett. 28, 4339–4342. http://dx.doi.org/10.1029/2001GL013759.

Buffett, B.A., 2014. Geomagnetic fluctuations reveal stable stratification at the top of the Earth's core. Nature 507, 484–487. http://dx.doi.org/10.1038/nature13122.

Buffett, B.A., Wenk, H.R., 2001. Texturing of the Earth's inner core by Maxwell stresses. Nature 413, 60–63. http://dx.doi.org/10.1038/35092543.

Bunge, H.-P., Richards, M.A., Baumgardner, J.R., 1996. Effect of depth-dependent viscosity on the planform of mantle convection. Nature 379, 436–438. http://dx.doi.org/10.1038/379436a0.

Cann, J.R., 1968. Geological processes at mid-oceanic ridge crests. Geophys. J. R. Astron. Soc. 15, 331–341.

Canova, G.R., Wenk, H.-R., Molinari, A., 1992. Deformation modelling of multiphase polycrystals: case of a quartz-mica aggregate. Acta Metall. 40, 1519–1530.

Cao, A., Romanowicz, B., 2007. Test of the innermost inner core models using broadband PKIKP travel time residuals. Geophys. Res. Lett. 34, L08303. http://dx.doi.org/10.1029/2007GL029384.

Carrez, P., Ferré, D., Cordier, P., 2007. Implications for plastic flow in the deep mantle from modelling dislocations in $MgSiO_3$ minerals. Nature 446, 68–70. http://dx.doi.org/10.1038/nature05593.

Castelnau, O., Blackman, D.K., Becker, T.W., 2009. Numerical simulations of texture development and associated rheological anisotropy in regions of complex mantle flow. Geophys. Res. Lett. 36. L12304 (1-6).

Catalli, K., Shim, S.H., Prakapenka, V.B., 2009. Thickness and Clapeyron slope of the post-perovskite boundary. Nature 462, 782–785. http://dx.doi.org/10.1038/nature08598.

Catalli, K., Shim, S.H., Prakapenka, V.B., Zhao, J.Y., Sturhahn, W., Chow, P., Xiao, Y.M., Liu, H.Z., Cynn, H., Evans, W.J., 2010. Spin state of ferric iron in $MgSiO_3$ perovskite and its effect on elastic properties. Earth Planet. Sci. Lett. 289, 68–75. http://dx.doi.org/10.1016/j.epsl.2009.10.029.

Chang, S.-J., Ferreira, A.M., Ritsema, J., van Heijst, H.J., Woodhouse, J.H., 2014. Global radially anisotropic mantle structure from multiple datasets: a review, current challenges, and outlook. Tectonophysics 617, 1–19. http://dx.doi.org/10.1016/j.tecto.2014.01.033.

Chang, S.-J., Ferreira, A.M.G., Ritsema, J., van Heijst, H.J., Woodhouse, J.H., 2015. Joint inversion for global isotropic and radially anisotropic mantle structure including crustal thickness perturbations. J. Geophys. Res. Solid Earth 120 (6), 4278–4300. http://dx.doi.org/10.1002/2014JB011824.

Chen, I., Argon, A., 1979. Grain boundary and interphase boundary sliding in power law creep. Acta Metall. 27, 749–754.

Christensen, U., 1987. Some geodynamical effects of anisotropic viscosity. Geophys. J. Int. 91, 711–736. http://dx.doi.org/10.1111/j.1365-246X.1987.tb01666.x.

Cobden, L., Thomas, C., Trampert, J., 2015. Seismic detection of post-perovskite inside the Earth. In: Khan, A., Deschamps, F. (Eds.), The earth's heterogeneous mantle. Springer Geophysics. http://dx.doi.org/10.1007/978-3-319-15627-9_13. chapter 13.

Conrad, C.P., Lithgow-Bertelloni, C., 2004. The temporal evolution of plate driving forces: importance of "slab suction" versus "slab pull" during the Cenozoic. J. Geophys. Res. 109, B10407. http://dx.doi.org/10.1029/2004JB002991.

Cordier, P., Amodeo, J., Carrez, P., 2012. Modelling the rheology of MgO under Earth's mantle pressure, temperature and strain rates. Nature 481, 177–180. http://dx.doi.org/10.1038/nature10687.

Cormier, V.F., Stroujkova, A., 2005. Waveform search for the innermost inner core. Earth Planet. Sci. Lett. 236 (1–2), 96–105. http://dx.doi.org/10.1016/j.epsl.2005.05.016.

Cottaar, S., Li, M., McNamara, A., Romanowicz, B., Wenk, H.-R., 2014. Synthetic seismic anisotropy models within a slab impinging on the core-mantle boundary. Geophys. J. Int. 199, 164–177. http://dx.doi.org/10.1093/gji/ggu244.

Cottaar, S., Romanowicz, B., 2013. Observations of changing anisotropy across the southern margin of the African LLSVP. Geophys J Int 195 (2), 1184–1195. http://dx.doi.org/10.1093/gji/ggt285.

Crampin, S., 1984. Evaluation of anisotropy by shear wave splitting: Theory, background, and field studies. Geophysics 20, 23–33.

Creager, K.C., 1992. Anisotropy of the inner core from differential travel times of the phases PKP and PKiKP. Nature 356, 309–314. http://dx.doi.org/10.1038/356309a0.

Creager, K.C., 1999. Large-scale variations in inner core anisotropy. J. Geophys. Res. 104, 23127–23139.

Dawson, P.R., Wenk, H.-R., 2000. Texturing of the upper mantle during convection. Phil. Mag. A 80 (3), 573–598. http://dx.doi.org/10.1080/01418610008212069.

Debayle, E., Ricard, Y., 2013. Seismic observations of large-scale deformation at the bottom of fast moving plates. Earth Planet. Sci. Lett. 376, 165–177. http://dx.doi.org/10.1016/j.epsl.2013.06.025.

De Bresser, J., ter Heege, J., Spiers, C., 2001. Grain size reduction by dynamic recrystallization: can it result in major rheological weakening? Int. J. Earth Sci. 90, 28–45.

Deguen, R., 2012. Structure and dynamics of Earth's inner core. Earth Planet. Sci. Lett. 333–334, 211–225. http://dx.doi.org/10.1016/j.epsl.2012.04.038.

Deuss, A., 2014. Heterogeneity and anisotropy of Earth's Inner Core. Annu. Rev. Earth Planet. Sci. 42, 103–126.

Deuss, A., Irving, J.C.E., Woodhouse, J.H., 2010. Regional variation of inner core anisotropy from seismic normal mode observations. Science 328, 1018–1020. http://dx.doi.org/10.1126/science.1188596.

Devincre, B., Kubin, L.P., 1997. The modelling of dislocation dynamics: elastic behavior versus core properties. Phil. Trans. R. Soc. Lond. A 355, 2003–2012.

De Wit, R.W.L., Trampert, J., 2015. Robust constraints on average radial lower mantle anisotropy and consequences for composition and texture. Earth Planet. Sci. Lett. 429, 101–109. http://dx.doi.org/10.1016/j.epsl.2015.07.057.

D'Halloy, d'Omalius J.-B., 1833. Introduction à la Géologie. Levrault, Paris.

Ding, X., Helmberger, D.V., 1997. Modelling D″ structure beneath Central America with broadband seismic data. Phys. Earth Planet. Inter. 101, 245–270. http://dx.doi.org/10.1016/S0031-9201(97)00001-0.

Dobson, D.P., Miyajima, N., Nestola, F., Alvaro, M., Casati, N., Liebske, C., Wood, I.G., Walker, A.M., 2013. Strong inheritance of texture between perovskite and postperovskite in the D″ layer. Nature Geosci. 6, 575–578. http://dx.doi.org/10.1038/ngeo1844].

Dubrovinsky, L., Dubrovinskaia, N., Prakapenka, V., Seifert, F., Langenhorst, F., Dmitriev, V., Weber, H., Le Bihan, T., 2004. A class of new high-pressure silica polymorphs. Phys. Earth Planet. Inter. 143, 231–240.

Dubrovinsky, L., Dubrovinskaia, N., Narygina, O., Kantor, I., Kuznetzov, A., Prakapenka, V.B., Vitos, L., Johansson, B., Mikhaylushkin, A.S., Simak, S.I., Abrikosov, I.A., 2007. Body centered cubic iron nickel alloy in Earth's core. Science 316, 1880–1883. http://dx.doi.org/10.1126/science.1142105.

Dubrovinsky, L., Glazyrin, K., McCammon, C., Narygina, O., Greenberg, E., Ubelhack, S., Chumakov, A.I., Pascarelli, S., Prakapenka, V., Bock, J., Dubrovinskaia, N., 2009. Portable laser-heating system for diamond anvil cells. J. Synchr. Rad. 16 (6), 737–741. http://dx.doi.org/10.1107/S0909049509039065.

Dziewonski, A.M., Gilbert, F., 1971. Solidity of the inner core of the Earth inferred from normal mode observations. Nature 234, 465–466. http://dx.doi.org/10.1038/234465a0.

Dziewonski, A.M., Anderson, D.L., 1981. Preliminary reference Earth model. Phys. Earth Planet. Inter. 25, 297–356. http://dx.doi.org/10.1016/0031-9201(81)90046-7.

Ekström, G., 2011. A global model of Love and Rayleigh surface wave dispersion and anisotropy, 25–250s. Geophys. J. Int. 187 (3), 1668–1686. http://dx.doi.org/10.1111/j.1365-246X.2011.05225.x.

Engdahl, E.R., van der Hilst, R., Buland, R., 1998. Global teleseismic earthquake relocation with improved times and procedures for depth determination. Bull. Seismol. Soc. Amer. 88, 722–743.

Fei, Y.W., Zhang, L., Corgne, A., Watson, H., Ricolleau, A., Meng, Y., Prakapenka, V., 2007. Spin transition and equations of state of (Mg, Fe)O solid solutions. Geophys. Res. Lett. 34, L17307. http://dx.doi.org/10.1029/2007GL030712.

Ferré, D., Cordier, P., Carrez, P., 2009. Dislocation modeling in calcium silicate perovskite based on Peierls-Nabarro model. Amer. Mineral. 94 (1), 135–142. http://dx.doi.org/10.2138/am.2009.3003.

Fischer, R.A., Campbell, A.J., Reaman, D.M., Miller, N.A., Heinz, D.L., Dera, P., Prakapenka, V.B., 2013. Phase relations in the Fe-FeSi system at high pressures and temperatures. Earth Planet. Sci. Lett. 373, 54–64. http://dx.doi.org/10.1016/j.epsl.2013.04.035.

Ford, H.A., Long, M.D., 2015. A regional test of global models for flow, rheology, and seismic anisotropy at the base of the mantle. Phys. Earth Planet. Inter. 245, 71–75. http://dx.doi.org/10.1016/j.pepi.2015.05.004.

Ford, S.R., Garnero, E.J., McNamara, A.K., 2006. A strong lateral shear velocity gradient and anisotropy heterogeneity in the lowermost mantle beneath the southern Pacific. J. Geophys. Res. 111, B03306. http://dx.doi.org/10.1029/2004JB003574.

Ford, H.A., Long, M.D., He, X., Lynner, C., 2015. Lowermost mantle flow at the eastern edge of the African Large Low Shear Velocity Province, Earth Planet. Sci. Lett. 420, 12–22. http://dx.doi.org/10.1016/j.epsl.2015.03.029.

Fouch, M.J., Fischer, K.M., Wysession, M.E., 2001. Lowermost mantle anisotropy beneath the Pacific: imaging the source of the Hawaiian plume. Earth Planet. Sci. Lett. 190, 167–180. http://dx.doi.org/10.1016/S0012-821X(01)00380-6.

French, S.W., Romanowicz, B.A., 2014. Whole-mantle radially anisotropic shear velocity structure from spectral-element waveform tomography. Geophys. J. Int. 199, 1303–1327. http://dx.doi.org/10.1093/gji/ggu334.

Frost, D.J., Liebske, C., Langenhorst, F., McCammon, C.A., Tronnes, R.G., Rubie, D.C., 2004. Experimental evidence for the existence of iron-rich metal in the Earth's lower mantle. Nature 428, 409–412. http://dx.doi.org/10.1038/nature02413.

Frost, H.J., Ashby, M.F., 1982. Deformation mechanism maps. The plasticity and creep of metals and ceramics. Pergamon, Oxford.

Gaidies, F., Milke, R., Heinrich, W., Abart, R., 2017. Metamorphic mineral reactions: porphyroblast, corona and symplectic growth. EMO Notes Mineral. 16 (14), 469–540. http://dx.doi.org/10.1180/EMU-notes.16.14.

Garcia, R., 2002. Constraints on upper inner-core structure from waveform inversion of core phases. Geophys. J. Int. 150, 651–664. http://dx.doi.org/10.1046/j.1365-246X.2002.01717.x.

Garnero, E.J., Lay, T., 1997. Lateral variations in lowermost mantle shear wave anisotropy beneath the North Pacific and Alaska. J. Geophys. Res. 102 (B4), 8121–8135. http://dx.doi.org/10.1029/96JB03830.

Garnero, E.J., Maupin, V., Lay, T., Fouch, M.J., 2004a. Variable azimuthal anisotropy in Earth's lowermost mantle. Science 306, 259–261. http://dx.doi.org/10.1126/science.1103411.

Garnero, E.J., Moore, M.M., Lay, T., Fouch, M.J., 2004b. Isotropy or weak vertical transverse isotropy in D″ beneath the Atlantic Ocean. J. Geophys. Res. 109 (B8), B08308. http://dx.doi.org/10.1029/2004JB003004.

Girard, J., Amulele, G., Farla, R., Mohiuddin, A., Karato, S.-I., 2016. Shear deformation of bridgmanite and magnesiowuestite aggregates at lower mantle conditions. Science 351, 144–147. http://dx.doi.org/10.1126/science.aad3113.

Godwal, B.K., Gonzalez-Cataldo, F., Verma, A.K., Stixrude, L., Jeanloz, R., 2015. Stability of iron crystal structures at 0.3–1.5 TPa. Earth Planet. Sci. Lett. 409, 299–306. http://dx.doi.org/10.1016/j.epsl.2014.10.056.

Goryaeva, A.M., Carrez, P., Cordier, P., 2015. Modeling defects and plasticity in $MgSiO_3$ post-perovskite: Part 2—screw and edge [100] dislocations. Phys. Chem. Min. 42, 793–803. http://dx.doi.org/10.1007/s00269-015-0763-8.

Green, G., 2016. Low viscosity and high attenuation in $MgSiO_3$ post-perovskite inferred from atomic-scale calculations. Nature Sci. Rep. 6, 34771. doi:10.1038/srep34771.

Green, G., 1838. On the reflexion and refraction of sound. Trans. Philos. Soc. London 7. 24 p.

Green, H.W., 1980. On the thermodynamics of non-hydrostatically stressed solids. Phil. Mag. A 41, 637–647.

Griggs, D.T., 1936. Deformation of rocks under high confining pressure. J. Geol. 44, 541–577.

Grocholski, B., Shim, S.H., Prakapenka, V.B., 2013. Stability, metastability, and elastic properties of a dense silica polymorph, seifertite. J. Geophys. Res. E Planets 118, 4745–4757. http://dx.doi.org/10.1002/jgrb.5036.

Gurnis, M., Hager, B.H., 1988. Controls on the structure of subducted slabs. Nature 335, 317–321.

Gutenberg, B., 1913. Über die Konstitution des Erdinnern, erschlossen aus Erdbebenbeobachtungen. Physikalische Zeitschrift 14, 1217–1218.

Haessner, F., 1978. Recrystallization of metallic materials. Riederer, Stuttgart.

Hager, B.H., O'Connell, R.J., 1981. A simple model of plate dynamics and mantle convection. J. Geophys. Res. 86, 4843–4868.

Hall, S., Kendall, J., van der Baan, M., 2004. Some comments on the effects of lower-mantle anisotropy on SKS and SKKS phases. Phys. Earth Planet. Inter. 146 (3–4), 469–481.

Handy, M., 1994. Flow laws for rocks containing two non-linear viscous phases: a phenomenological approach. J. Struct. Geol. 16 (3), 287–301. http://dx.doi.org/10.1016/0191-8141(94)90035-3.

Hansen, L.N., Zimmerman, M.E., Kohlstedt, D.L., 2011. Grainboundary sliding in San Carlos olivine: flow law parameters and crystallographic-preferred orientation. J. Geophys. Res. 116 (B8). http://dx.doi.org/10.1029/2011JB008220.

Hansen, L.N., Zimmerman, M.E., Kohlstedt, D.L., 2012. The influence of microstructure on deformation of olivine in the grain-boundary sliding regime. J. Geophys. Res. 117, B09201. http://dx.doi.org/10.1029/2012JB009305.

He, X., Long, M.D., 2011. Lowermost mantle anisotropy beneath the northwest-ern Pacific: evidence from PcS, ScS, SKS, and SKKS phases. Geochem. Geophys. Geosyst. 12, Q12012. http://dx.doi.org/10.1029/2011GC003779.

Hernlund, J.W., Thomas, C., Tackley, P.J., 2005. A doubling of the post-perovskite phase boundary and structure of the Earth's lowermost mantle. Nature 434, 882–886.

Herwegh, M., Linckens, J., Ebert, A., Berger, A., Brodhag, S.H., 2011. The role of second phases for controlling microstructural evolution in polymineralic rocks: a review. J. Struct. Geol. 33 (12), 1728–1750. http://dx.doi.org/10.1016/j.jsg.2011.08.011.

Hess, H.H., 1964. Seismic anisotropy of the uppermost mantle under oceans. Nature 203, 629–631.

Hill, R., 1952. The elastic behaviour of a crystalline aggregate. Proc. Phys. Soc. London Sect. A 65, 349–354.

Hirose, K., Labrosse, S., Hernlund, J., 2013. Composition and state of the core. Ann. Rev. Earth Planet. Sci. 41, 657–691.

Hornby, B.E., Schwartz, L.M., Hudson, J.A., 1994. Anisotropic effective-medium modeling of the elastic properties of shales. Geophysics 59 (10), 1570–1583. http://dx.doi.org/10.1190/1.1443546.

Hunt, S.A., Weidner, D.J., Li, L., Wang, L., Walte, N.P., Brodholt, J.P., Dobson, D.P., 2009. Weakening of calcium iridate during its transformation from perovskite to postperovskite. Nature Geosci. 2, 794–797. http://dx.doi.org/10.1038/ngeo663.

Irifune, T., Ringwood, A.E., 1993. Phase transformations in subducted oceanic crust and buoyancy relationships at depths of 600–800 km in the mantle. Earth Planet. Sci. Lett. 117, 101–110. http://dx.doi.org/10.1016/0012-821X(93)90120-X.

Irifune, T., Tsuchiya, T., 2015. Phase transitions and mineralogy of the lower mantle. . 2nd ed. Treatise on Geophysics 2nd ed., vol. 2, pp. 33–60.

Irving, J.C.E., 2016. Imaging the inner core under Africa and Europe. Phys. Earth Planet. Inter. 254, 12–24. http://dx.doi.org/10.1016/j.pepi.2016.03.001.

Irving, J.C.E., Deuss, A., 2011. Hemispherical structure in inner core velocity anisotropy. J. Geophys. Res. 116, B04307. http://dx.doi.org/10.1029/2010JB007942.

Ishii, M., Tromp, J., 1999. Normal mode and free-air gravity constraints on lateral variations in velocity and density of Earth's mantle. Science 285, 1231–1236. http://dx.doi.org/10.1126/science.285.5431.1231.

Ishii, M., Dziewonski, A.M., 2002. The innermost inner core of the earth: Evidence for a change in anisotropic behavior at the radius of about 300 km. Proc. Natl. Acad. Sci. 99, 14026–14030.

Ishii, M., Dziewonski, A.M., 2005. Constraints on the outer-core tangent cylinder using normal-mode splitting measurements. Geophys. J. Int. 162, 787–792. http://dx.doi.org/10.1111/j.1365-246X.2005.02587.x.

Jackson, I., Faul, U.H., 2010. Grainsize-sensitive viscoelastic relaxation in olivine: towards a robust laboratory-based model for seismological applications. Phys. Earth Planet. Inter. 183, 151–163. http://dx.doi.org/10.1016/j.pepi.2010.09.005.

Jeanloz, R., Wenk, H.-R., 1988. Convection and anisotropy of the inner core. Geophys. Res. Lett. 15, 72–75. http://dx.doi.org/10.1029/GL015i001p00072.

Jeong, T., Pickett, W.E., 2004. Implications of the B20 crystal structure for the magnetoelectronic structure of MnSi. Phys. Rev. B 70, 075114. doi.org/10.1103/PhysRevB.70.075114.

Jones, C.A., 2011. Planetary magnetic fields and fluid dynamos. Annual Rev. Fluid. Mech. 43, 583–614.

Jung, H., Karato, S., 2001. Water-induced fabric transitions in olivine. Science 293, 1460–1463. http://dx.doi.org/10.1126/science.1062235.

Jung, H., Katayama, I., Jiang, Z., Hiraga, T., Karato, S., 2006. Effects of water and stress on the lattice preferred orientation in olivine. Tectonophysics 421, 1–22.

Kaercher, P., Miyagi, L., Kanitpanyacharoen, W., Zepeda-Alarcon, E., Wang, Y., Parkinson, D., Lebensohn, R.A., De Carlo, F., Wenk, H.R., 2016. Two phase deformation of lower mantle mineral analogs. Earth Planet. Sci. Lett. 456, 134–145. doi.org/10.1016/j.epsl.2016.09.030.

Kamb, W.B., 1961. The thermodynamic theory of nonhydrostatically stressed solids. J. Geoph. Res. 66, 259–271.

Kaminski, E., Ribe, N.M., 2001. A kinematic model for recrystallization and texture development in olivine polycrystals. Earth Planet. Sci. Lett. 189, 253–267. http://dx.doi.org/10.1016/S0012-821X(01)00356-9.

Karato, S., 1999. Seismic anisotropy of the Earth's inner core resulting from flow induced Maxwell stresses. Nature 402, 871–873. http://dx.doi.org/10.1038/47235.

Karato, S., Jung, H., Katayama, I., Skemer, P., 2008. Geodynamic significance of seismic anisotropy of the upper mantle: new insights from laboratory studies. Annu. Rev. Earth Planet. Sci. 36, 59–95.

Karki, B., Wentzcovitch, R.M., De Gironcoli, S., Baroni, S., 2000. High pressure lattice dynamics and thermoelasticity of MgO. Phys. Rev. B 61 (13), 8793–8800. http://dx.doi.org/10.1103/PhysRevB.

Kawai, K., Geller, R.R.J., 2010. The vertical flow in the lowermost mantle beneath the Pacific from inversion of seismic waveforms for anisotropic structure. Earth Planet. Sci. Lett. 297 (1–2), 190–198. http://dx.doi.org/10.1016/j.epsl.2010.05.037.

Kawai, K., Tsuchiya, T., 2015. Small shear modulus of cubic CaSiO$_3$ perovskite. Geophys. Res. Lett. 42, 2718–2736. http://dx.doi.org/10.1002/2015GL063442.

Kawazoe, T., Nishiyama, N., Nishihara, Y., Irifune, T., 2010. Deformation experiment at P-T conditions of the mantle transition zone using D-DIA apparatus. Phys. Earth Planet. Inter. 183, 190–195.

Kendall, J., Silver, P., 1996. Constraints from seismic anisotropy on the nature of the lowermost mantle. Nature 381, 409–412. http://dx.doi.org/10.1038/381409a0.

Kendall, J.-M., Silver, P.G., 1998. Investigating causes of D″ anisotropy. In: Gurnis, M., Wysession, M.E., Knittle, E., Buffett, B.A. (Eds.), The core-mantle boundary region, geodynamics series. American Geophysical Union, Washington, pp. 97–118.

Kennett, B.L.N., Widyantoro, S., 1998. Joint seismic tomography for bulk sound and shear wave speed in the Earth's mantle. J. Geophys. Res. 103 (12), 469–493. http://dx.doi.org/10.1029/09JB00150.

Kern, H., Ivankina, T.I., Nikitin, A.N., Lokajicek, T., Pros, Z., 2008. The effect of oriented microcracks and crystallographic and shape preferred orientation on bulk elastic anisotropy of a foliated biotite gneiss from Outokumpu. Tectonophysics 457, 143–149.

Kern, H., Wenk, H.R., 1990. Fabric-related velocity anisotropy and shear wave splitting in rocks from the Santa Rosa mylonite zone, California. J. Geophys. Res. 95 (B7), 11213–11223. http://dx.doi.org/10.1029/JB095iB07p11213.

Kingma, K.J., Cohen, R.E., Hemley, R.J., Mao, H.-k., 1995. Transformation of stishovite to a denser phase at lower-mantle pressures. Nature 374, 243–245. http://dx.doi.org/10.1038/374243a0.

Koci, L., Vitos, L., Ahuja, R., 2007. Ab initio calculations of the elastic properties of ferropericlase Mg1-xKexO (x⁎0.25). Phys. Earth Planet. Inter. 164, 177–185.

Kohlstedt, D.T., Goetze, C., 1974. Low-stress high-temperature creep in olivine single crystals. J. Geophys. Res. 79, 2045–2051.

Komatitsch, D., Vinnik, L.P., Chevrot, S., 2010. SHdiff-SVdiff splitting in an isotropic Earth. J. Geophys. Res. 115, B07312. http://dx.doi.org/10.1029/2009JB006795.

Kraych, A., Carrez, P., Hirel, P., Clouet, E., Cordier, P., 2016. On dislocation glide in MgSiO3 bridgmanite at high-pressure and high-temperature. Earth Planet. Sci. Lett. 452, 60–68. http://dx.doi.org/10.1016/j.epsl.2016.07.035.

Kubin, L.P., Canova, G., Condat, M., Devincre, B., Pontikis, V., Bréchet, Y., 1992. Dislocation microstructures and plastic flow: A 3D simulation. Solid State Phenomena 23–24, 455–472. http://dx.doi.org/10.4028/www.scientific.net/SSP.23-24.455.

Kuwayama, Y., Hirose, K., Sata, N., Ohishi, Y., 2005. The pyrite-type high-pressure form of silica. Science 309, 923–925. http://dx.doi.org/10.1126/science.1114879.

Kustowski, B., Ekström, G., Dziewonski, A., 2008. Anisotropic shear-wave velocity structure of the Earth's mantle: a global model. J. Geophys. Res. 113 (B6), B06306. http://dx.doi.org/10.1029/2007JB005169.

Langdon, T.G., Mohamed, F.A., 1978. A simple method of constructing Ashby-type deformation mechanism maps. J. Mater. Sci. 13, 473–482. http://dx.doi.org/10.1007/BF00544735.

Langrand, C., Hilairet, N., Nisr, C., Roskosz, M., Ribárik, G., Vaughan, G.B.M., Merkel, S., 2017. Reliability of multigrain indexing for orthorhombic polycrystals above 1 Mbar: application to MgSiO$_3$-post-perovskite. J. Appl. Crystallog. 50, 120–130. http://dx.doi.org/10.1107/S1600576716018057.

Lay, T., 2015. Deep earth structure: Lower mantle and D″. In: Romanowicz, B., Dziewonski, A.M. (Eds.), Treatise on Geophysics, Vol. 1.22, pp. 684–723.

Lay, T., Helmberger, D.V., 1983. The shear-wave velocity gradient at the base of the mantle. J. Geophys. Res. 88, 8160–8170. http://dx.doi.org/10.1029/JB088iB10p08160.

Lay, T., Young, C.J., 1991. Analysis of seismic SV waves in the core's penumbra. Geophys. Res. Lett. 18, 1373–1376. http://dx.doi.org/10.1029/91GL01691.

Lay, T., Williams, Q., Garnero, E.J., Kellogg, L., Wysession, M.E., 1998. Seismic wave anisotropy in the D″ region and its implications. In: Gurnis, M., Wysession, M.E., Knittle, E., Buffett, B.A. (Eds.), The core-mantle boundary region, geodynamics series 28. American Geophysical Union, Washington, USA, pp. 299–318.

Lay, T., Garnero, E.J., Williams, Q., 2004. Partial melting in a thermo-chemical boundary layer at the base of the mantle. Phys. Earth Planet. Inter. 146, 441–467. http://dx.doi.org/10.1126/science.1133280.

Lebensohn, R.A., Tomé, C.N., 1993. A self-consistent anisotropic approach for the simulation of plastic deformation and texture development of polycrystals – application to zirconium alloys. Acta Metall. Mater. 41, 2611–2624. http://dx.doi.org/10.1016/0956-7151(93)90130-K.

Lebensohn, R.A., 2001. N-site modeling of a 3D viscoplastic polycrystal using fast fourier transform. Acta Mater. 49, 2723–2737. http://dx.doi.org/10.1016/S1359-6454(01)00172-0.

Lehmann, I., 1936. P', Bureau Central Séismologique International Strasbourg. Publications du Bureau Central Scientifiques A 14 (3), 87–115.

Lekic, V., Cottaar, S., Dziewonski, A., Romanowicz, B., 2012. Cluster analysis of global lower mantle tomography: a new class of structure and implications for chemical heterogeneity. Earth Planet. Sci. Lett. 357, 68–77. http://dx.doi.org/10.1016/j.epsl.2012.09.014.

Levitas, V.I., Ma, Y., Hashemi, J., Holtz, M., Guven, N., 2006. Strain-induced disorder, phase transformations, and transformation-induced plasticity in hexagonal boron nitride under compression and shear in a rotational diamond anvil cell: In situ x-ray diffraction study and modeling. J. Chem. Phys. 125, 044507. http://dx.doi.org/10.1063/1.2208353.

Leykam, D., Tkalčič, H., Reading, A.M., 2010. Core structure re-examined using new teleseismic data recorded in Antarctica: evidence for, at most, weak cylindrical seismic anisotropy in the inner core. Geophys. J. Int. 180 (3), 1329–1343. http://dx.doi.org/10.1111/j.1365-246X.2010.04488.x.

Li, M., McNamara, A.K., Garnero, E.J., 2014. Chemical complexity of hotspots caused by cycling oceanic crust through mantle reservoirs. Nature Geosci. 7, 366–370. http://dx.doi.org/10.1038/ngeo2120.

Li, J., Struzhkin, V.V., Mao, H.-K., Shu, J., Hemley, R.J., Fei, Y., Mysen, B., Dera, P., Prakapenka, V., Shen, G., 2004. Electronic spin state of iron in lower mantle perovskite. Proc. Nat. Acad. Sci. 101, 14027–14030. 10.1073 pnas.0405804101.

Li, X.-D., Romanowicz, B., 1995. Comparison of global waveform inversions with and without considering cross-branch modal coupling. Geophys. J. Int. 121 (3), 695–709. 10.1111/j.1365-246X.1995.tb06432.x..

Li, Y., Deschamps, F., Tackley, P.J., 2014. Effects of low-viscosity post-perovskite on the stability and structure of primitive reservoirs in the lower mantle. Geophys. Res. Lett. 41. http://dx.doi.org/10.1002/2014GL061362.

Liermann, H.-P., Merkel, S., Miyagi, L., Wenk, H.-R., Shen, G., Cynn, H., Evans, W.J., 2009. Experimental method for *in situ* determination of material textures at simultaneous high-pressure and high temperature by means of radial diffraction in the diamond anvil cell. Rev. Scient. Instrum. 80 (104501), 1–8. http://dx.doi.org/10.1063/1.3236365.

Lin, J.-F., Watson, H., Vanko, G., Alp, E.E., Prakapenka, V.B., Dera, P., Struzhkin, V., Kubo, A., Zhao, J., McCammon, C., Evans, W.J., 2008. Intermediate-spin ferrous iron in lowermost mantle post-perovskite and perovskite. Nature Geosci. 1, 688–691. http://dx.doi.org/10.1038/ngeo310.

Lin, J.-F., Wenk, H.-R., Voltolini, M., Speziale, S., Shu, J., Duffy, T., 2009. Deformation of lower mantle ferropericlase (Mg, Fe)O across the electronic spin transition. Phys. Chem. Mineral. 36, 585–592. http://dx.doi.org/10.1007/s00269-009-0303-5.

Lin, J.-F., Alp, E.E., Mao, Z., Inoue, T., McCammon, C., Xia, Y.M., Chow, P., Zhao, J.Y., 2012. Electronic spin states of ferric and ferrous iron in the lower-mantle silicate perovskite. Amer. Mineral. 97, 592–597. http://dx.doi.org/10.2138/am.2012.4000.

Linckens, J., Herwegh, M., Müntener, O., Mercolli, I., 2011. Evolution of a polymineralic mantle shear zone and the role of second phases in the localization of deformation. J. Geophys. Res. 116, B06210. http://dx.doi.org/10.1029/2010JB008119.

Lincot, A., Merkel, S., Cardin, P., 2015. Is inner core seismic anisotropy a marker for plastic flow of cubic iron? Geophys. Res. Lett. 42, 1326–1333. http://dx.doi.org/10.1002/2014GL062862.

Lincot, A., Merkel, S., Deguen, P., Cardin, P., 2016. Multiscale model of global inner-core anisotropy induced by hcp alloy plasticity. Geophys. Res. Lett. 43, 1084–1091. http://dx.doi.org/10.1002/2015GL067019.

Liu, L.-G., 1974. Silicate perovskite from phase transformations of pyrope-garnet at high pressure and temperature. Geophys. Res. Lett. 1, 277–280. http://dx.doi.org/10.1029/GL001i006p00277.

Long, M.D., 2009. Complex anisotropy in D″ beneath the eastern Pacific from SKS–SKKS splitting discrepancies. Earth Planet. Sci. Lett. 283, 181–189. http://dx.doi.org/10.1016/j.epsl.2009.04.019.

Long, M.D., 2013. Constraints on subduction geodynamics from seismic anisotropy. Rev. Geophys. 51, 76–112. http://dx.doi.org/10.1002/rog.20008.

Long, M.D., Silver, P.G., 2009. Shear wave splitting and mantle anisotropy: measurements, interpretations, and new directions. Surv. Geophys. 30, 407–461. http://dx.doi.org/10.1007/s10712-009-9075-1.

Long, M.D., Becker, T.W., 2010. Mantle dynamics and seismic anisotropy. Earth Planet. Sci. Lett. 297, 341–354. http://dx.doi.org/10.1016/j.epsl.2010.06.036.

Long, M.D., Lynner, C., 2015. Seismic anisotropy in the lowermost mantle near the Perm Anomaly. Geophys. Res. Lett. 42, 7073–7080. http://dx.doi.org/10.1002/2015GL065506.

Long, M.D., Xiao, X., Jiang, Z., Evans, B., Karato, S., 2006. Lattice preferred orientation in deformed polycrystalline (Mg, Fe)O and implications for seismic anisotropy in D″. Phys. Earth Planet. Inter. 156 (1–2), 75–88. http://dx.doi.org/10.1016/j.pepi.2006.02.006.

Lutterotti, L., Vasin, R., Wenk, H.-R., 2014. Rietveld texture analysis from synchrotron diffraction images: I. Basic analysis. Powder Diffraction 29, 76–84. http://dx.doi.org/10.1007/s00269-011-0439-y.

Lynner, C., Long, M.D., 2012. Evaluating contributions to SK(K)S splitting from lower mantle anisotropy: a case study from station DBIC, Côte D'Ivoire. Bull. Seismol. Soc. Am. 102, 1030–1040. http://dx.doi.org/10.1785/-12-11-0255.

Lynner, C., Long, M.D., 2014. Lowermost mantle anisotropy and deformation along the boundary of the African LLSVP. Geophys. Res. Lett. 41, 3447–3454. http://dx.doi.org/10.1002/2014GL059875.

Lythgoe, K.H., Deuss, A., Rudge, J.F., Neufeld, J.A., 2014. Earth's inner core: Innermost inner core or hemispherical variations? Earth Planet. Sci. Lett. 385, 181–189. http://dx.doi.org/10.1016/j.epsl.2013.10.049.

Mainprice, D., Tommasi, A., Ferré, D., Carrez, P., Cordier, P., 2008. Predicted glide systems and crystal preferred orientations of polycrystalline silicate Mg-perovskite at high pressure: Implications for the seismic anisotropy in the lower mantle. Earth Planet. Sci. Lett. 271, 135–144. http://dx.doi.org/10.1016/j.epsl.2008.03.058.

Mao, H.K., Bassett, W.A., Takahashi, T., 1967. Effect of pressure on crystal structure and lattice parameters of iron up to 300 kbars. J. Appl. Phys. 38, 272–276.

Marquardt, H., Miyagi, L., 2015. Slab stagnation in the shallow lower mantle linked to an increase in mantle viscosity. Nature Geosci. 8, 311–314. http://dx.doi.org/10.1038/ngeo2393.

Masters, G., Laske, G., Bolton, H., Dziewonski, A., 2000. The relative behavior of shear velocity, bulk sound speed, and compressional velocity in the mantle: implications for chemical and thermal structure. In: Karato, S.-I. (Ed.), Earth's Deep Interior: Minreal Physics and Tomography from the atomic to the global scale. American Geophysical Union, Washington, DC, pp. 63–88. http://dx.doi.org/10.1029/GM117p0063.

Martorell, B., Vocadlo, L., Brodholdt, J., Wood, I.G., 2013. Strong premelting effect in the elastic properties of hcp-Fe under inner core conditions. Science 342, 466–468. http://dx.doi.org/10.1126/science.1243651.

Mattesini, M., Belonoshko, A.B., Buforn, E., Ramirez, M., Simak, S.I., Udias, A., Mao, H.-K., Ahuja, R., 2010. Hemispherical anisotropic patterns of the Earth's inner core. Proc. Nat. Acad. Sci. 107, 9507–9512.

Matthies, S., 2012. GEO-MIX-SELF calculations of the elastic properties of a textured graphite sample at different hydrostatic pressures. J. Appl. Crystallog. 45 (1), 1–16. http://dx.doi.org/10.1107/S002188981104338X.

Matthies, S., Humbert, M., 1995. On the principle of a geometric mean of even-rank symmetric tensors for textured polycrystals. J. Appl. Crystallog. 28 (3), 254–266. http://dx.doi.org/10.1107/S0021889894009623.

Matzel, E., Sen, M.K., Grand, S.P., 1996. Evidence for anisotropy in the deep mantle beneath Alaska. Geophys. Res. Lett. 23, 2417–2420. http://dx.doi.org/10.1029/96GL02186.

Maupin, V., 1994. On the possibility of anisotropy in the D″ layer as inferred from the polarization of diffracted S waves. Phys. Earth Planet. Inter. 87 (1–2), 1–32. http://dx.doi.org/10.1016/0031-9201(94)90019-1.

Maupin, V., Garnero, E.J., Lay, T., Fouch, M.J., 2005. Azimuthal anisotropy in the D″ layer beneath the Caribbean. J. Geophys. Res. 110, B08301. http://dx.doi.org/10.1029/2004JB003506.

McCammon, C., 1997. Perovskite as a possible sink for ferric iron in the lower mantle. Nature 387, 694–696.

McKenzie, D.P., 1969. Speculations on the consequences and causes of plate motions. Geophys. J. R.. Astron. Soc. 18, 1–32.

McNamara, A., van Keken, P., Karato, S., 2002. Development of anisotropic structure in the Earth's lower mantle by solid-state convection. Nature 416 (6678), 310–314. http://dx.doi.org/10.1038/416310a.

McNamara, A., van Keken, P., Karato, S., 2003. Development of finite strain in the convecting lower mantle and its implications for seismic anisotropy. J. Geophys. Res. 108 (B5), 2230. http://dx.doi.org/10.1029/2002JB001970.].

Meade, C., Silver, P.G., Kaneshima, S., 1995. Laboratory and seismological observations of lower mantle isotropy. Geophys. Res. Lett. 22, 1293–1296. http://dx.doi.org/10.1029/95GL01091.

Mégnin, C., Romanowicz, B., 2000. The three-dimensional shear velocity structure of the mantle from the inversion of body, surface and higher-mode waveforms. Geophys. J. Int. 143 (3), 709–728. http://dx.doi.org/10.1046/j.1365-246X.2000.00298.x.

Merkel, S., Wenk, H.-R., Shu, J., Shen, G., Gillet, P., Mao, H.-K., Hemley, R.J., 2002. Deformation of polycrystalline MgO at pressures of the lower mantle. J. Geophys. Res. 107 (B11), 2271. http://dx.doi.org/10.1029/2001JB000920.

Merkel, S., Wenk, H.-R., Badro, J., Montagnac, J., Gillet, P., Mao, H.k., Hemley, R.J., 2003. Deformation of (Mg0.9, Fe0.1)SiO$_3$ perovskite aggregates up to 32 GPa. Earth Planet. Sci. Lett. 209, 351–360. http://dx.doi.org/10.1016/S0012-821X(03)00098-0.

Merkel, S., Wenk, H.-R., Gillet, P., Mao, H.-K., Hemley, R.J., 2004. Deformation of polycrystalline iron up to 30 GPa and 1000 K. Phys. Earth Planet. Inter. 145, 239–251. http://dx.doi.org/10.1016/j.pepi.2004.04.001.

Merkel, S., Kubo, A., Miyagi, L., Speziale, S., Duffy, T.S., Mao, H.-K., Wenk, H.-R., 2006. Plastic deformation of MgGeO$_3$ post-perovskite at lower mantle pressures. Science 311, 644–646. http://dx.doi.org/10.1126/science.1121808.

Merkel, S., McNamara, A.K., Kubo, A., Speziale, S., Miyagi, L., Meng, Y., Duffy, T.S., Wenk, H.-R., 2007. Deformation of (Mg, Fe)SiO3 post-perovskite and D″ anisotropy. Science 316, 1729–1732. http://dx.doi.org/10.1126/science.1140609.

Merkel, S., Liermann, H.P., Miyagi, L., Wenk, H.-R., 2013. In-situ radial X-ray diffraction study of texture and stress during phase transformations in bcc-, fcc-, and hcp-iron up to 36 GPa and 1000K. Acta Mater. 61, 5144–5151. http://dx.doi.org/10.1016/j.actamat.2013.04.068.

Mika, D.P., Dawson, P.R., 1999. Polycrystal plasticity modeling of intracrystalline boundary textures. Acta Mater. 47 (4), 1355–1369. http://dx.doi.org/10.1016/S1359-6454(98)00386-3.

Mitrovica, J.X., Forte, A.M., 2004. A new inference of mantle viscosity based upon joint inversion of convection and glacial isostatic adjustment data, Earth Planet. Sci. Lett. 225, 177–189.

von Mises, R., 1928. Mechanik der plastischen Formänderung von Kristallen. Z. Angew. Math. Mech. 8, 161–185.

Mitchell, B.J., Helmberger, D.V., 1973. Shear velocities at the base of the mantle from observations of S and ScS. J. Geophys. Res. 78, 6009–6020. http://dx.doi.org/10.1029/JB078i026p06009.

Miyagi, L., Merkel, S., Yagi, T., Sata, N., Ohishi, Y., Wenk, H.-R., 2006. Quantitative Rietveld texture analysis of CaSiO$_3$ perovskite deformed in a diamond anvil cell. J. Phys. Cond. Matter 18, S995–S1005. http://dx.doi.org/10.1088/0953-8984/18/25/S07.

Miyagi, L., Merkel, S., Yagi, T., Oshishi, Y., Wenk, H.-R., 2009. Diamond anvil cell deformation of CaSiO$_3$ perovskite up to 49 GPa. Phys. Earth Planet. Inter. 174, 159–164. http://dx.doi.org/10.1016/j.pepi.2008.05.018.

Miyagi, L., Wenk, H.-R., 2016. Texture development and slip systems in bridgmanite and bridgmanite + ferropericlase aggregates. Phys. Chem. Minerals 43, 597–613. http://dx.doi.org/10.1007/s00269-016-0820-y.

Miyagi, L., Kunz, M., Nasiatka, J., Voltolini, M., Knight, J., Wenk, H.-R., 2008. *In-situ* study of texture development in polycrystalline iron during phase transformations and deformation at high pressure and temperature. J. Appl. Phys. 104, 103510. http://dx.doi.org/10.1063/1.3008035.

Miyagi, L., Kanitpanyacharoen, W., Kaercher, P., Lee, K.K.M., Wenk, H.R., 2010. Slip systems in MgSiO$_3$ post-perovskite: Implications for D″ anisotropy. Science 329, 1639–1641. http://dx.doi.org/10.1126/science.1192465.

Miyagi, L., Kanitpanyacharoen, W., Stackhouse, S., Militzer, B., Wenk, H.-R., 2011. The enigma of post-perovskite anisotropy: deformation versus transformation textures. Phys. Chem. Minerals 38, 665–678. http://dx.doi.org/10.1007/s00269-011-0439-y.

Miyagi, L., Kanitpanyacharoen, W., Raju, V., Kaercher, P., Knight, J., McDowell, A., Wenk, H.R., Williams, Q., Zepeda, E., 2013. Combined resistive and laser heating technique for in situ radial X-ray diffraction in the diamond anvil cell experiments at high pressure and temperature. Rev. Sci. Instr. 84 (025118), 1–9. http://dx.doi.org/10.1063/1.4793398.

Miyajima, N., Yagi, T., Ichihara, M., 2009. Dislocation microstructures of MgSiO$_3$ perovskite at a high pressure and temperature condition. Phys. Earth Planet. Inter. 174, 153–158. http://dx.doi.org/10.1016/j.pepi.2008.04.004.

Molinari, A., Canova, G.R., Ahzi, S., 1987. A self-consistent approach of the large deformation polycrystal viscoplasticity. Acta Metall. 35, 2983–2994.

Montagner, J.P., 2002. Upper mantle low anisotropy channels below the Pacific plate. Earth Planet. Sci. Lett. 202, 263–274.

Montagner, J.P., Anderson, D.L., 1989. Petrological constraints on seismic anisotropy. Phys. Earth Planet. Inter. 54, 82–105.

Montagner, J.P., Tanimoto, T., 1990. Global anisotropy in the upper mantle inferred from the regionalization of phase velocities. J. Geophys. Res. 95, 4797–4819. http://dx.doi.org/10.1029/JB095iB04p04797.

Montagner, J.P., Tanimoto, T., 1991. Global upper mantle tomography of seismic velocities and anisotropies. J. Geophys. Res. 96, 20337–20351. http://dx.doi.org/10.1029/91JB01890.

Montagner, J.-P., Kennett, B.L.N., 1996. How to reconcile body-wave and normal-mode reference Earth models. Geophys. J. Int. 125, 229–248. 10.1111/j.1365-246X.1996.tb06548.x.

Monteiller, V., Chevrot, S., 2010. How to make robust splitting measurements for single-station analysis and three-dimensional imaging of seismic anisotropy. Geophys. J. Int. 182. http://dx.doi.org/10.1111/j.1365246X.2010.04608.

Morelli, A., Dziewonski, A.M., Woodhouse, J.H., 1986. Anisotropy of the inner core inferred from PKIKP travel times. Geophys. Res. Lett. 13, 1545–1548. http://dx.doi.org/10.1029/GL013i013p01545.

Morris, G.B., Raitt, R.W., Shor, G.G., 1969. Velocity anisotropy and delay-time maps of the mantle near Hawaii. J. Geophys. Res. 17, 4300–4316.

Moulik, P., Ekström, G., 2014. An anisotropic shear velocity model of the Earth's mantle using normal modes, body waves, surface waves, and long-period waveforms. Geophys. J. Int. 199, 1713–1738. http://dx.doi.org/10.1029/JB078i026p06009.

Murakami, M., Hirose, K., Kawamura, K., Sata, N., Ohishi, Y., 2004. Post-perovskite phase transition in MgSiO$_3$. Science 304, 855–858. http://dx.doi.org/10.1126/science.1095932.

Nataf, H.C., Nakanishi, I., Anderson, D.L., 1984. Anisotropy and shear velocities in the upper mantle. Geophys. Res. Lett. 11, 109–112. http://dx.doi.org/10.1029/GL011i002p00109.

Naumann, C.F., 1850. Lehrbuch der Geognosie. Engelmann, Leipzig.

Nisr, C., Ribarik, G., Ungar, T., Vaughan, G.B.M., Cordier, P., Merkel, S., 2012. High resolution three-dimensional X-ray diffraction study of dislocations in grains of post-perovskite at 90 GPa. J. Geophys. Res. 117, B03201. http://dx.doi.org/10.1029/2011JB008401.

Niu, F., Wen, L., 2002. Seismic anisotropy in the top 400 km of the inner core beneath the "eastern" hemisphere. Geophys. Res. Lett. 29 (12), 1611. 15-1-53-5 [doi:10.1029/2001GL014118].

Niu, F., Perez, A.M., 2004. Seismic anisotropy in the lower mantle: a comparison of waveform splitting of SKS and SKKS. Geophys. Res. Lett. 31, L24612. http://dx.doi.org/10.1029/2004GL021196.

Nobre Silva, I.G., Weis, D., Scoates, J.S., 2013. Isotopic systematics of the early Mauna Kea shield phase and insight into the deep mantle beneath the Pacific Ocean. Geochem. Geophys. Geosyst. 14 (3), 659–676. http://dx.doi.org/10.1002/ggge.20047.

Nowacki, A., Wookey, J., 2016. The limits of ray theory when measuring shear wave splitting in the lowermost mantle with ScS waves. Geophys. J. Int. 207 (3), 1573–1583. http://dx.doi.org/10.1093/gji/ggw358.

Nowacki, A., Wookey, J., Kendall, J.-M., 2010. Deformation of the lowermost mantle from seismic anisotropy. Nature 467, 1091–1094. http://dx.doi.org/10.1038/nature09507.

Nowacki, A., Wookey, J., Kendall, J.-M., 2011. New advances in using seismic anisotropy, mineral physics and geodynamics to understand deformation in the lowermost mantle. J. Geodyn. 52, 205–228. http://dx.doi.org/10.1016/j.jog.2011.04.003.

Nowacki, A., Walker, A., Wookey, J., Kendall, J., 2013. Evaluating post-perovskite as a cause of D″ anisotropy in regions of palaeosubduction. Geophys. J. Int. 192 (3), 1085–1090. http://dx.doi.org/10.1093/gji/ggs068.

Oganov, A., Ono, S., 2004. Theoretical and experimental evidence for a post-perovskite phase of $MgSiO_3$ in Earth's D″ layer. Nature 430 (6998), 445–448. http://dx.doi.org/10.1038/nature02701.

Ohtami, E., Sakai, T., 2008. Recent advances in the study of mantle phase transitions. Phys. Earth Planet. Inter. 170, 240–247. http://dx.doi.org/10.1016/j.pepi.2008.07.024.

Oldham, R.D., 1906. The constitution of the interior of the Earth, as revealed by earthquakes. Quart. J. Geol. Soc. 62 (1–4), 456–475.

Onodera, A., 1987. Octahedral-anvil high-pressure devices. High Temperature-High Pressure 19, 579–609.

Oreshin, S., Vinnik, L., 2004. Heterogeneity and anisotropy of seismic attenuation in the inner core. Geophys. Res. Lett. 31, L02613. http://dx.doi.org/10.1029/2003GL018591.

Pamato, M.G., Myhill, R., Boffa Balaran, T., Frost, D.J., Heidelbach, F., Miyajima, N., 2014. Lower-mantle water reservoir implied by the extreme stability of a hydrous aluminosilicate. Nature Geosci. 8, 75–79. http://dx.doi.org/10.1038/ngeo2306.

Panning, M.P., Romanowicz, B., 2004. Inferences on flow at the base of Earth's mantle based on seismic anisotropy. Science 303, 351–353. http://dx.doi.org/10.1126/science.1091524.

Panning, M.P., Romanowicz, B., 2006. A three-dimensional radially anisotropic model of shear velocity in the whole mantle. Geophys. J. Int. 167, 361–379. http://dx.doi.org/10.1111/j.1365-246X.2006.03100.x.

Panning, M.P., Lekic, V., Romanowicz, B.A., 2010. Importance of crustal corrections in the development of a new global model of radial anisotropy. J. Geophys. Res. 115, B12325. http://dx.doi.org/10.1029/2010JB007520.

Paterson, M.S., 1973. Nonhydrostatic thermodynamics and its geologic applications. Rev. Geophys. 11, 355–389.

Paterson, M.S., Olgaard, D.L., 2000. Rock deformation tests to large shear strains in torsion. J. Struct. Geol. 22 (8), 1341–1358. http://dx.doi.org/10.1016/S0191-8141(00)00042-0.

Petrova, A.E., Krasnorussky, V.N., Stishov, S.M., 2010. Elastic properties of FeSi. J. Exp. Theor. Physics 111, 427–430.

Pfaff, F., 1859. Versuche über den Einfluss des Drucks auf die optischen Eigenschaften doppeltbrechender Krystalle. Ann. Phys. 107, 333–338.

Ping, Y., Coppari, F., Hicks, D.G., Yaakobi, B., Fratanduono, D.E., Hamel, S., Eggert, J.H., Rygg, J.R., Smith, R.F., Swift, D.C., Braun, D.G., Boehly, T.R., Collins, G.W., 2013. Solid iron compressed up to 560GPa. Phys. Rev. Lett. 111 (6), 065501. http://dx.doi.org/10.1103/PhysRevLett. 111.065501.

Polanyi, M., 1934. Lattice distortion which originates plastic flow. Z. Phys. 89, 660.

Prakapenka, V.B., Kubo, A., Kuznetsov, A., Laskin, A., Shkurikhin, O., Dera, P., Rivers, M.L., Sutton, S.R., 2008. Advanced flat top laser heating system for high pressure research at GSECARS: application to the melting behavior of germanium. High Pressure Research 28 (3), 225–235. http://dx.doi.org/10.1080/08957950802050718.

Pulliam, J., Sen, M., 1998. Seismic anisotropy in the core–mantle transition zone. Geophys. J. Int. 135, 113–128. http://dx.doi.org/10.1046/j.1365-246X.1998.00612.x.

Raitt, R.W., 1963. Marine physics laboratory. Scripps Inst. Oceanography, Univ. Calif. San Diego. MPL-U-23/63.

Raleigh, C.B., 1968. Mechanisms of plastic deformation in olivine. J. Geophys. Res. 73, 5391–5406.

Restivo, A., Helffrich, G., 2006. Core-mantle boundary structure investigated using SKS and SKKS polarization anomalies. Geophys. J. Int. 165, 288–302.

Reuss, A., 1929. Berechnung der Fließgrenze von Mischkristallen auf Grund der Plastizitätsbedingung für Einkristalle. Z. Angew. Math. Mech. 9, 49–58.

Ringwood, A.E., 1962. Mineralogical constitution of the deep mantle. J. Geophys. Res. 67, 4005–4010.

Ringwood, A.E., 1975. Composition and Petrology of the Earth's Mantle. McGraw-Hill, New York. 618 pp.

Ritsema, J., Lay, T., Garnero, E.J., Benz, H., 1998. Seismic anisotropy in the lowermost mantle beneath the Pacific. Geophys. Res. Lett. 25, 1229–1232. http://dx.doi.org/10.1029/98GL00913.

Ritsema, J., 2000. Evidence for shear wave anisotropy in the lowermost mantle beneath the Indian Ocean. Geophys. Res. Lett. 27, 1041–1044. http://dx.doi.org/10.1029/1999GL011037.

Rokosky, J.M., Lay, T., Garnero, E.J., Russell, S., 2004. High-resolution investigation of shear wave anisotropy in D″ beneath the Cocos Plate. Geophys. Res. Lett. 31, L0760. http://dx.doi.org/10.1029/2003GL018902.

Rokosky, J.M., Lay, T., Garnero, E.J., 2006. Small-scale lateral variations in azimuthally anisotropic D structure beneath the Cocos Plate. Earth Planet. Sci. Lett. 248 (1–2), 411–425. http://dx.doi.org/10.1016/j.epsl.2006.06.005.

Romanowicz, B., Bréger, L., 2000. Anomalous splitting of free oscillations: a re-evaluation of possible interpretations. J. Geophys. Res. 105 (B9), 21559–21578. http://dx.doi.org/10.1029/2000JB900144.

Romanowicz, B., Li, X.-D., Durek, J., 1996. Anisotropy in the inner core: could it be due to low-order convection? Science 274 (5289), 963–966. http://dx.doi.org/10.1126/science.274.5295.1988f.

Romanowicz, B., Tkalcic, H., Bréger, L., 2003. On the origin of complexity in PKP travel time data. . 1st ed.. In: Dehant, V. et al (Eds.), Earth's Core: Dynamics, Structure, Rotation 1st ed., vol. 31 AGU, Washington, DC, pp. 31–44.

Romanowicz, B., Cao, A., Godwal, B., Wenk, R., Ventosa, S., Jeanloz, R., 2016. Seismic anisotropy in the Earth's innermost inner core: testing structural models against mineral physics predictions. Geophys. Res. Lett. 43, 93–100. http://dx.doi.org/10.1002/2015GL066734.

Rosa, A.D., Hilairet, N., Ghosh, S., Garbarino, G., Jacobs, J., Perrillat, J.-P., Vaughan, G., Merkel, S., 2015. In situ monitoring of phase transformation microstructures at Earth's mantle pressure and temperature using multi-grain XRD. J. Appl. Crystallog. 48, 1346–1354. http://dx.doi.org/10.1107/S1600576715012765.

Rozel, A., Ricard, Y., Bercovici, D., 2011. A thermodynamically self-consistent damage equation for grain size evolution during dynamic recrystallization. Geophys. J. Int. 184 (2), 719–728.

Rudolph, M.L., Lekic, V.L., Lithgow-Bertelloni, C., 2015. Viscosity jump in Earth's mid-mantle. Science 350, 1349–1352. http://dx.doi.org/10.1126/science.aad1929.

Rudzki, M.P., 1897. Ueber die Gestalt elastischer Wellen in Gesteinen. Bull. Acad. Sci. Cracow, 387–393.

Rudzki, M.P., 1911. Parametrische Darstellung der elastischen Welle in anisotropen Medien. Bull. Acad. Sci. Cracow (A), 503–536.

Russell, S.A., Lay, T., Garnero, E.J., 1998. Seismic evidence for small-scale dynamics in the lowermost mantle at the root of the Hawaiian hotspot. Nature 396, 255–258. http://dx.doi.org/10.1038/24364.

Russell, S.A., Lay, T., Garnero, E.J., 1999. Small-scale lateral shear velocity and anisotropy heterogeneity near the core-mantle boundary beneath the central Pacific imaged using broadband ScS waves. J. Geophys. Res. 104 (B6), 13183–13199. http://dx.doi.org/10.1029/1999JB900114.

Sachs, G., 1928. Zur Ableitung einer Fliessbedingung. Z. Ver. Dtsch. Ing. 72, 734–736.

Saha, S., Bengtson, A., Crispin, K., Morgan, D., 2011. Effects of spin transition on diffusion of Fe^{2+} in ferropericlase in Earth's lower mantle. Phys. Rev. B 84, 184102. http://dx.doi.org/10.1103/PhysRevB.84.184102.

Sakai, T., Ohtani, E., Hiro, N., Ohishi, Y., 2011. Stability field of the hcp-structure for Fe, Fe-Ni and Fe-Ni-Si alloys up to 3 Mbar. Geophys. Res. Lett. 38, L09302. http://dx.doi.org/10.1029/2011GL047178.

Sayers, C.M., 1994. The elastic anisotropy of shales. J. Geophys. Res. 99, 767–774. http://dx.doi.org/10.1029/93JB02579.

Schmandt, B., Jacobson, S.D., Becker, T.W., Liu, Z., Duecker, K.G., 2014. Dehydration melting at the top of the lower mantle. Science 344, 1265–1268. http://dx.doi.org/10.1126/science1253358.

Schmid, E., 1924. Zn-normal stress law. Proc. Int. Congr. Appl. Mech. (Delft), p. 342.

Shi, C.Y., Zhang, L., Yang, W., Liu, Y., Wang, J., Meng, Y., Andrews, J.C., Mao, W.L., 2013. Formation of an interconnected network of iron melt at Earth's lower mantle conditions. Nature Geosci. 6, 971–975. http://dx.doi.org/10.1038/ngeo1956.

Shieh, S.R., Duffy, T.S., Shen, G., 2004. Elasticity and strength of calcium silicate perovskite at lower mantle pressures. Phys. Earth Planet. Int. 143–144, 93–105. http://dx.doi.org/10.1016/j.pepi2003.10.006.

Shim, S.H., Jeanloz, R., Duffy, T.S., 2002. Tetragonal structure of $CaSiO_3$ perovskite above 20 GPa. Geophys. Res. Lett. 29 (24), 2166. http://dx.doi.org/10.1029/2002GL016148.

Shimizu, I., 1999. A stochastic model of grain size distribution during dynamic recrystallization. Philos. Mag. A 79, 1217–1231.

Shimizu, I., 2008. Theories and applicability of grain size piezometers: The role of dynamic recrystallization mechanisms. J. Struct. Geol. 30, 899–917. 10.1016/j.jsg.2008.03.004.

Simmons, N.A., Forte, A.M., Grand, S.P., 2009. Joint seismic, geodynamic and mineral physical constraints on three-dimensional mantle heterogeneity: implications for the relative importance of thermal versus compositional heterogeneity. Geophys. J. Int. 177, 1284–1304. http://dx.doi.org/10.1111/j.1365-246X.2009.04133.x.

Simmons, N.A., Myers, S.C., Johannesson, G., Matzel, E., 2012. LLNL-G3Dv3: global P wave tomography model for improved regional and teleseismic travel time prediction. J. Geophys. Res. 117, B10302. http://dx.doi.org/10.1029/2012JB009525.

Soderlund, K.M., King, E.M., Aurnou, J.M., 2012. The influence of magnetic fields in planetary dynamo models. Earth Planet. Sci. Lett. 333–334, 9–20. http://dx.doi.org/10.1016/j.epsl.2012.03.038.

Souriau, A., 2015. Deep earth structure: the Earth's cores. In: Romanowicz, B., Dziewonski, A.M. (Eds.), Treatise on Geophysics, Vol. 1, pp. 656–693. chap 1.19.

Souriau, A., Romanowicz, B., 1996. Anisotropy in inner core attenuation: A new type of data to constrain the nature of the solid core. Geophys. Res. Lett. 23, 1–4. http://dx.doi.org/10.1029/95GL03583.

Souriau, A., Romanowicz, B., 1997. Anisotropy in the inner core: relation between P-velocity and attenuation. Phys. Earth Planet. Inter. 101, 33–47. http://dx.doi.org/10.1016/S0031-9201(96)03242-6.

Souriau, A., Teste, A., Chevrot, S., 2003. Is there structure inside the liquid outer core? Geophys. Res. Lett. 30 (11), 1567. http://dx.doi.org/10.1029/2003GL017008.

Speziale, S., Marquardt, H., Duffy, T.S., 2014. Brillouin scattering and its application in geosciences. Rev. Mineral. Geochem. 78, 543–603.

Stackhouse, S., Brodholt, J.P., Wookey, J., Kendall, J.-M., Price, G.D., 2005. The effect of temperature on the seismic anisotropy of the perovskite and post-perovskite polymorphs of $MgSiO_3$. Earth Planet. Sci. Lett. 230 (1–2), 1–10. http://dx.doi.org/10.1016/j.epsl.2004.11.021.

Stevenson, D.J., 1987. Limits on lateral density and velocity variations in the Earth's outer core. Geophys. J. R. Astron. Soc. 88 (1), 311–319. http://dx.doi.org/10.1111/j.1365-246X.1987.tb01383.x.

Stretton, I., Heidelbach, F., Mackwell, S., Langenhorst, F., 2001. Dislocation creep of magnesiowuestite ($Mg_{0.8}Fe_{0.2}O$). Earth Planet. Sci. Lett. 194, 229–240. http://dx.doi.org/10.1016/S0012-821X(01)00533-7.

Su, W.-J., Dziewonski, A.M., 1997. Simultaneous inversion for 3-D variations in shear and bulk velocity in the mantle. Phys. Earth Planet. Inter. 100, 135–156. http://dx.doi.org/10.1016/S0031-9201(96)03236-0.

Sumita, I., Bergman, M.I., 2015. Inner-core dynamics. In: Treatise on Geophysics, vol. 8 (chap 8.10).

Sun, X.L., Song, X.D., 2008a. Tomographic inversion for three-dimensional anisotropy of Earth's inner core. Phys. Earth Planet. Inter. 167, 53–68. http://dx.doi.org/10.1016/j.pepi.2008.02.011.

Sun, X.L., Song, X.D., 2008b. The inner inner core of the Earth: texturing of iron crystals from three dimensional seismic anisotropy. Earth Planet. Sci. Lett. 269, 56–65. http://dx.doi.org/10.1016/j.epsl.2008.01.049.

Sun, X.Y., Cordier, P., Taupin, V., Fressengeas, C., Jahn, S., 2016. Continuous description of a grain boundary in forsterite from atomic scale simulations: the role of disclinations. Phil. Mag. 96, 1757–1772. http://dx.doi.org/10.1080/14786435.2016.1177232.

Tackley, P.J., 1993. Effects of strongly temperature-dependent viscosity on time-dependent, three-dimensional models of mantle convection. Geophys. Res. Lett. 20, 2187–2190. http://dx.doi.org/10.1029/93GL02317.

Tanaka, S., Hamaguchi, H., 1997. Degree one heterogeneity and hemispherical variation of anisotropy in the inner core from PKP(BC)-PKP(DF) times. J. Geophys. Res. 102, 2925–2938. http://dx.doi.org/10.1029/96JB03187.

Tanimoto, T., Anderson, D.L., 1984. Mapping convection in the mantle. Geophys. Res. Lett. 11 (4), 287–290. http://dx.doi.org/10.1029/GL011i004p00287.

Tanimoto, T., Anderson, D.L., 1985. Lateral heterogeneity and azimuthal anisotropy of the upper mantle: Love and Rayleigh Waves 100–250s. J. Geophys. Res. 90, 1842–1858. http://dx.doi.org/10.1029/JB090iB02p01842.

Tamura, N., 2014. XMAS: a versatile tool for analyzing synchrotron X-ray microdiffraction data. In: Ice, G.E., Barabash, R. (Eds.), Strain and Dislocation Gradients from Diffraction. London Imperial College Press, pp. 125–155. http://dx.doi.org/10.1142/9781908979636_fmatter.

Tateno, S., Hirose, K., Sata, N., Ohishi, Y., 2009. Determination of post-perovskite phase transition boundary up to 4400 K and implications for the thermal structure of D″ layer. Earth Planet. Sci. Lett. 277, 130–136. http://dx.doi.org/10.1016/j.epsl.2008.10.004.

Tateno, S., Hirose, K., Ohishi, Y., Tatsumi, Y., 2010. The structure of iron in Earth's inner core. Science 330, 359–361. http://dx.doi.org/10.1126/science.1194662.

Tateno, S., Hirose, K., Komabayashi, T., Ozawa, H., Ohishi, Y., 2012. The structure of Fe-Ni alloy in Earth's inner core. Geophys. Res. Lett. 39 (L12305), 1–4. http://dx.doi.org/10.1029/2012GL052103.

Tateno, S., Kuwayama, Y., Hirose, K., Ohishi, Y., 2015. The structure of Fe–Si alloy in Earth's inner core. Earth Planet. Sci. Lett. 418, 11–19. http://dx.doi.org/10.1016/j.epsl.2015.02.008.

Taylor, G.I., 1934. The mechanism of plastic deformation of crystals. Proc. R. Soc. London 145, 362–404.

Taylor, G.I., 1938. Plastic strain in metals. J. Inst. Metals 62, 307–324.

Thomas, C., Kendall, J.M., 2002. The lowermost mantle beneath northern Asia: (2) Evidence for D″ anisotropy. Geophys. J. Int. 151, 296–308. http://dx.doi.org/10.1046/j.1365-246X.2002.01760.x.

Thomas, C., Wookey, J., Simpson, M., 2007. D″ anisotropy beneath Southeast Asia. Geophys. Res. Lett 34 (4), L04301. http://dx.doi.org/10.1029/2006GL028965.

Thomas, C., Wookey, J., Brodholt, J., Fieseler, T., 2011. Anisotropy as cause for polarity reversals of D″ reflections. Earth Planet. Sci. Lett. 307, 369–376. http://dx.doi.org/10.1016/j.epsl.2011.05.011.

Thomsen, L., 1986. Weak elastic anisotropy. Geophysics 51 (10), 1954–1966. http://dx.doi.org/10.1190/1.1442051.

Tkalčić, H., 2010. Large variations in travel times of mantle-sensitive seismic waves from the South Sandwich Islands: Is the Earth's inner core a conglomerate of anisotropic domains? Geophys. Res. Lett. 37, L14312. http://dx.doi.org/10.1029/2010GL043841.

Tkalčić, H., 2015. Complex inner core of the Earth: the last frontier of global seismology. Rev. Geophys. 53, 59–94. http://dx.doi.org/10.1002/2014RG000469.

Tkalčić, H., Romanowicz, B., Houy, N., 2002. Constraints on D″ structure using PKP (AB-DF), PKP(BC-DF) and PcP-P traveltime data from broad-band records. Geophys. J. Int. 148, 599–616. http://dx.doi.org/10.1046/j.1365-246X.2002.01603x.

To, A., Romanowicz, B., Capdeville, Y., Takeuchi, N., 2005. 3D effects of sharp boundaries at the borders of the African and Pacific Superplumes: Observation and modeling. Earth Planet. Sci. Lett. 233, 137–153. http://dx.doi.org/10.1016/j.epsl.2005.01.037.

Trampert, J., Woodhouse, J.H., 2003. Global anisotropic phase velocity maps for fundamental mode surface waves between 40 and 150s. Geophys. J. Int. 154, 154–165. http://dx.doi.org/10.1046/j.1365-246X.2003.01952.x.

Trampert, J., van Heijst, H.J., 2002. Global azimuthal anisotropy in the transition zone. Science 296, 1297–1299. http://dx.doi.org/10.1126/science.1070264.

Tschauner, O., Ma, C., Beckett, J.R., Prescher, C., Prakapenka, V.B., Rossman, G.R., 2014. Discovery of bridgmanite, the most abundant mineral in Earth, in a shocked meteorite. Science 346, 1100–1102. 1100 [doi: 10.1126/science.1259369].

Tsuchiya, J., Tsuchiya, T., 2008. Postperovskite phase equilibria in the $MgSiO_3$-Al_2O_3 system. Proc. Nat. Acad. Sci. 105, 19160–19164. http://dx.doi.org/10.1073/pnas.0805660105.

Tsuchiya, J., Tsuchiya, T., 2011. First-principles prediction of a high-pressure hydrous phase of AlOOH. Physical Review B 83, 054115. http://dx.doi.org/10.1029/2010JB008018.

Tsuchiya, T., Wentzcovitch, R.M., da Silva, C.R.S., de Gironcoli, S., 2006. Spin transition in magnesiowstite in Earth's lower mantle. Phys. Rev. Lett. 96, 198501. doi.org/10.1103/PhysRevLett. 96.198501.

Tsujino, N., Nishihara, Y., Yamazaki, D., Seto, Y., Higo, Y., Takahashi, E., 2016. Mantle dynamics inferred from the crystallographic preferred orientation of bridgmanite. Nature 539, 81–85. http://dx.doi.org/10.1038/nature19777.

Tullis, J., Wenk, H.-R., 1994. Effect of muscovite on the strength and lattice preferred orientations of experimentally deformed quartz aggregates. Mat. Sci. Eng. A175, 209–220.

Ullemeyer, K., Siegesmund, S., Rasolofosaon, P.N.J., Behrmann, J.H., 2006. Experimental and texture-derived P-wave anisotropy of principal rocks from the TRANSALP traverse: an aid for the interpretation of seismic field data. Tectonophysics 414, 97–116. http://dx.doi.org/10.1016/j.tecto.2005.10.024.

Usui, Y., Hiramatsu, Y., Furumoto, M., Kanao, M., 2008. Evidence of seismic anisotropy and a lower temperature condition in the D″ layer beneath Pacific Antarctic Ridge in the Antarctic Ocean. Phys. Earth Planet. Inter. 167, 205–216.

Van den Berg, A.P., De Hoop, M.V., Yuen, D.A., Duchkov, A., van der Hilst, R.D., Jacobs, M.H.G., 2010. Geodynamical modeling and multiscale seismic expression of thermo-chemical heterogeneity and phase transitions in the lowermost mantle. Phys. Earth Planet. Inter. 180, 244–257. 10.1016/j.pepi.2010.02.008.

Vanacore, E., Niu, F., 2011. Characterization of the D″ layer beneath the Galapagos Islands using SKKS and SKS waveforms. Earthquake Sci. 24, 87–99. http://dx.doi.org/10.1007/s11589-011-0772-8.

Vasin, R., Wenk, H.-R., Kanitpanyacharoen, W., Matthies, S., Wirth, R., 2013. Anisotropy of Kimmeridge shale. J. Geophys. Res. 118, 1–26. http://dx.doi.org/10.1002/jgrb.50259.

Vilella, K., Shim, S.-H., Farnetani, C.G., Badro, J., 2015. Spin state transition and partitioning of iron: effects on mantle dynamics. Earth Planet. Sci. Lett. 417, 57–66. http://dx.doi.org/10.1016/j.epsl.2015.02.009.

Vine, F.J., Matthews, D.H., 1963. Magnetic anomalies over oceanic ridges. Nature 199, 947–949.

Vinnik, L., Farra, V., Romanowicz, B., 1989. Observational evidence for diffracted SV in the shadow of the Earth's core. Geophys. Res. Lett. 16 (6), 519–522. http://dx.doi.org/10.1029/GL016i006p00519.

Vinnik, L., Romanowicz, B., Bréger, L., 1994. Anisotropy in the center of the inner core. Geophys. Res. Lett. 21 (16), 1671–1674. http://dx.doi.org/10.1029/94GL01600.

Vinnik, L., Romanowicz, B., Le Stunff, Y., Makeyeva, L., 1995. Seismic anisotropy in the D″ layer. Geophys. Res. Lett. 22 (13), 1657–1660. http://dx.doi.org/10.1029/95GL01327.

Vinnik, L., Bréger, L., Romanowicz, B., 1998a. On the inversion of Sd particle motion for seismic anisotropy in D″. Geophys. Res. Lett. 25 (5), 679–682. http://dx.doi.org/10.1029/98GL00190.

Vinnik, L.P., Bréger, L., Romanowicz, B., 1998b. Anisotropic structures at the base of the Earth's mantle. Nature 393, 564–567. http://dx.doi.org/10.1038/31208.

Vočadlo, L., Alfè, D., Gillan, M.J., Wood, I.G., Brodholt, J.P., Price, G.D., 2003. Possi-ble thermal and chemical stabilization of body centered-cubic iron in the Earth's core. Nature 424, 536–539. http://dx.doi.org/10.1038/nature01829.

Vočadlo, L., Wood, I.G., Gillan, M.J., Brodholt, J., Dobson, D.P., Price, G.D., Alfe, D., 2008. The stability of bcc-Fe at high pressures and temperatures with respect to tetragonal strain. Phys. Earth Planet. Inter. 170, 52–59. http://dx.doi.org/10.1016/j. pepi.2008.07.032.

Vočadlo, L., Dobson, D.P., Wood, I.G., 2009. Ab initio calculations of the elasticity of hcp-Fe as a function of temperature at inner- core pressure. Earth Planet. Sci. Lett. 288, 534–538. http://dx.doi.org/10.1016/j.epsl.2009.10.015.

Voigt, W., 1887. Theoretische Studien über die Elasticitätsverhältnisse der Krystalle. Abh. Kgl. Ges. Wiss. Göttingen Math. Kl. 34, 3–51.

Walker, A.M., Forte, A.M., Wookey, J., Nowacki, A., Kendall, J.-M., 2011. Elastic anisotropy of D'' predicted from global models of mantle flow. Geochem. Geophys. Geosystems 12, Q10006. http://dx.doi.org/10.1029/2011GC003732.

Wang, Y., Weidner, D.J., Guyot, F., 1996. Thermal equation of state of $CaSiO_3$ perovskite. J. Geophys. Res. 101, 661–672. http://dx.doi.org/10.1029/95JB03254.

Wang, Y., Wen, L., 2007. Complex seismic anisotropy at the border of a very low velocity province at the base of the Earth's mantle. J. Geophys. Res. 112, B09305. http://dx.doi.org/10.1029/2006JB004719.

Wang, Y., Durham, W.B., Getting, I.C., Weidner, D.J., 2003. The deformation-DIA: A new apparatus for high temperature triaxial deformation to pressures up to 15 GPa. Rev. Sci. Instrum. 74, 3002. http://dx.doi.org/10.1063/1.1570948.

Wang, Y., Lesher, C., Fiquet, G., Rivers, M.L., Nishiyama, N., Siebert, J., Roberts, J., Morard, G., Gaudio, S., Clark, A., Watson, H., Menguy, N., Guyot, F., 2011. In situ high-pressure and high-temperature X-ray microtomographic imaging during large deformation: A new technique for studying mechanical behavior of multiphase composites. Geosphere 7 (1), 40–53. http://dx.doi.org/10.1130/GES00560.1.

Wang, T., Song, X., Xia, H.H., 2015. Equatorial anisotropy in the inner part of the Earth's inner core from autocorrelation of earthquake coda. Nature Geosci. 8, 224–227. http://dx.doi.org/10.1038/ngeo2354.

Waszek, L., Irving, J., Deuss, A., 2011. Reconciling the hemispherical structure of Earth's inner core with its super-rotation. Nat. Geosci. 4, 264–267. http://dx.doi.org/10.1038/ngeo1083.

Wegener, A., 1915. Die Entstehung der Kontinente und Ozeane. Vieweg, Braunschweig.

Weidner, D.J., Li, L., 2015. Methods for the study of high P-T deformation and rheology. . 2nd ed. Treatise on Geophysics 2nd ed., pp. 351–368.

Weis, D., Garcia, M.O., Rhodes, J.M., Jellinek, M., Scoates, J.S., 2011. Role of the deep mantle in generating bilateral the compositional asymmetry of the Hawaiian mantle plume. Nature Geosci. 4, 831–838. http://dx.doi.org/10.1038/ngeo1328.

Wenk, H.-R., Canova, G., Brechet, Y., Flandin, L., 1997. A deformation-based model for recrystallization of anisotropic materials. Acta Mater. 45, 3283–3296.

Wenk, H.-R., Tomé, C., 1999. Simulation of deformation and recrystallization of olivine deformed in simple shear. J. Geophys. Res. 104, 25513–25527. http://dx.doi.org/10.1029/1999JB900261.

Wenk, H.-R., Matthies, S., Hemley, R.J., Mao, H.-K., Shu, J., 2000a. The plastic deformation of iron at pressures of the Earth's inner core. Nature 405, 1044–1047. http://dx.doi.org/10.1016/j.epsl.2004.07.033.

Wenk, H.-R., Baumgardner, J., Lebensohn, R., Tomé, C., 2000b. A convection model to explain anisotropy of the inner core. J. Geophys. Res. 105, 5663–5677. http://dx.doi.org/10.1029/1999JB900346.

Wenk, H.-R., Lonardelli, I., Pehl, J., Devine, J., Prakapenka, V., Shen, G., Mao, H.-K., 2004. In situ observation of texture development in olivine, ringwoodite, magnesiowuestite and silicate perovskite at high pressure. Earth Planet. Sci. Lett. 226, 507–519. http://dx.doi.org/10.1016/j. epsl.2004.07.033.

Wenk, H.-R., Speziale, S., McNamara, A.K., Garnero, E.J., 2006. Modeling lower mantle anisotropy development in a subducting slab. Earth Planet. Sci. Lett. 245, 302–314. http://dx.doi.org/10.1016/j.epsl.2006.02.028.

Wenk, H.-R., Armann, M., Burlini, L., Kunze, K., Bortolotti, M., 2009. Large strain shearing of halite: experimental and theoretical evidence for dynamic texture changes. Earth Planet. Sci. Lett. 280, 205–210. http://dx.doi.org/10.1016/j.epsl.2009.01.036.

Wenk, H.-R., Cottaar, S., Tomé, C., McNamara, A., Romanowicz, B., 2011. Deformation in the lowermost mantle: From polycrystal plasticity to seismic anisotropy. Earth Planet. Sci. Lett. 306, 33–45. http://dx.doi.org/10.1016/j.epsl.2011.03.021.

Wenk, H.-R., Lutterotti, L., Kaercher, P., Kanitpanyacharoen, W., Miyagi, L., Vasin, R., 2014. Rietveld texture analysis from synchrotron diffraction images: II. Complex multiphase materials and diamond anvil cell experiments. Powder Diffraction 29, 220–232. http://dx.doi.org/10.1017/S0885715614000360.

Wentzcovitch, R., Karki, B., Cococcioni, M., de Gironcoli, S., 2004. Thermoelastic properties of MgSiO3-perovskite: insights on the nature of the Earth's lower mantle. Phys. Rev. Lett. 92 (1), 1–4.

Wentzcovitch, R.M., Tsuchiya, T., Tsuchiya, J., 2005. $MgSiO_3$ postperovskite at D'' conditions. Proc. Nat. Acad. Sci. 103, 543–546. http://dx.doi.org/10.1073/pnas.0506879103.

White, W.M., 2015. Probing the Earth's deep interior through geochemistry. Geochem. Perspect. 4 (2), 95–251.

Williams, Q., Garnero, E.J., 1996. Seismic evidence for partial melt at the base of Earth's mantle. Science 273, 1528–1530. http://dx.doi.org/10.1126/science.273.5281.1528.

Woodhouse, J.H., Giardini, D., Li, X.-D., 1986. Evidence for inner core anisotropy from free oscillations. Geophys. Res. Lett. 13, 1549–1552. http://dx.doi.org/10.1029/GL013i013p01549.

Wookey, J., Kendall, J.-M., 2007. Seismic anisotropy of post-perovskite and the lowermost mantle. In: Post-Perovskite: The Last Mantle Phase Transition. In: Hirose, K., Brodholt, J., Lay, T., Yuen, D. (Eds.), . Geophysical Monograph Series, vol. 174. AGU, 984, Washington, DC, pp. 171–189.

Wookey, J., Kendall, J., 2008. Constraints on lowermost mantle mineralogy and fabric beneath Siberia from seismic anisotropy. Earth Planet. Sci. Lett. 275, 32–42. http://dx.doi.org/10.1016/j.epsl.2008.07.049.

Wookey, J., Kendall, J., Rümpker, G., 2005a. Lowermost mantle anisotropy beneath the north Pacific from differential S-ScS splitting. Geophys. J. Int. 161, 829–838. http://dx.doi.org/10.1111/j.1365-246X.2005.02623.x.

Wookey, J., Stackhouse, S., Kendall, J.-M., Brodholt, J., Price, G.D., 2005b. Efficacy of the post-perovskite phase as an explanation for lowermost-mantle seismic properties. Nature 438, 1004–1007. http://dx.doi.org/10.1038/nature-04345.

Wu, X., Lin, J.-F., Kaercher, P., Mao, Z., Wenk, H.-R., Prakapenka, V., 2017. Seismic anisotropy of the D'' layer induced by (001) deformation of post-perovskite. Nature Commu. 8. http://dx.doi.org/10.10038/ncomms14669. 14669.

Wysession, M., Lay, T., Revenaugh, J., Williams, Q., Garnero, E.J., Jeanloz, R., Kellogg, L.H., 1998. The D'' discontinuity and its implications. In: Gurnis, M., Wysession, M.E., Knittle, E., Buffett, B.A. (Eds.), The core-mantle boundary region. American Geophysical Union, Washington, DC, pp. 273–298. http://dx.doi.org/10.1029/GD028p0273.

Yamasaki, D., Karato, S.I., 2001. Some mineral physics constraints on the rheology and geothermal structure of Earth's lower mantle -. Amer. Mineral. 86, 385–391. http://dx.doi.org/10.2138/am-2001-0401.

Yamazaki, D., Ito, E., Yoshino, T., Tsujino, N., Yoneda, A., Guo, X., Xu, F., Higo, Y., Funakoshi, K., 2014. Over 1 Mbar generation in the Kawai-type multianvil apparatus and its application to compression of $(Mg_{0.92}Fe_{0.08})SiO_3$ perovkite and stishovite. Phys. Earth Planet. Int. 228, 262–267. http://dx.doi.org/10.1016/j.pepi.2014.01.013.

Yoshida, S., Sumita, I., Kumazawa, M., 1996. Growth model of the inner core coupled with outer core dynamics and the resulting elastic anisotropy. J. Geophys. Res. 101, 28085–28103.

Yuan, K., Beghein, C., 2013. Seismic anisotropy changes across upper mantle phase transitions, Earth Planet. Sci. Lett. 374, 132–144. http://dx.doi.org/10.1016/j.epsl.2013.05.031.

Zhang, Z., Stixrude, L., Brodholt, J., 2013. Elastic properties of $MgSiO_3$-perovskite under lower mantle conditions and the composition of the deep Earth. Earth Planet. Sci. Lett. 379, 1–12. http://dx.doi.org/10.1016/j.epsl.2013.07.034.

Zhang, L., Popov, D., Meng, Y., Wang, J., Ji, C., Li, B., Mao, H.-K., 2016. In-situ crystal structure determination of seifertite SiO_2 at 129 GPa: Studying a minor phase near Earth's core-mantle boundary. Amer. Mineral. 101, 231–234. doi.org/10.2138/am-2016-5525.